

THESIS ON NATURAL AND EXACT SCIENCES B239

**Study of $\text{Cu}_2(\text{Zn,Cd})\text{SnS}_4$ Absorber
Materials for Monograin Layer
Solar Cells**

MARIS PILVET



TALLINN UNIVERSITY OF TECHNOLOGY
School of Engineering
Department of Materials and Environmental Technology

This dissertation was accepted for the defence of the degree of Doctor of Philosophy in Natural and Exact Sciences on August 03, 2017.

Supervisor: Senior Research Scientist Marit Kauk-Kuusik, Department of Materials and Environmental Technology, Tallinn University of Technology, Estonia

Opponents: Prof. Charlotte Platzer Björkman, Department of Engineering Science, Solid State Electronics, Uppsala University, Sweden

Dr. Vambola Kisand, Faculty of Science and Technology,
Institute of Physics, University of Tartu, Estonia

Defense of the thesis: September 07, 2017 at 14.00
Lecture hall: U06A-229
Tallinn University of Technology, Ehitajate tee 5,
Tallinn

Declaration:

Hereby I declare that this doctoral thesis, my original investigation and achievement, submitted for the doctoral degree at Tallinn University of Technology, has not been submitted for any academic degree.

/Maris Pilvet/



Copyright: Maris Pilvet, 2017

ISSN 1406-4723

ISBN 978-9949-83-141-8 (publication)

ISBN 978-9949-83-142-5 (PDF)

LOODUS- JA TÄPPISTEADUSED B239

**Päikesepatareides kasutatavate
 $\text{Cu}_2(\text{Zn,Cd})\text{SnS}_4$ absorbermaterjalide
uurimine**

MARIS PILVET

TABLE OF CONTENTS

LIST OF PUBLICATIONS	7
AUTHOR'S CONTRIBUTION	8
LIST OF ABBREVIATIONS.....	9
INTRODUCTION	10
1 LITERATURE OVERVIEW AND THE AIM OF THE STUDY	12
1.1 I ₂ -II-IV-VI ₄ compounds based solar cells	12
1.2 Structural properties of Cu ₂ ZnSnS ₄ and Cu ₂ CdSnS ₄	13
1.3 Defect structure of Cu ₂ ZnSnS ₄ and Cu ₂ CdSnS ₄	14
1.4 Ordering-disordering in crystal structure	15
1.5 Bandgap engineering	17
1.6 Monograin powder technology	18
1.7 Secondary phases in Cu ₂ ZnSnS ₄ and Cu ₂ CdSnS ₄	19
1.8 Summary of the literature review and objectives of the research	20
2 EXPERIMENTAL.....	22
2.1 Preparation of powder samples	22
2.2 Post-treatments of Cu ₂ ZnSnS ₄ monograin powders.....	23
2.2.1 Cooling parameters for Cu ₂ ZnSnS ₄ monograin powders.....	24
2.2.2 Low-temperature annealing of Cu ₂ ZnSnS ₄ monograin powder.....	26
2.2.3 Low-temperature annealing of Cu ₂ CdSnS ₄ polycrystalline powder	26
2.3 Fabrication of monograin layer solar cells.....	27
2.4 Characterization of monograin and polycrystalline powders.....	28
2.4.1 Material characterization	28
2.4.2 Solar cell characteristics	29
3 RESULTS AND DISCUSSION.....	30
3.1 Zn substitution by Cd in Cu ₂ ZnSnS ₄ monograin powders	30
3.1.1 Composition of Cu ₂ (Zn _{1-x} Cd _x)SnS ₄ monograin powders.....	30
3.1.2 Influence of the Cd content on Cu ₂ ZnSnS ₄ structural properties.....	31
3.1.2.1 X-ray diffraction analysis.....	31
3.1.2.2 Raman analysis	33
3.1.3 Influence of the Cd content on Cu ₂ ZnSnS ₄ optical properties	34
3.2 Disordering studies in Cu ₂ ZnSnS ₄ monograin powders	36
3.2.1 Influence of cooling rate on Cu ₂ ZnSnS ₄ properties	36

3.2.1.1	Compositional analysis	36
3.2.1.2	Photoluminescence and Raman results	37
3.2.2	Impact of low-temperature annealing on the CZTS monograin layer solar cells	40
3.3	Modification of the optoelectronic properties of $\text{Cu}_2\text{CdSnS}_4$ through low-temperature annealing.....	43
3.3.1	Results of structural and compositional analysis	43
3.3.2	Photoluminescence analysis results	46
CONCLUSIONS	52
ACKNOWLEDGEMENTS	54
ABSTRACT	55
KOKKUVÕTE	57
REFERENCES	59
APPENDIX A	67
APPENDIX B	95

LIST OF PUBLICATIONS

The thesis is based on the following publications, which are referred to in the text by Roman numerals I-IV:

- I. **M. Pilvet**, M. Kauk-Kuusik, M. Altosaar, M. Grossberg, M. Danilson, K. Timmo, A. Mere, V. Mikli, Compositionally tunable structure and optical properties of $\text{Cu}_{1.85}(\text{Cd}_x\text{Zn}_{1-x})_{1.1}\text{SnS}_{4.1}$ ($0 \leq x \leq 1$) monograin powders, *Thin Solid Films* 582 (2015) 180–183.
 - II. K. Timmo, M. Kauk-Kuusik, **M. Pilvet**, T. Raadik, M. Altosaar, M. Danilson, M. Grossberg, J. Raudoja, K. Ernits, Influence of order-disorder in $\text{Cu}_2\text{ZnSnS}_4$ powders on the performance of monograin layer solar cells, *Thin Solid Films* 633 (2017) 122–126.
 - III. **M. Pilvet**, M. Kauk-Kuusik, M. Grossberg, T. Raadik, V. Mikli, R. Traksmäa, J. Raudoja, K. Timmo, J. Krustok, Modification of the optoelectronic properties of $\text{Cu}_2\text{CdSnS}_4$ through low-temperature annealing treatments, *Journal of Alloys and Compounds* 723 (2017) 820-825.
-
- IV. K. Timmo, M. Kauk-Kuusik, M. Altosaar, J. Raudoja, T. Raadik, M. Grossberg, T. Varema, **M. Pilvet**, I. Leinemann, O. Volobujeva, E. Mellikov, Novel $\text{Cu}_2\text{CdSnS}_4$ and $\text{Cu}_2\text{ZnGeSe}_4$ absorber materials for monograin layer solar cell application, Proceeding of *EU PVSEC 2013 (2013)*, Wiley-Blackwell 2385–2388.

Copies of these articles are included in APPENDIX A.

AUTHOR'S CONTRIBUTION

The contribution by the author to the papers included in the thesis is as follows:

- I. Major part of experimental work (preparation of precursors and monograin powders, solar cell preparation), part of characterization, analysis of the results, and major part of writing.
 - II. Major part of experimental work (etching and thermal treatments of the monograins, CBD-CdS deposition, solar cell preparation), part of characterization, analysis of the results, and minor part of writing.
 - III. Major part of experimental work (preparation of some precursors and $\text{Cu}_2\text{CdSnS}_4$ polycrystalline powders, thermal treatments of the powder), part of characterization, analysis of the results, and major part of writing.
-
- IV. Part of experimental work (preparation of some precursors and $\text{Cu}_2\text{CdSnS}_4$ monograin powders, solar cell preparation), part of characterization, and minor part of writing.

LIST OF ABBREVIATIONS

Br ₂ -MeOH	bromine in methanol
CCdTS	Cu ₂ CdSnS ₄ , copper cadmium tin sulfide
CIGSe	Cu(In,Ga)Se ₂ , copper (indium, gallium) diselenide
CZCdTS	Cu ₂ Zn _{1-x} Cd _x SnS ₄ , copper zinc cadmium tin sulfide
CZTS	Cu ₂ ZnSnS ₄ , copper zinc tin sulfide
CZTSSe	Cu ₂ ZnSn(S,Se) ₄ , copper zinc tin sulfoselenide
CBD	chemical bath deposition
I-V	current-voltage
EDX	energy dispersive x-ray spectroscopy
EQE	external quantum efficiency
E_g	band gap energy
E_g^*	effective band gap energy
FF	fill factor
HT	high-temperature
J_{sc}	short circuit current
LTA	low-temperature annealing
MGL	monograin layer
PV	photovoltaic
PL	photoluminescence
QE	quantum efficiency
RT	room temperature
SEM	scanning electron microscope
T_{ann}	temperature annealing
T_c	critical temperature
V_{oc}	open circuit voltage
η	efficiency
XRD	X-ray diffraction
PCE	power conversion efficiency

INTRODUCTION

Global electricity generation was around 21 000 TWh in 2015 [1]. Most of the electricity is produced using conventional carbon-based technologies due to their lower price per watt. However, global fossil resources are depleting while at the same time, the world's population is growing rapidly. Therefore, the need for a sustainable and environmentally friendly alternative energy source is unavoidable.

Sunlight is the most abundant and free natural energy source, and light-to-electricity conversion in a solar cell is one of the best-developed renewable energy technologies [2]. The production of solar cells with reduced cost, high efficiency and environmentally friendly processes is the current challenge for photovoltaic research and industry for photovoltaics (PV) to be competitive with conventional energy technologies. Currently, approximately 90% of the world's PV market is dominated by silicon-based technologies. The record laboratory cell efficiency is 25.6% for mono-crystalline and 20.8% for multi-crystalline silicon wafer-based technology [3]. Japan's Kaneka Corporation has reached a certified conversion efficiency of more than 26% for silicon heterojunction solar cells [4].

In 2015, the market share of all thin film technologies amounted to about 8% of the total annual production [3]. The most efficient thin film solar cells with efficiencies of 22.1% [5] and 22.6% [6] are based on cadmium telluride (CdTe) and copper (indium, gallium) diselenide (CIGSe), respectively. As production volumes increase, the cost and scarcity of In and Te will become major issues that may limit the utilization of widespread CdTe and CIGSe photovoltaics. In the last decade, new absorber materials that use low cost and broadly available elements have been proposed as an alternative. Quaternary $I_2-II-IV-VI_4$ (I = Cu, Ag; II = Zn, Cd; IV = Si, Ge, Sn; VI = S, Se) chalcogenides form a large group of semiconductors with variable structural, optical and electrical properties. The kesterite-type Cu_2ZnSnS_4 (CZTS), $Cu_2ZnSnSe_4$ (CZTSe) and their solid solutions $Cu_2ZnSn(S,Se)_4$ (CZTSSe) continue to excite interest as potential earth-abundant alternatives to CIGSe for application as absorber materials in solar cells. These materials are closely related to CIGSe as their crystal structures are very similar and the same preparation methods can be used.

By 2014, the efficiency of CZTSSe solar cells had reached 12.7% [7], but progress since then has been slowing down. The main limiting factor for device performance is the open circuit voltage, which is ~200 mV lower than that of CIGSe cells with comparable bandgaps. The reasons for the voltage losses in kesterite solar cells are still not clear. One possible cause is enhanced recombination due to tail states arising from Cu-Zn disorder, surface recombination and the influence of secondary phases [8-10].

During the last decade, the power conversion efficiency of solar cells based on pure Cu_2ZnSnS_4 absorber has achieved as high as 9.5% by using $Zn_{1-x}Cd_xS$ buffer layer [11]. Despite suitable properties of the absorber material, the performance of the photovoltaic device is still poor. For high efficiency solar

cells, the bandgap of the absorber layer is one of the important parameters. According to the Shockley–Queisser efficiency limit for solar cells using a single p - n junction, an ideal solar energy absorber material should have a bandgap around 1.4 eV [12]. The direct bandgap of CZTS is 1.5 eV [13]. To reach the ideal bandgap, bandgap engineering is possible. Several studies have shown the possibility to tune the bandgap of CZTS between 1.0 to 1.5 eV due to the change in the anion composition. First-principles calculations on the band structure and optical properties of CZTSSe have indicated that the mixed-anion solutions are highly miscible [14]. It is also difficult to control the anion ratio of S/Se (and therefore the control of bandgap) precisely through the annealing processes.

For most compound semiconductors, it is commonly accepted that substitution of heavier atoms from the same group in the periodic table results in narrower bandgaps. Therefore, another possibility for tuning the bandgap of CZTS is through substitution of Zn atom by Cd atom into the crystal lattice forming a new $\text{Cu}_2\text{CdSnS}_4$ compound. Cd is a suitable element for lowering the bandgap of CZTS because it belongs to the same group of elements and is larger than Zn.

The present thesis is divided into four Chapters. The Introduction is followed by a brief literature review in Chapter 1. It provides a short overview of $\text{I}_2\text{-II-V-VI}_4$ compounds based solar cells. Further, the properties of $\text{Cu}_2\text{ZnSnS}_4$ and $\text{Cu}_2\text{CdSnS}_4$, which are important for absorber materials for PV, are outlined, followed by the description of the monograin powder technology. Summary of the literature review and objectives of the research close Chapter 1. Chapter 2 presents the experimental details of monograin powder and polycrystalline powder synthesis processes, as well as post-growth treatments and monograin layer solar cell fabrication. The techniques used to characterize the properties of powders and solar cells are also introduced. Chapter 3 is divided into three sections and contains original experimental results together with the discussion. All the results have been published in four peer-reviewed papers included in Appendix A. The first section reports the effect of Zn substitution by Cd to the structural and optical properties of $\text{Cu}_2\text{ZnSnS}_4$. The second section comprises systematic investigation of the influence of structural disordering in CZTS on the optoelectronic properties and devices based on these powders. The third section is devoted to the modification of optoelectronic properties of polycrystalline $\text{Cu}_2\text{CdSnS}_4$ powder by the low-temperature annealing process. The thesis concludes with a summary of the main goals.

1 LITERATURE OVERVIEW AND THE AIM OF THE STUDY

1.1 I₂-II-IV-VI₄ compounds based solar cells

Cu₂ZnSnS₄ (CZTS) and Cu₂CdSnS₄ (CCdTS) belong to the group of I₂-II-IV-VI₄ compounds and have recently emerged as promising light-absorber materials for solar cells due to suitable energy bandgaps, high absorption coefficient and earth abundant elements. The direct bandgap of CZTS is around 1.5 eV [13, 15, 16]. At first, the direct bandgap of CCdTS was estimated as 1.06 eV [17], but for today, it is proposed to be around 1.4 eV [18-20]. Absorption coefficients larger than 10⁴ cm⁻¹ and *p*-type conductivity were also measured for both of these compounds [17].

The pioneers of CZTS solar cells are Kentaro Ito and Hironori Katagiri. The former was the first to report synthesis of CZTS thin films and suggest their potential photovoltaic application [7]. The latter was the first to fabricate the first CZTS solar cell, with an efficiency of 0.66% [21]. Until 2008, research on CZTS solar cells was limited to a few groups. In 2010, IBM group achieved a high conversion efficiency of about 10% [22]. In 2013, the Japanese thin-film solar company Solar Frontier announced that in joint research with IBM and Tokyo Ohka Kogyo, they had developed a world-record setting CZTSSe solar cell with an energy conversion efficiency of 12.6% [23]. Currently, the highest record efficiency for pure sulfide CZTS thin film is 9.5% [11].

With regard to Cu₂CdSnS₄, only few literature reports are available about solar cell efficiencies based on CCdTS absorber material. In the 1970s, the Bell laboratories were the first to make solar cells on Cu₂CdSnS₄ single crystal absorbers. The Au/Cu₂CdSnS₄/CdS/In-Ga solar cell exhibited an efficiency of 1.6% [26]. In 2015, W. Zhao *et al.* [27] presented the Cu₂CdSn(S,Se)₄ nanocrystal thin film solar cell with a power conversion efficiency of 3.1% and groups from NTU reported the best efficiency of 9.24% by adjusting the ratio of Zn/Cd in Cu₂Zn_{1-x}Cd_xSnS₄ thin films using the low cost sol-gel method [28]. Recently, a group from UNSW in Australia led by M. A. Green investigated the effects of Cd-alloying and the mechanism underpinning the performance improvement and achieved the Cd-alloyed CZTS solar cell efficiency beyond 11% [29].

Although a noteworthy increase in the conversion efficiencies of I₂-II-IV-VI₄ compounds based solar cells have been achieved in recent years, significant improvements are required to further enhance efficiency to the level of CIGSe solar cells, and to increase the commercial viability of these types of photovoltaics.

The following sections analyze some of the main aspects influencing the efficiency of $\text{Cu}_2\text{ZnSnS}_4$ and $\text{Cu}_2\text{CdSnS}_4$ based devices, from the fundamental properties of absorber materials to the aspects related to efficiency improvements.

1.2 Structural properties of $\text{Cu}_2\text{ZnSnS}_4$ and $\text{Cu}_2\text{CdSnS}_4$

$\text{Cu}_2\text{ZnSnS}_4$ and $\text{Cu}_2\text{CdSnS}_4$ can be derived from the ternary CuInS_2 chalcopyrite type lattice by replacing half of the indium atoms with zinc or cadmium atoms and the other half with tin atoms. The crystal structures are therefore very closely related, which presumes that excellent optoelectronic properties can also be achieved for these materials.

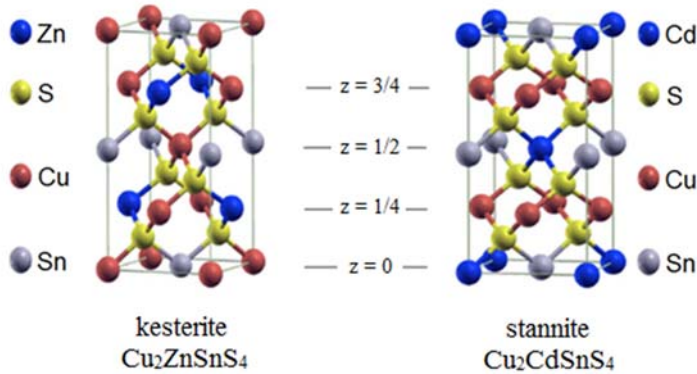


Figure 1.1 Crystal structures of kesterite-type $\text{Cu}_2\text{ZnSnS}_4$ and stannite-type $\text{Cu}_2\text{CdSnS}_4$ [30].

Regarding the arrangement of the atoms in the crystal structure, two types of structures with very similar formation energy exist: kesterite (space group $\bar{I}4$) and stannite (space group $\bar{I}42m$) (see Figure 1) [15, 30, 31]. Initially, CZTS was described as stannite-type [17], but now kesterite structure has been found to be favored both experimentally [30] and theoretically [32]. Due to the similar structural properties and isoelectronic nature of Cu^+ and Zn^{2+} , it is very difficult to distinguish between the kesterite and stannite phases experimentally by X-ray diffraction. It was confirmed [33] by neutron diffraction and in [34] by anomalous diffraction studies that CZTS compounds crystallize in the kesterite structure. It is suggested that the observed stannite structure for CZTS compounds was due to the existence of partial disorders of Cu and Zn sites in the I–II (001) layer of the kesterite phase [33–36]. This disorder could be due to the formation of both kesterite and stannite phases during the crystallization process since there is only a negligible difference in the lattice parameters and the total energy. CCdTS has been found to crystallize in the stannite-type crystal structure [36–38].

In both structures, the kesterite-type and the stannite-type, cations are located on tetrahedral sites but their distributions on planes perpendicular to the c-axis are not the same. Specifically, the kesterite structure consists of two

alternating cation layers, each containing Cu and Zn or Cu and Sn, whereas in the stannite structure, a layer of Cu alternates with a layer of Cd and Sn [33, 36].

1.3 Defect structure of $\text{Cu}_2\text{ZnSnS}_4$ and $\text{Cu}_2\text{CdSnS}_4$

Defects play an important role in the resulting optoelectronic properties of semiconductor materials. Lattice defects are important material properties and are crucial to the application of semiconductors in photovoltaic devices, since they directly influence the generation, separation and recombination of electron-hole pairs [39].

Based on several experimental and theoretical studies [40-42], the main features of the defect properties of CZTS and CCdTS are very similar. It has been found that Cu_{Zn} antisite defects have low formation energy and high concentration due to the small atom size and chemical potential difference between Cu and Zn (Cu, Zn ≈ 1.35 Å) [43], making the synthesized CZTS always *p*-type. As the atom size difference between Cu and Cd is large (Cd ≈ 1.55 Å) [43], it can be expected that the formation energy of the Cu_{Cd} antisite may be high and the dominant defect will be the shallow Cu vacancy (V_{Cu}). The first principles calculations have shown that Cu_{Cd} antisite defect still has low formation energy, slightly higher than Cu_{Zn} in CZTS, by about 0.2 eV [42]. Thus, the dominance of the acceptor Cu_{Cd} results in intrinsic *p*-type conductivity of $\text{Cu}_2\text{CdSnS}_4$, similar to that in CZTS [42].

A critical issue to improve the material quality of an absorber layer is the control of intrinsic defects. In fact, the low open circuit voltage (V_{oc}) has been attributed to the recombination of light induced charge carriers due to the activity of detrimental defects, which can be located in the bulk [44, 45] as well as at the grain boundaries [46]. The type of defects prevailing and their [46] concentration depends on the synthesis conditions.

So far, to obtain efficient solar cell devices from CZTS films, Cu-poor and Zn-rich composition has been found to be most suitable [47-49] and this non-stoichiometry in the quaternary kesterites results in the facile formation of self-compensated defect complexes such as $[\text{Cu}_{\text{Zn}} + \text{Zn}_{\text{Cu}}]$, $[\text{V}_{\text{Cu}} + \text{Zn}_{\text{Cu}}]$, $[\text{Zn}_{\text{Sn}} + 2\text{Zn}_{\text{Cu}}]$, $[2\text{Cu}_{\text{Zn}} + \text{Sn}_{\text{Zn}}]$ in CZTS. Similar defect complexes like $[\text{Cu}_{\text{Cd}} + \text{Cd}_{\text{Cu}}]$ and $[2\text{Cu}_{\text{Cd}} + \text{Sn}_{\text{Cd}}]$ have been proposed for Cu-poor and Cd-rich CCdTS [44]. The defect pair $[\text{Cu}_{\text{Zn}} + \text{Zn}_{\text{Cu}}]$ turns out to be the most likely defect in CZTS with the lowest formation energy of 0.2 eV, resulting in a high concentration of these defects. Similarly, self-compensated antisite pair $[\text{Cu}_{\text{Cd}} + \text{Cd}_{\text{Cu}}]$ having the formation energy of 0.21 eV is dominating in CCdTS. The formation and clustering of $[\text{Cu}_{\text{Zn}} + \text{Zn}_{\text{Cu}}]$ and $[\text{Cu}_{\text{Cd}} + \text{Cd}_{\text{Cu}}]$ antisite pairs induce a small bandgap shrinking in the corresponding sample areas, which can cause bandgap fluctuations in the material [42].

Besides $[\text{Cu}_{\text{Zn}} + \text{Zn}_{\text{Cu}}]$ and $[\text{Cu}_{\text{Cd}} + \text{Cd}_{\text{Cu}}]$ pairs, the formation energies of $[2\text{Cu}_{\text{Zn}} + \text{Sn}_{\text{Zn}}]$ and $[2\text{Cu}_{\text{Cd}} + \text{Sn}_{\text{Cd}}]$ clusters are also low, about 0.2-0.6 eV and 0.43-0.65 eV, respectively [39, 42]. These clusters induce significant downshift

of the conduction band as well as the upshift of the valence band. High population of such defect complexes causes significant bandgap fluctuations and electron-trapping states in the absorber materials and is thus detrimental to the solar cell performance.

Zn and Cu are close neighbors in the periodic table with almost similar atomic size. Therefore, it is more likely for Zn and Cu to occupy vacancies of counterparts and result in a disordered kesterite structure in CZTS [50]. This is usually considered as the main reason for the Cu_{Zn} and Zn_{Cu} antisite defects in the CZTS system [51]. Thus, using a larger Cd atom to partially replace Zn may be one possible method to decrease the concentration of antisite defects [23]. The other possibility to reduce the Cu-Zn disordering appears to be a low temperature post-annealing treatment [52, 53].

In the next sections, the disordering phenomenon proven to exist in the kesterite structure in several studies [32, 52, 54] will be explained. In addition, a route to optimize the bandgap of CZTS by cation substitution will be introduced.

1.4 Ordering-disordering in crystal structure

Cu-Zn disorder in kesterites arises because of facile atomic exchange within $z = 1/4$ and $z = 3/4$ planes of the unit cell, while the rest of the lattice is undisturbed [33, 55, 56]. Figure 1.2 shows the relevant lattice sites and planes in the kesterite structure and illustrates the disorder-free and fully disordered cases. The impact of Cu-Zn disorder on the properties of CZTS is an intensely discussed topic and there are still unresolved problems such as influence on the device performance.

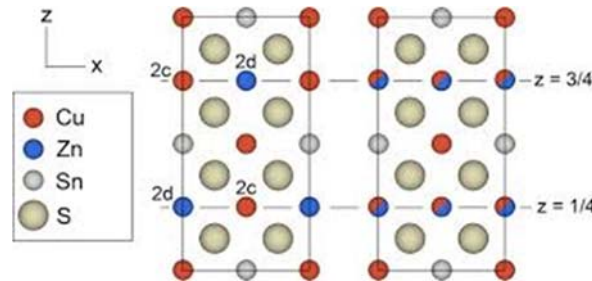


Figure 1.2 Projections of the conventional kesterite unit cell of CZTS along the y-axis, indicating the atoms, lattice planes and lattice sites involved in the Cu-Zn disorder. The left-hand image shows the perfectly ordered case. The right-hand image shows the fully disordered case, in which the Cu and Zn atoms in the $z = 1/4$ and $3/4$ planes have a random distribution among the 2c and 2d sites [57].

Several recent studies [54, 58] have shown that the existence of Cu and Zn cation disorder in $\text{Cu}_2\text{ZnSnS}_4$ kesterite crystal structure could be one reason for the large open circuit voltage deficit limiting the efficiency of the solar cell

device. Therefore, it is required to gain control over the Cu–Zn disorder. This requires knowledge of the kinetics and temperature dependence of the order-disorder transition. To describe the ordering of crystals, the ordering parameter S is used, as introduced in Vineyard's theory of order–disorder kinetics [59]. S is determined by the proportion of atoms located on the correct lattice sites in the relevant crystal substructure. The order parameter $S = 1$ is for perfect ordering and $S = 0$ for total disorder. S decreases with increasing annealing temperature, and drops rapidly to zero at a critical temperature (T_c). The order–disorder transition occurs at that critical temperature [52].

The degree of Cu-Zn disorder has been found to depend on the cooling rate after sample synthesis. Rapid cooling results in the highest degree of disorder, while slow cooling tends to give more ordered CZTS [33, 55, 56].

It is also possible to change the degree of Cu–Zn disordering during low-temperature (LT) post-annealing at the temperature below the critical temperature [52, 60, 61].

The order-disorder transition was found to be reversible and occurs at 260 ± 10 °C [52], 200 ± 20 °C [53] and 195 ± 5 °C [54] for reactively sputtered CZTS, co-evaporated CZTSe and solution-processed CZTSSe films, respectively.

Near-resonant Raman scattering [52, 53] and photo-luminescence spectroscopy [61, 62] are useful tools to estimate the degree of Cu-Zn disordering in kesterites. The low-temperature annealing at different temperatures below and above the critical temperature leads to the changes in the degree of Cu-Zn ordering. It appeared in the width and symmetry of the A_1 Raman peak [52]. The A_1 Raman peak was broadened with the increasing annealing temperature, which is attributed to the higher degree of disordering. It was found that the asymmetry of the A_1 peak is caused by a shoulder peak at low wavenumber side that was attributed to the A_1 mode of the disordered $\text{Cu}_2\text{ZnSnS}_4$ [52, 53, 63]. Scragg *et al.* measured the 785-nm Raman spectra of nominally ordered and disordered CZTS films and calculated the ratio of $Q = (m_{2A}) / I(m_{3A})$, where $I(m_{2A})$ and $I(m_{3A})$ are the Raman peak intensities for the A modes at 288 and 304 cm^{-1} . Thus, they showed that there exists the correlation: the larger the Q value, the more ordered is the structure [52].

By the first-principles calculations, the bandgap energy difference between the ordered and disordered kesterite phases was predicted to be around 0.1 eV in CZTS [64]. It is also confirmed by low-temperature photoluminescence (PL) studies that the bandgap energy for disordered CZTS is about 100 meV lower than for the ordered CZTS [57], resulting in a different position of PL bands arising from the same recombination. Moreover, recent PL studies showed that the radiative recombination could be different in the ordered and disordered structures [65]. In the disordered material, the concentration of different defect clusters is relatively high and radiative recombination involving these clusters that induce local bandgap decrease dominates at cryogenics temperatures. At temperatures below the order-to-disorder transition temperature, the concentration of defect clusters can be reduced. As a result, radiative

recombination involving deep acceptor defect with the ionization energy of about 200 meV is dominating in the PL spectra of ordered CZTS [65]. Both recombination channels, the one related to band gap energy fluctuations caused by the defect clusters and the other related to deep acceptor defects, are usually detrimental for solar cells.

In all of the studies reviewed, ordering annealing at a low temperature was observed to reduce the concentration of Cu_{Zn} and Zn_{Cu} defects, and consequently increased the effective bandgap (E_g^*). One would expect the V_{oc} deficit to reduce if the concentration of defects is decreased. However, so far no studies have reported this to occur in high-performance kesterite devices. Future work should continue to explore the link between ordering induced by low-temperature annealing and V_{oc} deficit in the kesterite-based devices.

1.5 Bandgap engineering

One of the most fundamental criteria for a semiconductor to be suitable for photovoltaic applications is the absorption of incident photons to create electron-hole pairs. For the absorption of the solar radiation, it is required to choose the bandgap of the absorbing material appropriately. The Shockley-Queisser limit, which describes the thermodynamic efficiency limit for photovoltaic solar energy conversion as a function of the bandgap of the absorber used in the single junction solar cell device, hereby gives the upper and lower limit for the bandgap [66]. For the solar spectrum, a maximum efficiency of around 30% can be achieved with materials with bandgaps between 1.0 and 1.5 eV [66]. To reach the ideal bandgap and improve the efficiency, bandgap engineering is possible. In a kesterite-based single junction solar cell, the ratio of S/Se has been modified in several studies [67-70]. The best efficiency (12.6%) was achieved by modifying the ratio of S/Se in the absorber material forming CZTSSe solid solutions [23]. However, it is very difficult to control the anion ratio of S/Se (and therefore, control the bandgap) precisely through the annealing processes. Therefore, another method to alter the bandgap by adjusting metal cations during the absorber synthesis, for example, by controlling the ratio of Zn/Cd [29, 71, 72] or Sn/Ge [73-75], may be a better alternative.

For most compound semiconductors, it is commonly accepted substitution of heavier atoms from the same group in the periodic table results in narrower bandgaps. As it is required to reduce the bandgap of CZTS for optimum absorption and higher efficiency, we can substitute Zn atom with Cd atom, which belongs to the same group of elements and is larger than Zn.

Synthesis of $\text{Cu}_2\text{Zn}_{1-x}\text{Cd}_x\text{SnS}_4$ ($0 \leq x \leq 1$) alloy thin films by the sol-gel method has been reported [71] to realize the goal of bandgap engineering in $\text{Cu}_2\text{ZnSnS}_4$ -based solar cells. Xiao *et al.* [71] reported that the optical bandgap of CZCdTS alloy could be modified continuously from 1.55 to 1.09 eV as Cd varies from 0 to 1, as determined by the optical absorption measurements. The bandgaps of the CZCdTS films, which were made by spin-coating the precursor

solutions followed by post-sulphurized treatment, determined by optical transmittance spectra were presented to be controlled linearly by adjusting the Cd/(Cd + Zn) ratios of the synthesis precursors from 1.35 ($x = 0$) to 1.15 eV ($x = 1.0$) [72]. In order to clarify the mismatch in the bandgap energies, the CZCdTS solid solutions in the form of monograin powders were synthesized and studied in this thesis (Paper I).

Lately, Su *et al.* [28] showed that the efficiency of $\text{Cu}_2\text{ZnSnS}_4$ solar cells could be enhanced up to 9.82% through partial Zn atom substitution with a Cd atom ($x = 0.4$) by forming the $\text{Cu}_2\text{Zn}_{1-x}\text{Cd}_x\text{SnS}_4$ ($x = 0-1$) solid solution. The substitution of Zn with Cd in CZTS induced the phase transformation from kesterite to stannite when $x > 0.6$. In addition, the microstructure of CZTS thin films was improved and the nature of secondary phases was changed to $\text{Zn}_{1-x}\text{Cd}_x\text{S}$ rather than pure ZnS. The variation of the Cd content was also found to change the depletion width, charge density, and series resistance in CZCdTS devices [29]. It was assumed that the variation of the parameters of a solar cell device as a function of the Zn/Cd ratio might be attributed to the change in the electronic structure of the bulk of the CZCdTS thin film. It is due to the phase transformation from kesterite to stannite, which in turn affects the band alignment at the CZCdTS/CdS interface and the charge separation at this interface.

Yan *et al.* [29] showed that the introduction of Cd to CZTS significantly reduced the band tailing, which was confirmed by the reduction in the difference between the photoluminescence peak position energy and optical bandgap (E_g) as well as by decreased Urbach energy. The microstructure, minority carrier lifetime, and electrical properties of the CZTS absorber were substantially improved by Cd alloying. In addition, X-ray photoelectron spectroscopy (XPS) analyses show that the partial Cd alloying slightly reduces the bandgap of CZTS via elevating the valence band maximum of CZTS. With these positive influences of Cd, over 11% power conversion efficiency (PCE) of the CZCdTS solar cell was achieved [29].

All these results suggest that further efficiency improvement of CZTS by engineering the absorber is possible.

1.6 Monograin powder technology

Solar cell technologies are traditionally divided into three generations. First generation solar cells are mainly based on silicon wafers. The benefits of this solar cell technology lie in their good performance, as well as their high stability. However, they are rigid and require a lot of energy in production. The second generation solar cells are based on thin film materials like amorphous silicon, CIGSe and CdTe, which have lower material consumption. Therefore, it has been possible to reduce production costs of these types of solar cells compared to the first generation. Third generation solar cells use organic materials such as small molecules or polymers. Still, the stability of these types of solar cells is still challenging [76].

Second generation solar cells can also be produced on flexible substrates. However, as the production of second generation solar cells still includes vacuum processes and high temperature treatments, there is still high energy consumption associated with the production of these solar cells [76]. There is also an alternative approach to prepare solar cell structures – by using powder materials. Powder technologies are the cheapest technologies for materials production.

Research and development of monograin layer solar cells at Tallinn University of Technology began in 1996 after a two-year period of investigations in the field of CuInSe_2 monograin powder growth [77]. Monograin is a single-crystalline powder particle consisting of one single crystal or several single crystalline blocks grown into compact grain [77]. The monograin layer (MGL) is a monolayer of about the same size powder grains embedded into organic resin. The idea of MGL as a construction element of optoelectronic devices was developed at Philips Laboratories in Eindhoven in 1967 [78].

The formation of monograin powders takes place during the heating process in the molten phase of the flux. Single crystals or single-crystalline powders can be obtained at temperatures above the melting point of the used salt at temperatures lower than the melting point of the semiconductor itself. Initial solid particles of low-solubility precursors react with each other in the molten salt media, and the formed solid particles of the product compound start to recrystallize and grow by the mechanism of Ostwald ripening [79].

The characteristics of monograin powder crystals are controlled by the selection of the synthesis temperature, as well as the nature and amount of the salt. The volume of the used molten salt has to exceed the volume of voids between precursor particles. In this case, the formed liquid phase is sufficient to repel both the solid precursor particles and the formed powder particles from each other and to avoid sintering caused by the contracting capillary forces arising in the solid – liquid phase boundaries. After the synthesis, the used salt is removed by washing with a suitable solvent and the released monograin powder is dried and sieved.

1.7 Secondary phases in $\text{Cu}_2\text{ZnSnS}_4$ and $\text{Cu}_2\text{CdSnS}_4$

High efficiency solar cells also require single-phase absorbers. As the existence region of single-phase $\text{Cu}_2\text{ZnSnS}_4$ is rather small [80], the outside of this single-phase region, the co-existence of one or more secondary phases with a CZTS phase is very likely.

The formation of secondary phases depends on the synthesis conditions. Cu_xS compounds can be expected for Cu-rich compositions, as well as for Sn- and Zn-poor stoichiometry. For Cu-poor or Sn-rich samples, a second quaternary compound $\text{Cu}_2\text{ZnSn}_3\text{S}_8$ (reported by Olekseyuk *et al.* in [80]) is also expected from the reaction of SnS_2 and CZTS at 700 °C. Highly conductive

phases of Cu-S and Cu-Sn-S compounds are detrimental for photovoltaic application of CZTS [81, 82] by creating shunting paths in the final devices.

Cu-poor and Zn-rich compositions are therefore desirable to suppress the formation of Cu-S and Cu-Sn-S detrimental phases and are usually implemented in the literature for the realization of high efficiency CZTS devices. As a result of the Cu-poor and Zn-rich composition, ZnS is expected as a single secondary phase for Zn-rich composition. It has quite high bandgap energy (3.54 eV), which could create insulator regions in the CZTS absorber layer, thus lowering the device performance. However, Cu-poor and Zn-rich composition has been found to be most suitable so far to obtain efficient devices from CZTS films [9, 21, 47, 49].

As the single phase in the quasi-binary system $\text{Cu}_2\text{SnS}_3 - \text{CdS}$ is shown with the line on the phase diagram [83], a slight deviation from the stoichiometry leads to the formation of Cu_2SnS_3 in Cu-rich side and CdS secondary phases in Cd-rich side, additionally to $\text{Cu}_2\text{CdSnS}_4$.

In the synthesis of $\text{Cu}_2\text{Zn}_{1-x}\text{Cd}_x\text{SnS}_4$ solid solutions, $\text{Zn}_{1-x}\text{Cd}_x\text{S}$ secondary phase forms in the ZnS-CdS system. The Zn/Cd ratio in $\text{Zn}_{1-x}\text{Cd}_x\text{S}$ depends on the ZnS/CdS ratio and has the same value as Zn/Cd ratio in $\text{Cu}_2\text{Zn}_{1-x}\text{Cd}_x\text{SnS}_4$ solid solution [84].

1.8 Summary of the literature review and objectives of the research

During the last decade, solar cells based on the CZTSSe absorber material have shown a significant increase in power conversion efficiency, from about 5.74% up to 12.7% [47, 7]. However, the continuing increase in efficiency has been slowing down. Several fundamental unsolved problems should be clarified for further improvement.

The studies reported in the literature on the properties of kesterite and stannite type absorber materials, and solar cells based on these materials can be summarized as follows:

- One of the most fundamental criteria for a semiconductor to be suitable for photovoltaic applications is the bandgap. As the bandgap of $\text{Cu}_2\text{ZnSnS}_4$ needs to be reduced for optimum absorption of the solar radiation and higher efficiency, the ratio of S/Se is modified in several studies. However, it is very difficult to control the anion ratio of S/Se (and therefore to control the bandgap) precisely through the annealing processes. Therefore, another method to alter the bandgap is by adjusting metal cations during the absorber synthesis, for example, by controlling the ratio of Zn/Cd. The bandgap values of $\text{Cu}_2\text{Zn}_{1-x}\text{Cd}_x\text{SnS}_4$ solid solutions reported in the literature depend on the synthesized method and also on the used analysis method. Systematic investigation is necessary to clarify the mismatches in bandgap values and find the

optimal ratio of Zn/Cd for a suitable bandgap for photovoltaic applications.

- The main limitation of the PCE in $\text{Cu}_2\text{ZnSnS}_4$ based solar cells is low open circuit voltage (V_{oc}) as compared to the bandgap energy value E_g . The reasons for the voltage losses in kesterite cells are still not clear. High concentration of defect complexes and defect clusters could cause bandgap fluctuations and electron-trapping states; also, existence of antisite defects in the absorber materials is detrimental to the solar cell performance. Thus, using a larger Cd atom to partially replace Zn may be one possible method to decrease the concentration of antisite defects. The other possibility to reduce the Cu-Zn disordering appears to be a low-temperature post-annealing treatment. Structural ordering should reduce the concentration of Cu_{Zn} and Zn_{Cu} defects, and consequently increase the effective bandgap. One would expect the V_{oc} deficit to reduce if the concentration of defects is decreased. However, so far this has not been reported to occur in high-performance kesterite devices.
- Despite the reported material properties of pure $\text{Cu}_2\text{CdSnS}_4$ that seem to be suitable for absorber material in photovoltaics, the performance of devices is still low. Main reason for poor performance of $\text{Cu}_2\text{CdSnS}_4$ solar cells is still unclear and more information about the optoelectronic properties is needed.

The aims of the present doctoral thesis were:

- to synthesize $\text{Cu}_2(\text{Zn}_{1-x}\text{Cd}_x)\text{SnS}_4$ ($x = 0-1$) solid solutions of monograin powders in KI molten salt and characterize the compositional, structural and optoelectronic properties of these powders to find the optimal Cd content in solid solutions for an ideal bandgap of $\text{Cu}_2(\text{Zn}_{1-x}\text{Cd}_x)\text{SnS}_4$ -based single junction solar cells;
- to study the influence of ordering-disordering in $\text{Cu}_2\text{ZnSnS}_4$ monograin powders on the compositional, structural and optical properties of these powders and on the performance of $\text{Cu}_2\text{ZnSnS}_4$ based monograin layer solar cells;
- to clarify the existence of disordering in stannite-type compounds and to study the influence of this phenomenon on the optoelectronic properties of $\text{Cu}_2\text{CdSnS}_4$ polycrystalline powder through low-temperature annealing.

2 EXPERIMENTAL

2.1 Preparation of powder samples

Monograin powder materials [published in Papers I, II, IV] studied in this thesis were synthesized from different purity self-synthesized binary compounds (CuS, ZnS, CdS, SnS) or commercially available elemental powders in the molten salt. The polycrystalline powder of $\text{Cu}_2\text{CdSnS}_4$ [Paper III] was synthesized from elemental Cu, Sn, S and CdS binary compound by solid-state reaction. Details about initial composition of studied materials and the experimental synthesis conditions for powder preparation are presented in Tables 2.1 and 2.2.

Table 2.1 Initial compositions of powders.

Sample	Cu	Cd	Sn	S	Flux	Temperature (°C)	Time (h)	Notes
1	100	0	0	100	0	740	120	
2	100	0	0	100	0	610	120	
3	100	0	0	100	0	740	120	
4	100	0	0	100	0	610	120	
5	100	0	0	100	0	740	120	
6	100	0	0	100	0	610	120	
7	100	0	0	100	0	740	120	
8	100	0	0	100	0	610	120	
9	100	0	0	100	0	740	120	
10	100	0	0	100	0	610	120	

The precursor's mixtures with or without flux (KI or CdI_2) were ground in desired amounts in an agate mortar. The milled precursor's mixture was placed in quartz ampoules, which were degassed under dynamic vacuum (continuous vacuum pumping) at temperature up to 100 °C (in case of using CdI_2 flux) or 270 °C (in case of using KI flux) and sealed by using $\text{C}_3\text{H}_8/\text{O}_2$ flame.

For the synthesis of monograin powders, the temperature of the muffle furnace was increased from room temperature (RT) to 740 °C (in case of using KI flux) and 610 °C (in case of using CdI_2 flux) with a rate of 4 degree/min and kept at elevated temperature for 120 h. The growth of monograin powder crystals was interrupted by cooling the ampoules naturally in the air. The flux was removed by leaching with deionized water in ultrasonic bath and released monograin powders were dried in the thermostat at 50 °C for 12 h. Dried powders were sieved into granulometric fractions between 38 to 100 μm . The sieving was performed on a vibratory sieve shaker Retsch AS 200. For future technological processes, the grains with diameters of 63-100 μm were selected.

Polycrystalline powder of $\text{Cu}_2\text{CdSnS}_4$ was synthesized by solid-state reaction in sealed evacuated quartz ampoules. The temperature of the muffle furnace was increased from RT to 200 °C with a rate of 10 degree/min. Sulphurization process of metal components was obtained by keeping the mixture at 200 °C for 24 h. Subsequently, the temperature of the furnace was increased to 900 °C with the rate of 12 degree/min and powder was homogenized at this temperature for 168 h. A complete homogenization was obtained by decreasing the temperature to 740 °C and keeping the powder at this temperature for 168 h. Finally, the powder was cooled from 740 °C to RT for 19 h.

Table 2.2 Experimental synthesis conditions for powder preparation.

Step	Temperature (°C)	Rate (°C/min)	Time (h)	Notes
1	RT to 200	10	-	Initial heating
2	200	-	24	Sulphurization process
3	200 to 900	12	-	Temperature increase
4	900	-	168	Homogenization
5	900 to 740	-	-	Temperature decrease
6	740	-	168	Final homogenization
7	740 to RT	-	19	Cooling

Detailed procedure of monograin and polycrystalline powder preparation and synthesis is described in experimental sections in Papers I, II, IV and III, respectively.

2.2 Post-treatments of $\text{Cu}_2\text{ZnSnS}_4$ monograin powders

Generally, during the synthesis of monograin powder, some part of precursor compounds is dissolved in the flux material at the growth temperature. In the cooling process, the dissolved material precipitates on the formed solid crystal surfaces. The removal of secondary phases from the surface of the monograins has been one of the major challenges to improve the performances of CZTS MGL solar cells. In this contribution, the complex etching with fresh-made 1% bromine methanol for 5 min followed by 10% KCN aqueous solution for 5 min

was performed for all powders used in the current experiments. According to studies [85, 86], bromine-based solution etching mainly removes Cu and Zn, leaving the crystal surface Sn- and chalcogenide-rich, which is removed by subsequent KCN etching.

After chemical etching, an annealing step at high temperature typically above 740 °C in S atmosphere is required to obtain high quality absorbers. A standard process in the CZTS monograin powder technology is the post-growth annealing of powder in quartz ampoules in a two-temperature-zone tubular furnace (see Figure 2.1) at 740 °C in the sulphur atmosphere of 10³ Torr pressure for 1 h. After high-temperature annealing, the ampoule with powder is normally cooled in air from 740 °C to RT for about 5 min.

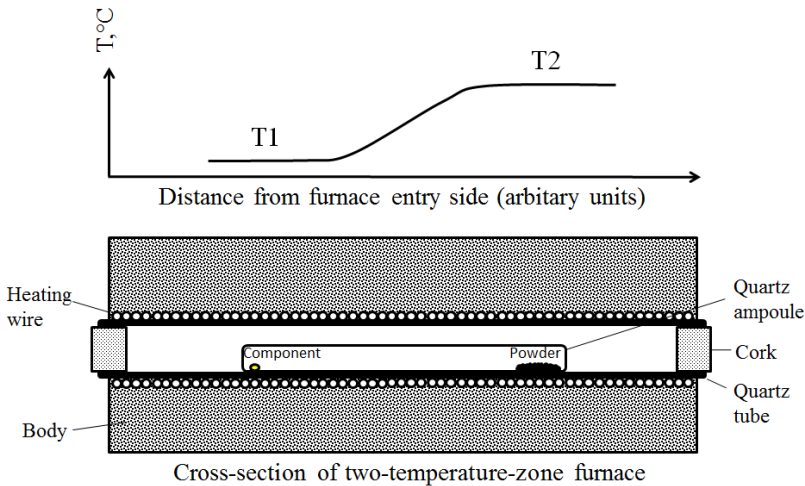


Figure 2.1 Scheme of tubular furnace and temperature profile along the ampoule in the furnace during heat treatment in the two-temperature-zone setup. T1 and T2 are the temperatures in component (sulphur) and material (monograin powder) zones, respectively.

The process parameters for chemical etching and thermal annealing are based on earlier studies [85-87].

2.2.1 Cooling parameters for Cu₂ZnSnS₄ monograin powders

According to the literature review, one possibility to modify the degree of Cu-Zn disordering is to use different cooling regimes after high-temperature (HT) treatments. Therefore, the influence of the cooling regime after HT-annealing in S atmosphere on the CZTS monograin powder properties and on the performance of the solar cells based on these powders was studied (CZTS-I) [Paper II]. The powders were cooled from 740 °C to RT by four different cooling times to obtain various degrees of ordering (see Table 2.3). The fastest cooling (named as Cooling A) rate was performed by quenching the ampoule with powder into cold water to freeze the HT thermal equilibrium of lattice

defects, corresponding to the state of maximum Cu-Zn disorder [56, 62]. The standard cooling (Cooling B, 5 min) was done in the monograin powder technology by cooling ampoules after HT-annealing in an air. The Cooling C (15 min), the ampoules together with special quartz tube that surrounded the ampoules was done in an air. The longest cooling (Cooling D, 510 min) was performed turning the heaters off and ampoules were cooled naturally with furnace to room temperature. Except for the fastest cooling, the other cooling profiles are presented in Figure 2.2.

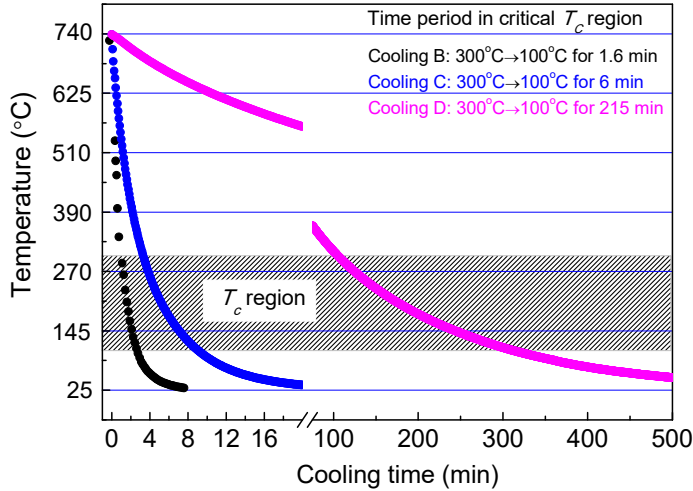


Figure 2.2 Temperature profiles for three different cooling rates. The temperature evolution registration during quenching in water is not presented in this figure, as the measurement was unfeasible.

As seen from Figure 2.2, the powders pass the temperature region near the T_c from 300 to 100 °C with different times. The parameters of cooling regimes are presented in Table 2.3.

Table 2.3 Parameters of cooling regimes after HT treatments.

CZTS-I	Cooling time from 740 °C to RT, min	Cooling time around T_c , min
Cooling A	Quenched	-
Cooling B	5 (standard)	1.6
Cooling C	15	6
Cooling D	510	215

All powders used in the cooling experiments had parallel samples. These samples were also used in later low-temperature experiments. In section 3.2.1.2, the influence of additional LT-annealing after different cooling regimes on the optoelectronic properties of CZTS monograin powder and solar cell devices is discussed [Paper II].

2.2.2 Low-temperature annealing of $\text{Cu}_2\text{ZnSnS}_4$ monograin powder

Another way to change the Cu-Zn ordering in the CZTS structure is low-temperature post-annealing at the temperature below the critical temperature ($T_c \sim 260$ °C) [52]. Therefore, after standard post-treatment of monograin powders in S atmosphere, followed by cooling from 740 °C to RT for 5 min, an additional annealing at low temperatures below T_c was studied (CZTS-II) [Paper II].

Experimental parameters for the low-temperature annealing study are presented in Table 2.4. After LT-annealing, all powders were cooled naturally in the air to RT.

Table 2.4 Experimental conditions for low-temperature annealing of CZTS-II.

Powder material	Annealing temperature, °C	Annealing time, min
CZTS-II	100	30, 60, 120, 240
	125	120, 240, 1440, 6720
	150	5, 15, 30, 120, 240, 10080
	175	5, 15, 30, 60, 120, 240
	200	3, 5, 15, 30, 60, 120
	225	5, 10, 30, 60, 120
	250	5, 10, 30, 60, 120

2.2.3 Low-temperature annealing of $\text{Cu}_2\text{CdSnS}_4$ polycrystalline powder

The theoretically predicted [43] existence of disordering in $\text{Cu}_2\text{CdSnS}_4$ was studied by applying low-temperature annealing similar to that used for CZTS studies.

Before low-temperature annealing study, the synthesized $\text{Cu}_2\text{CdSnS}_4$ polycrystalline powder was ground in an agate mortar and divided to equal amounts to the quartz ampoules, which were subsequently evacuated to 10^{-2} Torr vacuum and sealed with $\text{C}_3\text{H}_8/\text{O}_2$ flame. All sealed ampoules were heated up to 740 °C, annealed at this temperature for 1 h and then cooled by quenching into cold water. This annealing was done for healing out the mechanical damages on the powder particle surfaces caused by the grinding process.

As the critical temperature for $\text{Cu}_2\text{CdSnS}_4$ was not found in the literature, the low-temperature annealing study was done at the following temperatures (T_{ann}): 100 °C, 150 °C, 175 °C, 200 °C, 225 °C, 250 °C, 300 °C, 350 °C, and 400 °C for different times from 1 h to 2 weeks. After low-temperature annealing, the ampoules were quenched to cold water.

2.3 Fabrication of monograin layer solar cells

The post-treated monograin powders were used as absorber materials in MGL solar cells with the following structure: graphite/Cu₂(Zn,Cd)SnS₄/CdS/*i*-ZnO/ ZnO:Al/Ag. The scheme of MGL based solar cell structure is shown in Figure 2.3.

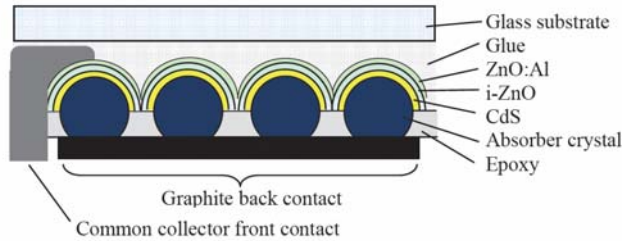


Figure 2.3. Scheme of monograin layer solar cell [88].

The fabrication of monograin layer solar cells started with the formation of the photoactive membrane. The thin epoxy layer stripe with the controlled thickness was applied on the temperature stable plastic foil by the doctor blade method. The thickness of the epoxy was fixed by the grain size used for membrane preparation. It should be at least 40% of the grain size. Powder grains with similar size in excess were rolled over the epoxy layer for several times. The lower grains adhered to the resin and remaining powder was shaken off. Finally, the applied grains were pressed into epoxy so that the upper part (approximately 50% of grain size) remained uncovered. After polymerization of epoxy, the monograin layer membrane was ready for the next technological processes.

To form the *p-n* junction, CdS thin film with approximately 45 nm was deposited on top of the MGL using the chemical bath deposition (CBD) method by a standard recipe developed in the Laboratory of Photovoltaic Materials, TTÜ. The bath solution contained NH₄OH, CdI₂ as Cd source and SC(NH₂)₂ as S precursor. Before CdS buffer layer deposition, 10% KCN etching was used to remove possible SnS₂ or S deposits on the crystal surface, which could be formed after annealing in the sulphur vapor. Chemical etching was performed at room temperature, as reported in [85]. To increase shunt resistance, an *i*-ZnO layer with a thickness of about 40-45 nm and a conductive ZnO:Al layer with a thickness of about 350-400 nm were deposited using the radio frequency magnetron sputtering system to act as a top electrode.

Finally, to intensify the collection of charge carriers, the silver nanorods and conductive silver paste grid contacts were applied on top of the bilayer of ZnO window, and the structure was glued onto a glass substrate. After removal of the plastic foil substrate from the top of the structure, the surfaces of powder crystals were released from the epoxy by etching it in the concentrated H₂SO₄ for determined times. After opening of back contact areas, the abrasive treatment was applied. Subsequently, graphite paste for the back contact was used.

2.4 Characterization of monograin and polycrystalline powders

2.4.1 Material characterization

This section presents the analytical techniques used to characterize the monograin powders and monograin layer solar cells. Detailed information about the instruments and measurements is given in the experimental sections of Papers I-IV.

Scanning electron microscopy

The morphology of synthesized powder crystals was studied by high-resolution scanning electron microscope (HR-SEM) Zeiss ULTRA 55 [I-IV]. The SEM images were made by Dr. Valdek Mikli at Tallinn University of Technology.

Energy dispersive X-ray spectroscopy

The bulk composition [I-IV] and elemental mapping [III] of the synthesized powder crystals were analyzed by energy dispersive X-ray spectroscopy (EDX) on Zeiss (HR-SEM) ULTRA 55 equipped with a backscattered detector and Bruker Esprit 1.8 system with an accelerating voltage of 20 kV. Compositional analysis and elemental mapping were made from polished cross-section of individual crystals. The measurement error for elemental analysis is about 0.5 at%. The EDX measurements were carried out by Dr. Valdek Mikli at Tallinn University of Technology.

X-ray diffraction

The crystalline structure of monograin powders [I] was characterized by X-ray diffraction (XRD) using a Rigaku Ultima IV diffractometer with monochromatic Cu K α radiation $\lambda = 1.54056 \text{ \AA}$ at 40 kV and 40 mA, using a D/teX Ultra silicon strip detector. For the identification of crystal phases, the Joint Committee on Powder Diffraction Standards (JCPDS) database was used. Lattice parameters were calculated using Rigaku PDXL Version 1.4.0.3 software. The XRD measurements of monograin powders were carried out by Dr. Arvo Mere at Tallinn University of Technology.

XRD patterns of Cu₂CdSnS₄ polycrystalline powders [III] were recorded on a Bruker AXS X-ray diffractometer D5005 using Cu K α 1 radiation $\lambda = 1.54056 \text{ \AA}$ with variable slit V12. Obtained data were analyzed by using the International Centre for Diffraction Data (ICDD) PDF 2015 database. The XRD patterns of polycrystalline powders were recorded by Dr. Rainer Traksmaa at Tallinn University of Technology.

Room-temperature micro-Raman spectroscopy

The phase composition of the powders [I-IV] was studied by room-temperature micro-Raman spectroscopy using Horiba's LabRam HR 800 spectrometer equipped with a multichannel CCD detection system in the backscattering configuration using a 532 nm laser line with a spot size of 5 micrometers. The measurement error in Raman peak position is 0.5 cm^{-1} . The Raman measurements of powders were carried out by Dr. Taavi Raadik and by Dr. Maarja Grossberg at Tallinn University of Technology.

The same equipment was used for room temperature photoluminescence (RT-PL) measurements. The measurement error in the values of the PL peak position is 0.005 eV. RT-PL measurements were made by Dr. Maarja Grossberg at Tallinn University of Technology.

Photoluminescence spectroscopy

For low temperature PL measurements [I-IV], the powder crystals were mounted in the closed-cycle He cryostat and cooled down to 10 K. The 658 nm or the 441 nm He-Cd laser line was used for PL excitation and the spectra were detected by using an InGaAs detector. The measurement error in the values of the PL peak position is 0.005 eV. The PL measurements were carried out by Dr. Maarja Grossberg at Tallinn University of Technology.

2.4.2 Solar cell characteristics

Completed solar cell structures were characterized by dark and light current-voltage (I - V) and quantum efficiency measurements (QE).

Current-Voltage measurements

Several parameters were used to characterize the efficiency of the solar cells. I - V curves were measured to evaluate the open-circuit voltage (V_{oc}), short-circuit current density (J_{sc}), fill factor (FF) and efficiency (η) of the monograin layer solar cells. Measurements were performed using Keithley 2400 source meter in dark and under standard test conditions light with illumination intensity of 100 mW/cm^2 (AM 1.5) [II, IV]. The measurement error in V_{oc} values can be considered up to 10 mV.

Quantum efficiency measurements

Unfortunately, the evaluation of E_g from the UV-VIS reflectance spectra of monograins is rather challenging. Quantum efficiency (QE) analysis is an alternative method that can be used to estimate the effective bandgap energy E_g^* of the synthesized absorber materials [89].

Spectral response measurements were performed in the spectral region of 350-1235 nm using a computer controlled SPM-2 prism monochromator. The generated photocurrent was detected at 0 V bias voltage at RT by using a 250 W halogen lamp. The QE measurements were carried out by Dr. Mati Danilson at Tallinn University of Technology.

3 RESULTS AND DISCUSSION

The following sections, 3.1–3.3, report the results of a systematic study of the structural and optical properties of the CZCdTS solid solutions, effect of structural disordering of CZTS on the material properties and solar cell performance, and modification of optical properties of $\text{Cu}_2\text{CdSnS}_4$ polycrystalline powder by the low-temperature annealing process. These results have been published in Papers I–IV.

3.1 Zn substitution by Cd in $\text{Cu}_2\text{ZnSnS}_4$ monograin powders

3.1.1 Composition of $\text{Cu}_2(\text{Zn}_{1-x}\text{Cd}_x)\text{SnS}_4$ monograin powders

$\text{Cu}_2(\text{Zn}_{1-x}\text{Cd}_x)\text{SnS}_4$ solid solutions were synthesized by the monograin powder technology, the experimental synthesis conditions of which were presented in Section 2.1.

In order to study the influence of Zn substitution by Cd on the bulk composition of powder crystals, EDX analysis from mechanically polished crystals was performed. As presented in Table 2.2, the ratios of $[\text{Cu}]/[\text{Sn}]=1.85$ and $[\text{Cu}]/([\text{Cd}]+[\text{Zn}]+[\text{Sn}])=0.88$ were kept constant in precursor mixtures and the ratio of $[\text{Cd}]/([\text{Cd}]+[\text{Zn}])$ was varied from 0 to 1. The average compositional ratios of elements in the synthesized CZCdTS solid solutions determined from EDX analysis are listed in Table 3.1.

Table 3.1 Compositional ratios of $\text{Cu}_2(\text{Zn}_{1-x}\text{Cd}_x)\text{SnS}_4$ monograin powders.

[Cd]/ ([Cd]+[Zn]) in precursors	Compositional ratios in powder				
	[Cd]/ ([Cd]+[Zn])	[Cu]/ ([Cd]+[Zn]+[Sn])	([Cd]+[Zn])/ [Sn]	[Cu]/[Sn]	[S]/[Met]
0	0	0.93	1.03	1.90	1.01
0.2	0.18	0.92	1.06	1.89	1.02
0.4	0.38	0.89	1.08	1.87	1.03
0.6	0.57	0.90	1.05	1.84	1.03
0.8	0.78	0.90	1.02	1.82	1.02
1	1	0.92	0.97	1.82	1.04

The results confirm that the value of $x = [\text{Cd}]/([\text{Cd}]+[\text{Zn}])$ in synthesized powders is close to the input value of x in precursors. It can be seen that the ratio of $[\text{Cu}]/[\text{Sn}]$ in the monograin powders decreases by increasing the Cd content in precursors. But the ratio of $[\text{Cu}]/([\text{Cd}]+[\text{Zn}]+[\text{Sn}])$ in all synthesized powders is higher than the same ratio in precursor mixtures (0.88), i.e. the final powders are more Cu-rich than the Cu content in the precursor mixtures. The ratio of $([\text{Cd}]+[\text{Zn}])/[\text{Sn}]$ decreased by increasing the Cd content and powders contain separately secondary phase crystals like $\text{Zn}_{1-x}\text{Cd}_x\text{S}$ or CdS. SEM images of the typical Cd-rich monograin powders are presented in Figure 3.1(a) and (b). It is in good agreement with the phase diagram of the quasi-binary system

Cu_2SnS_3 - CdS presented in [83], where a slight deviation from the stoichiometry in Cd-rich side leads to the formation of the CdS secondary phase.

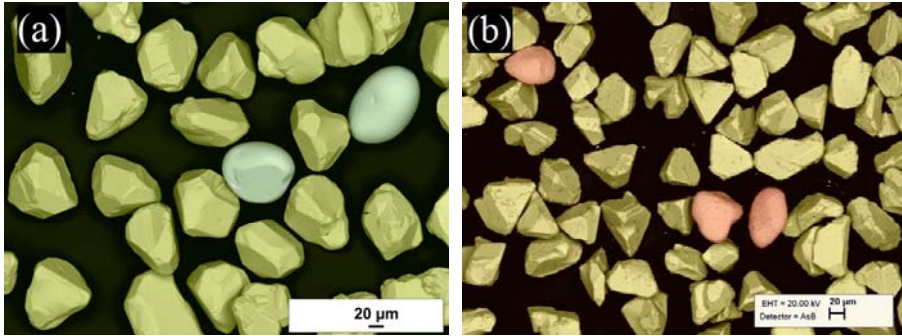


Figure 3.1 SEM image of $\text{Cu}_2\text{CdSnS}_4$ (a) and $\text{Cu}_2(\text{Zn}_{1-x}\text{Cd}_x)\text{SnS}_4$ (b) monograin powder. Crystals with round shape are determined as CdS and $\text{Zn}_{1-x}\text{Cd}_x\text{S}$ secondary phase, respectively.

Secondary phase crystals are visually very easily recognized because of the round shape. The ratio of $[\text{Zn}]/[\text{Cd}]$ in $\text{Zn}_{1-x}\text{Cd}_x\text{S}$ crystals is the same as in primary CZCdTS crystals, as shown in [84].

3.1.2 Influence of the Cd content on $\text{Cu}_2\text{ZnSnS}_4$ structural properties

3.1.2.1 X-ray diffraction analysis

Figure 3.2 shows the XRD patterns of monograin powders of CZCdTS solid solutions. The major diffraction peaks are indexed as corresponding to the (112), (200), (220), (312) and (332) planes of kesterite phase of $\text{Cu}_2\text{ZnSnS}_4$ (ICDD PDF2008, 01-075-4122) and stannite phase of $\text{Cu}_2\text{CdSnS}_4$ (ICDD (PDF2008, 00-029-0537). Figure 3.2 (a) shows the enlarged view of the (112) diffraction peaks. The peaks are shifted to the lower angle side with an increasing Cd content in the CZCdTS solid solutions.

The splitting of the profiles of (220) and (204) reflections due to the lattice distortion caused by the replacement of Zn by Cd for different x values is shown in Figure 3.2 (b). The splitting of the (220) peak increases up to $x = 0.4$. Then, besides the splitting, the high angle peak (204) appears and both (220) and (204) peaks are visible separately. The high angle peak (204) narrows with the increasing Cd content.

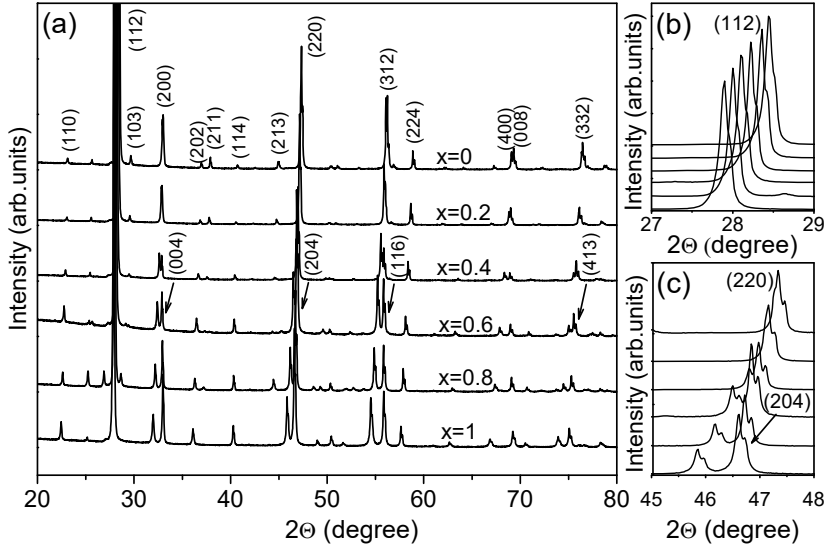


Figure 3.2 (a) XRD patterns of monograin powders of $\text{Cu}_2(\text{Zn}_{1-x}\text{Cd}_x)\text{SnS}_4$ solid solutions with $0 \leq x \leq 1$; (b) enlarged view of the (112) diffraction peaks and (c) splitting of the profiles of the (220) and (204) reflection.

Lattice constants for all powders were calculated from the XRD data (Figure 3.3). The a -axis lattice constant increases almost linearly from 5.433 to 5.593 Å as the Cd content increases from 0 to 1. The expansion of the lattice in this direction can be attributed to the larger ion radius of Cd than that of Zn or Cu. The simplest possibility is that Cd substitutes other metal atoms at their sites in the crystal lattice of CZCdTS. As the theoretically calculated substitution energies of Cd atoms at Cu, Sn and Zn atom sites in the CZTS lattice are $E_{\text{sub}}(\text{Cd}_{\text{Cu}}) = 0.69$ eV, $E_{\text{sub}}(\text{Cd}_{\text{Sn}}) = 1.07$ eV and $E_{\text{sub}}(\text{Cd}_{\text{Zn}}) = 0.53$ eV [90], the isoelectronic substitution of Cd at the Zn site is most likely.

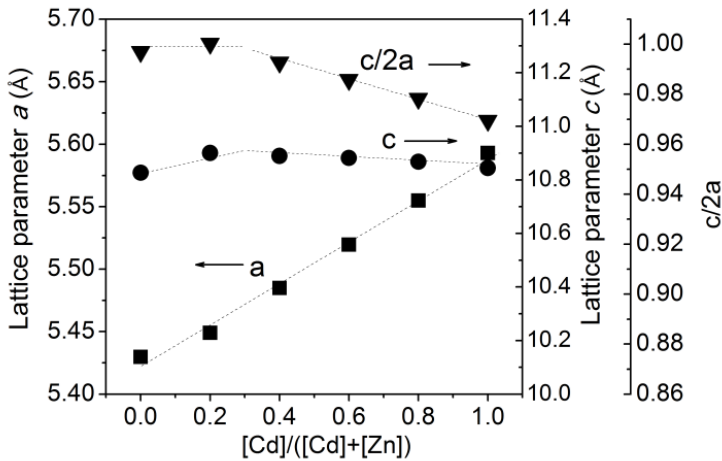


Figure 3.3 Lattice parameters of a , c and $c/2a$ as a function of the Cd content in $\text{Cu}_2(\text{Zn}_{1-x}\text{Cd}_x)\text{SnS}_4$.

The ratio of the lattice parameters $c/2a$ for CZCdTS in dependence of chemical composition is shown also in Figure 3.3. Schorr *et al.* carried out a neutron diffraction study of the $\text{Cu}_2\text{Fe}_{1-x}\text{Zn}_x\text{SnS}_4$ solid solutions and found that the ratio of the lattice constants $c/2a$ is equal to or greater than 1.0 for kesterite-type structure [31]. According to this, we could assume that CZCdTS solid solutions have kesterite-type structure in the region $0 \leq x \leq 0.3$ and in the region $0.4 \leq x \leq 1$ they exist in a stannite-type structure. Still, Su *et al.* [28] showed that the substitution of Zn with Cd in CZTS induced the phase transformation from kesterite to stannite when $x > 0.6$.

3.1.2.2 Raman analysis

In order to find out the existence of the secondary phases and confirm the stannite-kesterite transition point, the Raman measurements were performed. A linear shift of the A_1 Raman mode of CZCdTS towards lower wavenumbers (from 338 to 332 cm^{-1}) with an increasing Cd content in powders is demonstrated in the region $0 \leq x < 0.4$ (Figure 3.4).

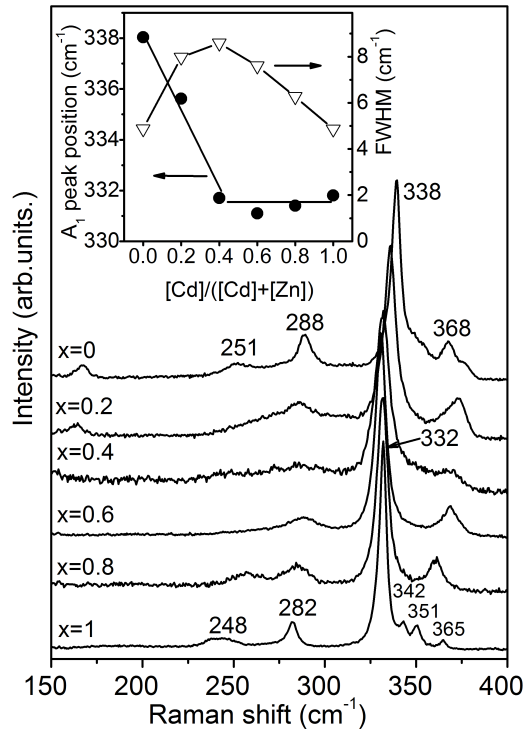


Figure 3.4 Raman spectra of $\text{Cu}_2(\text{Zn}_{1-x}\text{Cd}_x)\text{SnS}_4$ ($0 \leq x \leq 1$) monograin powders. Inset graph: Frequency and FWHM of the A_1 Raman mode versus the Cd content in $\text{Cu}_2(\text{Zn}_{1-x}\text{Cd}_x)\text{SnS}_4$.

Subsequent increase of the Cd concentration did not change the frequency of A_1 mode. The other Raman peaks for $\text{Cu}_2\text{ZnSnS}_4$ and for $\text{Cu}_2\text{CdSnS}_4$ correspond well to data in Paper IV and in [91-93]. No secondary phases were observed in the spectra of the crystals. The frequency and full width at half maximum (FWHM) of the main A_1 mode versus the chemical composition of the solid solution are plotted in the inset graph of Figure 3.4. A significant broadening from 5 to 8 cm^{-1} of the A_1 mode for powder with the value of $x = 0.4$ is observed. This could be attributed to the existence of disorder effects in the mixed crystals related to the structural transition from kesterite to the stannite structure. Both pure phases, CZTS and CCdTS, present equally narrow A_1 modes.

3.1.3 Influence of the Cd content on $\text{Cu}_2\text{ZnSnS}_4$ optical properties

Optical properties are characterized by low-temperature ($T = 10$ K) PL measurements. Normalized PL spectra of CZCdTS solid solutions with different Cd content are presented in Figure 3.5.

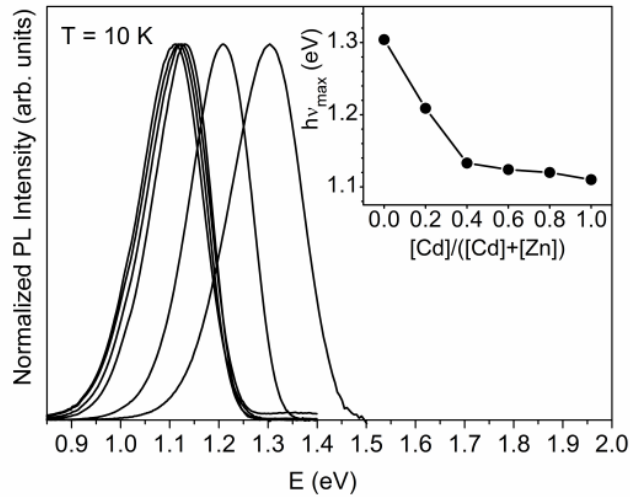


Figure 3.5 Normalized low-temperature PL spectra of $\text{Cu}_2(\text{Zn}_{1-x}\text{Cd}_x)\text{SnS}_4$ ($0 \leq x \leq 1$) monograin powders. Inset graph shows the dependence of the PL band position on the x value.

Low-temperature PL spectrum consists of one broad asymmetric PL band at 1.3 eV in $\text{Cu}_2\text{ZnSnS}_4$ and at 1.1 eV in $\text{Cu}_2\text{CdSnS}_4$. PL bands with such an asymmetric shape are often observed in multinary compounds that contain large concentrations of charged defects [92]. A shift of the PL band of CZCdTS monograin powders towards lower energies with an increasing Cd content is observed in the region $0 \leq x < 0.4$. Further increase in the Cd concentration did not change the PL band position significantly.

To estimate the bandgap values of the synthesized CZCdTS absorber materials, the external quantum efficiency (EQE) analyses were used. The normalized EQE spectra of MGL solar cells based on $\text{Cu}_2(\text{Zn}_{1-x}\text{Cd}_x)\text{SnS}_4$ solid solutions show a shift of the absorption edge to longer wavelength in the region $0 \leq x < 0.4$ (Figure 3.6). E_g^* values calculated from EQE measurements for $\text{Cu}_2\text{ZnSnS}_4$ and $\text{Cu}_2\text{CdSnS}_4$ devices are 1.55 eV and 1.37 eV, respectively. The linear change of the effective bandgap from 1.55 eV to 1.4 eV was observed in the region $0 \leq x < 0.4$ and subsequent increasing of the Cd content in the absorber material changed the bandgap value only down to 1.37 eV (inset graph in Figure 3.6).

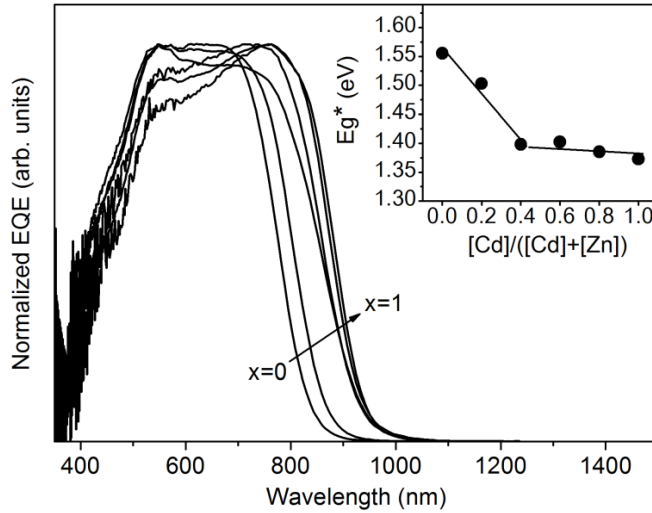


Figure 3.6 Normalized EQE spectra of $\text{Cu}_2(\text{Zn}_{1-x}\text{Cd}_x)\text{SnS}_4$ monograin layer solar cells. Inset graph presents the corresponding bandgap energy values determined from EQE measurements depending on the Cd content.

Based on the EQE and low-temperature PL results, we propose that in the kesterite-structured CZCdTS, the bandgap of the material can be changed in a larger extent by substituting Zn with Cd than in the stannite-structured CZCdTS. In addition, we determined (Paper IV) the room-temperature band gap energy of CCdTS 1.4 eV that is much larger than observed in the previous studies [71, 72]. Moreover, the large distance between the low-temperature PL band position and the bandgap energy of the CZCdTS material indicates a radiative recombination involving deep defects throughout the whole solid solution series. The radiative recombination mechanisms in CZTS and CCdTS are analyzed in more detail in Sections 3.2.1.2 and 3.3.2, respectively.

Summary of Zn substitution by Cd in $\text{Cu}_2\text{ZnSnS}_4$ monograin powders

$\text{Cu}_2(\text{Zn}_{1-x}\text{Cd}_x)\text{SnS}_4$ ($x = 0-1$) entire range of solid solutions of monograin powders in KI molten salt were synthesized. As $[\text{Cd}]/([\text{Cd}]+[\text{Zn}])$ in the synthesized powders and in precursor's mixture is quite close, it can be

concluded that Cd incorporation to the $\text{Cu}_2\text{ZnSnS}_4$ material is available and controllable. The major diffraction peaks are indexed as corresponding to the (112), (200), (220), (312) and (332) planes of kesterite phase of $\text{Cu}_2\text{ZnSnS}_4$ and stannite phase of $\text{Cu}_2\text{CdSnS}_4$. Split of (220) peak into (220) and (204) peaks confirms the transition from kesterite to stannite-type structure from the Cd content around $x = 0.4$ in $\text{Cu}_2(\text{Zn}_{1-x}\text{Cd}_x)\text{SnS}_4$ solid solutions. Calculated ratios of lattice parameters $c/2a$ also revealed the phase transition from kesterite to stannite. The Raman A_1 mode, PL band position and bandgap energy of $\text{Cu}_2(\text{Zn}_{1-x}\text{Cd}_x)\text{SnS}_4$ solid solutions showed the linear shift from 338 to 332 cm^{-1} , from 1.3 to 1.1 eV and from 1.55 to 1.4 eV, respectively with an increasing Cd content in the region $0 \leq x < 0.4$. Subsequent increase of the Cd content in solid solutions did not change these values significantly. The results of this study suggest that the x value around 0.4 has an optimal bandgap of 1.4 eV and could be a suitable material for the absorber layer in single junction solar cells. This result is in good agreement with the study [29], where the highest PCE of $\text{Cu}_2(\text{Zn}_{1-x}\text{Cd}_x)\text{SnS}_4$ solid solutions (11.5%) is achieved with the Cd content $x = 0.4$.

3.2 Disordering studies in $\text{Cu}_2\text{ZnSnS}_4$ monograin powders

As discussed in Section 1.4, disordering in the Cu-Zn planes of the kesterite crystal structure occurs and is proposed to be a possible reason for low V_{oc} . The degree of Cu-Zn disordering can be changed by using different cooling regimes after high temperature treatments or low-temperature post-annealing at the temperature below the critical temperature [52]. To study the disordering phenomenon in monograin powders, the influence of cooling rate on CZTS-I powder materials properties was investigated and for low-temperatures (LT), annealing studies were used CZTS-II powder [Paper II].

3.2.1 Influence of cooling rate on $\text{Cu}_2\text{ZnSnS}_4$ properties

3.2.1.1 Compositional analysis

Compositional analyses by EDX were made from the polished cross-section of individual crystals of CZTS powders cooled from 740 °C to RT by using different cooling rates. For each of the cooling conditions, the analysis was performed on at least eight different polished crystals. The average concentration ratios of elements in CZTS powder crystals are presented in Table 3.2.

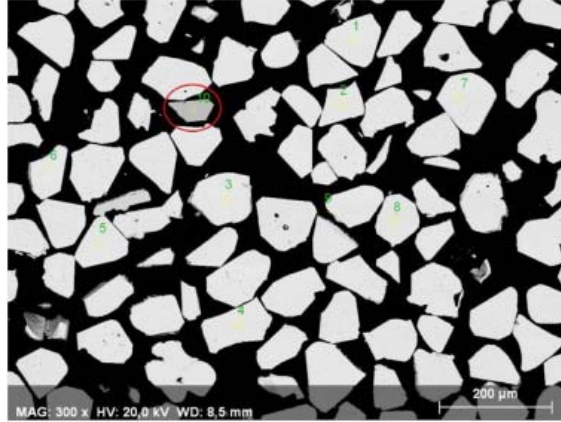


Figure 3.7 SEM image of polished cross-section of individual crystals of CZTS powder. The highlighted red circle indicates darker gray area, signifying secondary phase of ZnS.

Table 3.2 Compositional ratios of CZTS powders cooled from 740 °C to RT after S-treatment by using different cooling times. PL band positions and corresponding values of V_{oc} for solar cells based on these powders before and after additional LT-annealing.

Cooling regime	Parameters after different cooling regimes					Parameters after additional LT-annealing	
	[Cu]/([Zn]+[Sn])	[Zn]/[Sn]	[S]/[Met]	V_{oc} (mV)	PL _{max} (eV)	V_{oc} (mV)	PL _{max} (eV)
Cooling A	0.91	1.05	1.00	582	1.21	613	1.31
Cooling B	0.92	1.07	1.00	685	1.26	759	1.34
Cooling C	0.92	1.06	1.00	724	1.29	748	1.35
Cooling D	0.91	1.06	1.00	648	1.35	691	1.35

It can be seen that the bulk composition of CZTS monograin powders did not change significantly by increasing the cooling time after post-treatment. Only the ZnS secondary phase as separate crystals in the powders was detected and it is usually found to be present in CZTS monograin powders with Zn-rich composition (see Figure 3.7).

3.2.1.2 Photoluminescence and Raman results

Previously, the Cu–Zn disordering has been probed by Raman spectroscopy [52, 53, 94] and by PL measurements [57, 61]. Scragg *et al.* showed that there is remarkable correlation between the RT-PL peak energy and the order parameter S in CZTS. In the most ordered sample ($S \sim 0.8$), the RT-PL peak energy reaches 1.43 eV [57]. It was shown in our group’s previous study that there is a correlation in PL peak energies ($T = 10$ K) and the degree of Cu-Zn ordering [51]. PL and RT-PL were therefore used to estimate the degree of Cu-Zn ordering in studied CZTS monograin powders.

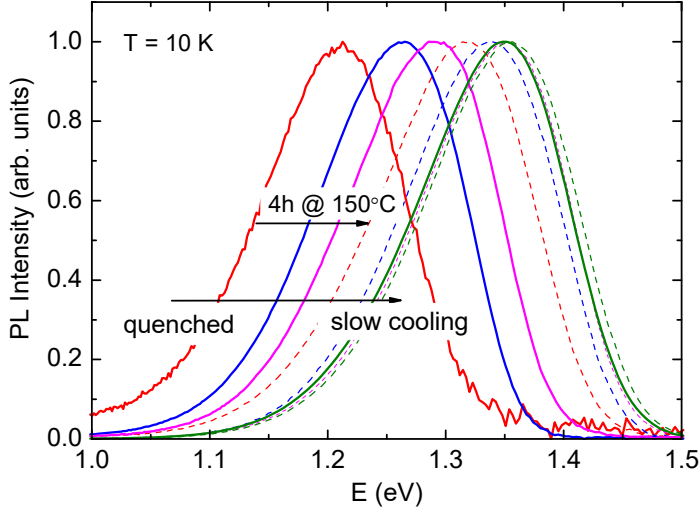


Figure 3.8 PL spectra of CZTS monograins with different cooling regimes are shown by solid lines and the parallel samples, subsequently annealed at 150 °C for 4 h, are shown by dashed lines with the same colors.

PL studies showed that slower cooling of CZTS monograin powders after HT-treatment shifted the typical broad asymmetric PL band position from 1.21 eV to 1.35 eV (~140 meV) (Figure 3.8). As mentioned in experimental section 2.2.1, all powders used in the cooling experiments were additionally annealed at 150 °C for 4 h. The annealing parameters were selected from the results of Section 3.2.2.

The additional annealing at 150 °C for 4 h after different cooling processes shifts the PL band position to a higher energy side, giving a hint to a further increase in the ordering degree (the PL band positions are listed in Tables 3.2). The shift of the PL band position of the slowest cooled powder by additional LT-annealing is only 5 meV, indicating that maximum ordering is already reached with the first cooling step. The behavior of the PL bands with increased Cu-Zn ordering is in correspondence with our previous PL study of CZTS with different cooling regimes [61]. It was shown that the shift of the PL bands is caused by two processes – improved Cu-Zn ordering of the crystals leading to increased bandgap energy by about 100 meV and change in the recombination type from band to tail to band to impurity type, the latter involving deep acceptor defect with the ionization energy of about 200 meV.

Scragg *et al.* measured the 785-nm Raman spectra of nominally ordered and disordered CZTS films and calculated the ratio of $Q = I(m_{2A}) / I(m_{3A})$. $I(m_{2A})$ and $I(m_{3A})$ are the Raman peak intensities for the A modes at 288 and 304 cm^{-1} , showing that there exists the correlation: the larger the Q value, the more ordered is the structure [52]. Studies on our CZTS monograin powders have demonstrated that different crystal planes show different intensities of the Raman peaks used for calculating Q values; therefore, we have used the FWHM of the A_1 mode to evaluate the degree of ordering. In the present study, the

FWHM of the A_1 Raman peak was found to decrease from 6.5 to 3.6 cm^{-1} for the best performed CZTS monograin powder after additional LT-annealing (see Figure 3.9). A similar trend was observed in the RT-PL spectra (Figure 3.10), where the band-band emission was detected.

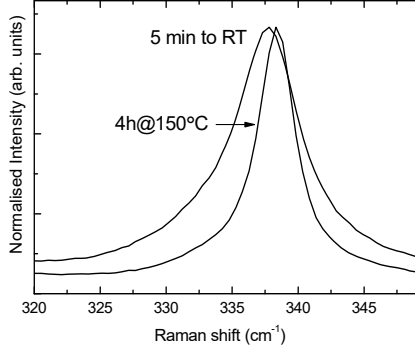


Figure 3.9 The shift in the FWHM of the A_1 Raman peak of the best performing CZTS monograin powder due to the LT-annealing

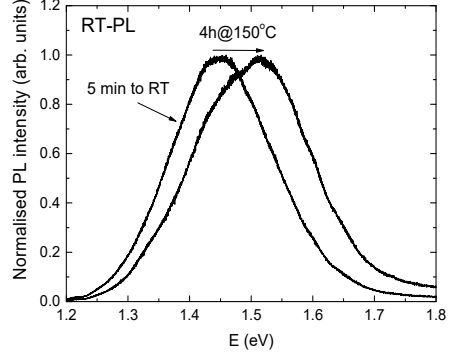


Figure 3.10 The shift in the RT-PL band position of the best performing CZTS monograin powder due to the LT-annealing.

Although the PL band position of the slowest cooled powder indicates the most ordered material, interestingly, the value of V_{oc} for corresponding CZTS monograin layer solar cell is not the highest (Table 3.2). The value of V_{oc} increases from 582 to 724 mV by increasing the time of cooling up to 15 min from 740 °C to RT, but further increase of the cooling time results in lower values of V_{oc} (648 mV) for the corresponding solar cell. This could be explained by the change in the radiative recombination mechanism since in the slowest cooled powder, the deep trap (~ 200 meV) related recombination dominates and reduces the positive effect of the bandgap increase to the V_{oc} in the most ordered material.

Therefore, we can conclude that the change in the defect structure of CZTS monograins accompanying the improved Cu-Zn ordering is most probably leading to the change in the Fermi level position determining the V_{oc} value. This is in agreement with the results of Bourdais *et al.* [54], showing that the bandgap changes induced by the Cu-Zn disorder are not fully responsible for the V_{oc} deficit in the kesterite solar cells. We should state here that besides changes in the bulk, the presence of secondary phases and compositional changes in the near surface layer induced by very slow cooling after sulphur treatment resulting in changed CZTS/CdS interface properties can be responsible for the decrease in the solar cell parameters, including V_{oc} . Since ZnS was found to be present in all our samples, we can exclude its influence on the changes in PL spectra and solar cell parameters. The studies of junction formation between ordered CZTS and buffer layer are a subject for further studies.

3.2.2 Impact of low-temperature annealing on the CZTS monograin layer solar cells

As a result of the experiments in Section 3.2.1, the best performing solar cell is based on the powder that was cooled from 740 °C to RT for 5 min (CZTS-I in Figure 3.11). The same cooling regime was used for the second powder (CZTS-II in Figure 3.11), where the powders were additionally annealed at different temperatures from 100 to 250 °C for different times. The difference between the powders CZTS-I and CZTS-II is presented in Table 2.2. The values of V_{oc} of CZTS MGL solar cells in dependence of LT-annealing at temperatures from 100 to 250 °C for different times are presented in Figure 3.11.

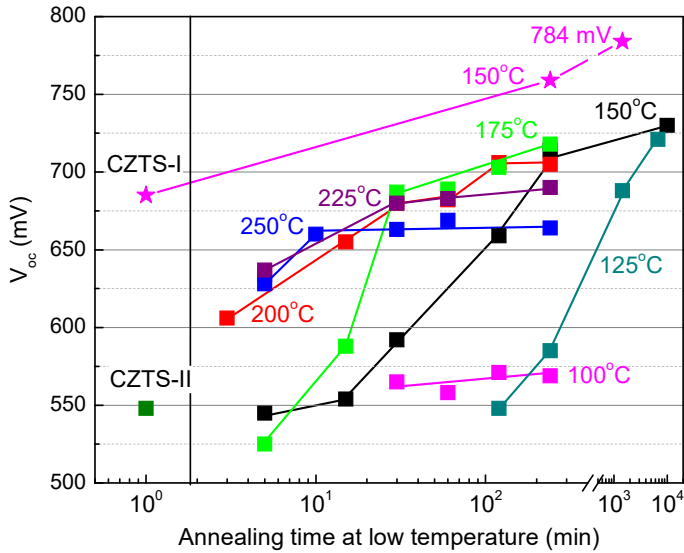


Figure 3.11 Evolution of V_{oc} of MGL solar cells based on CZTS-II powders (squares) by additional annealing at different temperatures as dependent on time. Improvement of V_{oc} for MGL solar cell based on CZTS-I by additional annealing at 150 °C for 4 and 24 h is shown by stars.

In this study, considering the V_{oc} values achieved at different annealing times at different temperatures, we concentrated to PL and Raman spectra that were measured for the powders annealed at 150 °C for 4 h. PL peak positions and corresponding values of V_{oc} are shown in Figure 3.12 as a function of LT-annealing temperature. The behavior of PL band position and the corresponding V_{oc} value are in good correlation. There is a continuous shift of the PL band maxima by 100 meV from 1.25 to 1.35 eV accompanied by the decrease in FWHM of the A_1 Raman peak with the increasing temperature of the LT-annealing from 100 to 175 °C. Further increase in the LT-annealing temperature resulted in PL band positions at lower energy values and in an increase in the FWHM of the A_1 Raman peak, indicating an increasing disordering. Again, the same trend was observed in the RT-PL spectra, where the band-band emission was detected.

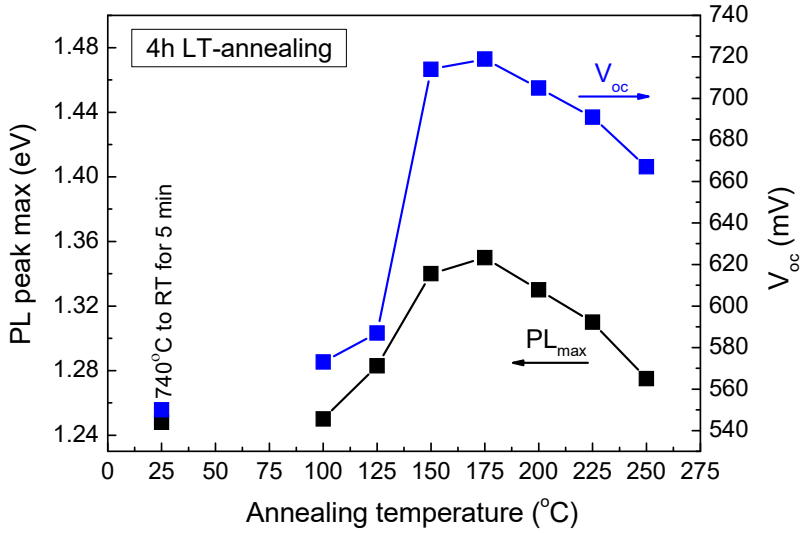


Figure 3.12 PL peak positions of powders LT-annealed at different temperatures for 4 h and V_{oc} values of corresponding MGL solar cells.

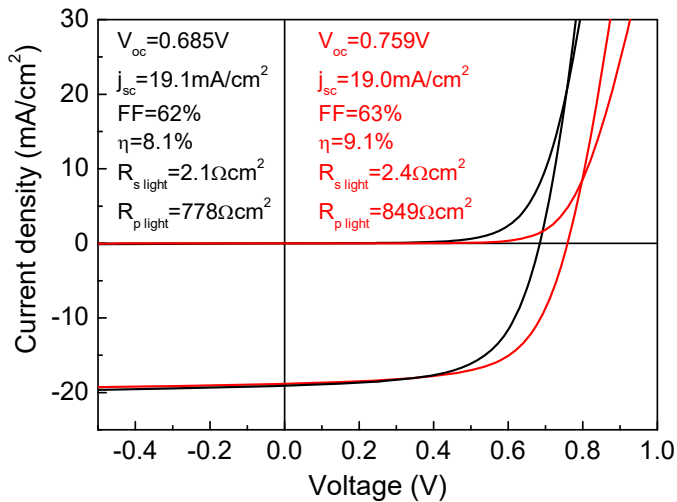


Figure 3.13 Current density-voltage curves before (black) and after (red) annealing powders at 150 °C for 4 h.

We can conclude that the highest degree of ordering in CZTS was achieved by annealing materials at temperatures between 150-175 °C. LT-annealing at 150 °C and 175 °C for 4 h increased the values of V_{oc} from 548 mV (CZTS-II) up to 714 mV and 718 mV, respectively. Annealing at temperatures higher than 175 °C (for example, at 200 °C) improves the values of V_{oc} to the level, which corresponds to the maximum possible value of the ordering degree at this temperature, and is constant thereafter. LT-annealing at temperatures lower than

150 °C will take longer time to reach the same level of V_{oc} , for example, the annealing at 125 °C for 5 days is equal to the annealing at 175 °C for 4 h.

Considering all solar cell output parameters, the optimal conditions for LT-annealing to improve monograin layer solar cells performance was found to be 4 h at 150 °C, although the highest V_{oc} value of 784 mV was gained by annealing the CZTS-I powder at 150 °C for 24 h (presented in Figure 3.11 by stars).

The optimal LT-annealing conditions were also applied to the CZTS-I powder, the corresponding J - V curve based on that powder is shown in Figure 3.13. The LT-annealing increased V_{oc} value by 74 mV, giving more than 10% higher efficiency ($\eta_{active} = 9.1\%$) compared to the reference cell ($\eta_{active} = 8.1\%$).

The EQE of these solar cells was measured as a function of the wavelength of the incident light at room temperature (see Figure 3.14). From the linear segment of the low-energy side of the construction $(E^*QE)^2$ vs. E curves, the effective bandgap energy E_g^* can be evaluated [89].

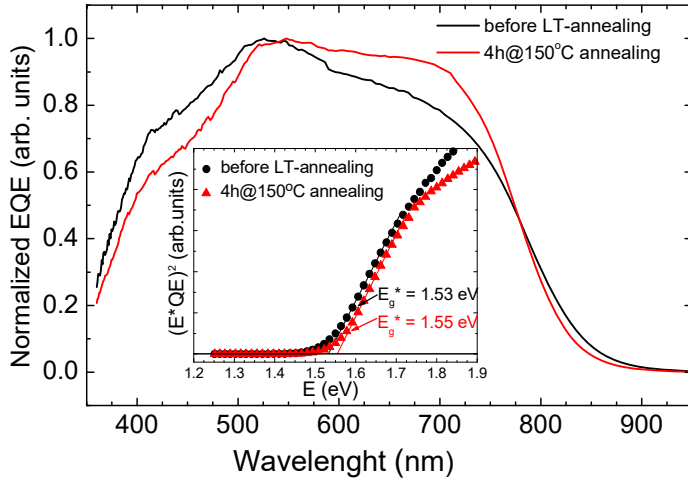


Figure 3.14 EQE spectra of MGL solar cell devices based on powders with different cooling regimes: before LT-annealing (black) and after annealing powder at 150 °C for 4 h (red). The inset graph shows the E_g^* determined from EQE data.

The E_g^* values of CZTS monograin powders before and after annealing at 150 °C for 4 h are 1.53 eV and 1.55 eV, respectively (see inset graph in Figure 3.14). It shows a small increase in the bandgap by improved ordering. This is in correspondence with the shift in band to band peak position in RT-PL spectra in Figure 3.10 (1.47 eV and 1.53 eV, respectively); however, the shift in the E_g^* value is smaller. This could be explained by the fact that E_g^* is connected to the change in the absorption, but RT-PL band position is determined by the recombination of the photogenerated charge carriers.

Summary of the disordering studies in $\text{Cu}_2\text{ZnSnS}_4$ monograin powders

Focus was on the influence of Cu-Zn ordering level in $\text{Cu}_2\text{ZnSnS}_4$ monograin powders on the performance of CZTS based MGL solar cells. The ordering level was changed by different cooling and LT-annealing regimes and estimated by PL and Raman spectroscopy. It was shown that improved ordering increases the bandgap energy of the CZTS materials, resulting in an increased value of V_{oc} of the corresponding MGL solar cells. The optimal conditions for LT-annealing to improve monograin layer solar cells performance were found to be 4 h at 150°C after cooling from 740°C to RT for 5 min, resulting in CZTS MGL solar cell efficiency of 9.1% (active area). The highest V_{oc} value 784 mV was obtained by annealing the powder at 150°C for 24 h.

It was found that change in the Cu-Zn ordering is accompanied with a change in the radiative recombination mechanism from band to tail to deep trap related recombination in the most ordered material, reducing the positive effect to the CZTS solar cell performance. In addition, the compositional changes in the near surface layer induced by very slow cooling after sulphur treatment could modify the interface properties of CZTS/CdS that can be responsible for the decrease in the solar cell parameters, including V_{oc} . The studies of junction formation between the ordered CZTS and the buffer layer are a subject for further studies.

3.3 Modification of the optoelectronic properties of $\text{Cu}_2\text{CdSnS}_4$ through low-temperature annealing

3.3.1 Results of structural and compositional analysis

The elemental composition of synthesized $\text{Cu}_2\text{CdSnS}_4$ polycrystalline powder was determined from the polished cross-section of individual crystals. Figure 3.15 presents SEM micrographs of (a) the polished cross-section and (b) the elemental mapping of Cu, Cd, Sn and S of individual $\text{Cu}_2\text{CdSnS}_4$ crystals. Figure 3.15(b) reveals that the elements are homogeneously distributed in the bulk of the powder crystals.

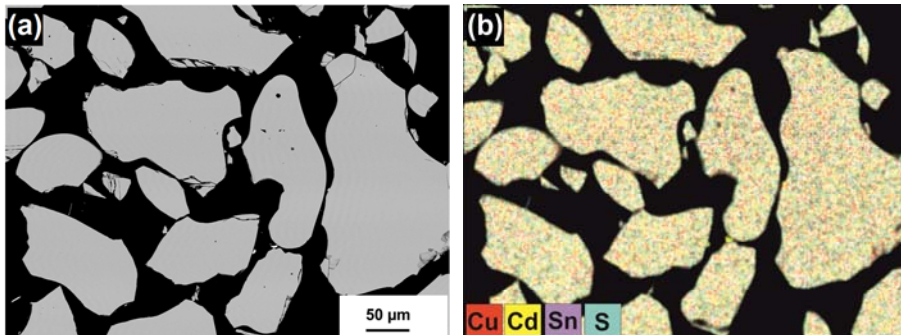


Figure 3.15 SEM images of (a) the polished cross-section and (b) elemental mapping by EDX for Cu, Cd, Sn and S of individual $\text{Cu}_2\text{CdSnS}_4$ crystals.

The average bulk composition of synthesized $\text{Cu}_2\text{CdSnS}_4$ polycrystalline powder determined by EDX analysis is $[\text{Cu}] = 24.5 \text{ at\%}$, $[\text{Cd}] = 13.0 \text{ at\%}$, $[\text{Sn}] = 12.5 \text{ at\%}$ and $[\text{S}] = 50.0 \text{ at\%}$. After different low-temperature annealing experiments, the composition of the powder remained unchanged.

Our experiments showed that the stable PL band position was reached by annealing at least 1 week at the temperature below $200 \text{ }^\circ\text{C}$; annealing at higher temperatures ($T_{\text{ann}} > 200 \text{ }^\circ\text{C}$) needed less time to reach stability. To be sure that the degree of ordering at a given temperature is reached, all powders used for the structural and optical studies were annealed for 1 week.

For structural studies, XRD and Raman analysis were performed. The XRD patterns of the $\text{Cu}_2\text{CdSnS}_4$ polycrystalline powders annealed at $T_{\text{ann}} = 100 \text{ }^\circ\text{C}$ and $T_{\text{ann}} = 400 \text{ }^\circ\text{C}$ are presented in Figure 3.16.

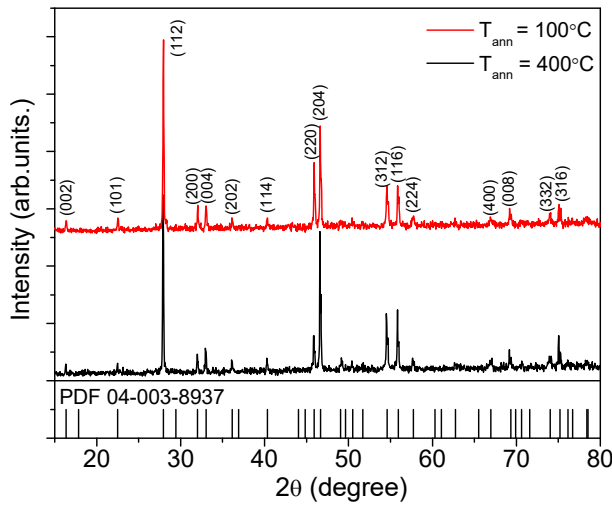


Figure 3.16 XRD patterns of the $\text{Cu}_2\text{CdSnS}_4$ polycrystals annealed at 100 and $400 \text{ }^\circ\text{C}$ for 1 week.

The major diffraction peaks can be attributed to (112), (200), (004), (220), (204), (312) and (116) planes of stannite type $\text{Cu}_2\text{CdSnS}_4$ with the space group $\bar{I}4_2m$ (ICDD PDF 04-003-8937). The a - and c - lattice constants were calculated from the XRD data and are $a = 5.592 \text{ \AA}$ and $c = 10.857 \text{ \AA}$ for both samples. All annealed $\text{Cu}_2\text{CdSnS}_4$ polycrystalline powders showed a similar XRD pattern and no other phases were detected.

Raman spectra of the $\text{Cu}_2\text{CdSnS}_4$ polycrystalline powder annealed at $T_{\text{ann}} = 100 \text{ }^\circ\text{C}$ and $T_{\text{ann}} = 400 \text{ }^\circ\text{C}$ are presented in Figure 3.17. The spectra of $\text{Cu}_2\text{CdSnS}_4$ annealed at different temperatures are all similar except for the widths of the peaks and for clarity, only the spectra for the material annealed at the lowest ($T_{\text{ann}} = 100 \text{ }^\circ\text{C}$) and at the highest temperature ($T_{\text{ann}} = 400 \text{ }^\circ\text{C}$) used in this study are presented. The observed Raman spectra are in agreement with our studies in Papers I and IV and with published data [94] and the two Raman active A_1 symmetry modes characteristic for the stannite type structured $\text{Cu}_2\text{CdSnS}_4$ can be found at 332 cm^{-1} and 283 cm^{-1} . These modes result from the

motions of anions only. Other symmetry Raman modes (E and B₂ modes) were detected at 89 cm⁻¹, 138 cm⁻¹, 237 cm⁻¹, 268 cm⁻¹, 343 cm⁻¹, 352 cm⁻¹, and 364 cm⁻¹.

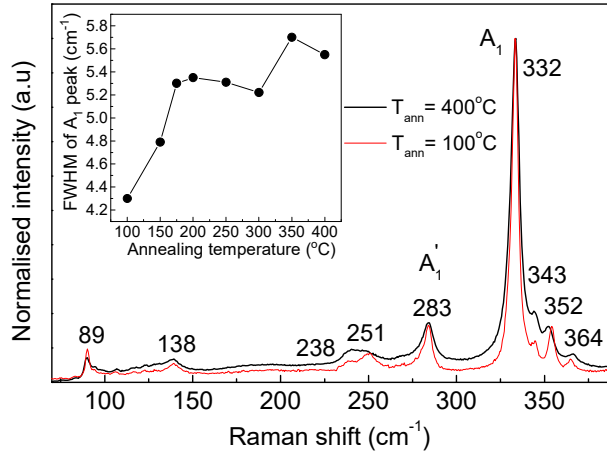


Figure 3.17 Raman spectra of Cu₂CdSnS₄ annealed at temperatures 100 and 400 °C for 1 week. The inset graph shows the dependence of the FWHM of the A₁ Raman mode at 332 cm⁻¹ on the annealing temperature.

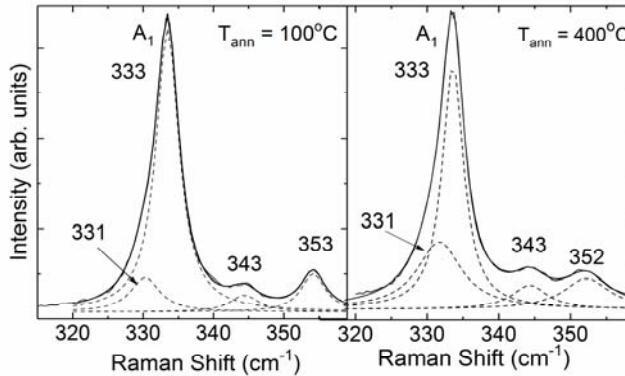


Figure 3.18 Fitting of the A₁ Raman peak of Cu₂CdSnS₄ annealed at 100 and 400 °C for 1 week, with two Lorentzian peaks. The shoulder peak at the low wavenumber side at 331 cm⁻¹ can be attributed to the disordered Cu₂CdSnS₄.

No significant difference in the Raman peak positions of Cu₂CdSnS₄ polycrystalline powder annealed at different temperatures could be detected. From the inset graph in Figure 3.17, a clear tendency towards an increasing full width at the half maximum (FWHM) of the dominating A₁ mode with increasing annealing temperature can be seen. It has been shown that in kesterite Cu₂ZnSnS₄ and Cu₂ZnSnSe₄, the low-temperature annealing at different temperatures below and above the critical temperature leads to the changes in the degree of Cu-Zn ordering and in the width and symmetry of the A₁ Raman peak [53, 53, 61, 62]. Broadening of the A₁ Raman peak with

increasing annealing temperature was observed, attributed to the higher degree of disordering. It was found that the asymmetry of the A_1 peak is caused by a shoulder peak at low wavenumber side that was attributed to the A_1 mode of the disordered $\text{Cu}_2\text{ZnSnS}_4$. The same trend as was seen in $\text{Cu}_2\text{ZnSnS}_4$ is observed in the present study for $\text{Cu}_2\text{CdSnS}_4$, indicating a higher level of disordering with an increasing annealing temperature. An example of the fitting of the A_1 Raman peak of $\text{Cu}_2\text{CdSnS}_4$ annealed at $T_{\text{ann}} = 100$ °C and $T_{\text{ann}} = 400$ °C with two Lorentzian peaks is shown in Figure 3.18. The shoulder peak at the low wavenumber side at 331 cm^{-1} can be attributed to the disordered $\text{Cu}_2\text{CdSnS}_4$ and its relative intensity decreases with the annealing temperature decreasing.

3.3.2 Photoluminescence analysis results

To determine the influence of low-temperature annealing on the defect structure of $\text{Cu}_2\text{CdSnS}_4$, temperature dependent PL measurements were performed. Low temperature ($T = 10\text{ K}$) PL spectra of all studied $\text{Cu}_2\text{CdSnS}_4$ polycrystalline powders annealed at different temperatures consisted of one broad asymmetric PL band, see Figure 3.19. We observed a shift in the PL band position towards lower energies with increasing annealing temperature. The highest energy PL band is situated at 1.215 eV , corresponding to the $\text{Cu}_2\text{CdSnS}_4$ polycrystalline powder annealed at 100 °C for 1 week (sample will be named as “ordered” based on the Raman results). The lowest energy PL band was detected at 1.064 eV , corresponding to the $\text{Cu}_2\text{CdSnS}_4$ polycrystalline powder annealed at 400 °C for 1 week (sample will be named as “disordered”).

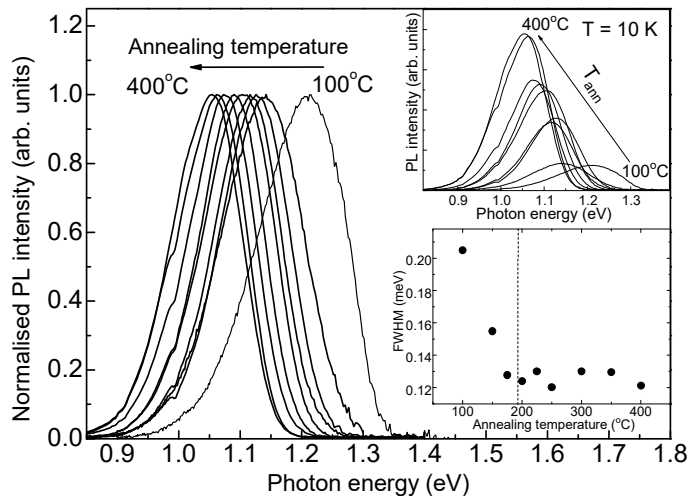


Figure 3.19 Normalized low-temperature ($T = 10\text{ K}$) PL spectra of $\text{Cu}_2\text{CdSnS}_4$ polycrystalline powders annealed at different temperatures in the range from 100 to 400 °C for 1 week. A shift of the PL band towards lower energies with increasing annealing temperature can be seen. The upper inset graph presents the original PL spectra showing the decrease in the PL intensity with decreasing annealing temperature. In the lower inset graph, the dependence of the FWHM of the PL band on the annealing temperature is shown.

The overall difference in the PL band positions of the ordered and disordered $\text{Cu}_2\text{CdSnS}_4$ is about 150 meV. As can be seen from the upper inset graph in Figure 3.19, the intensity of the PL signal decreases with the decrease in the annealing temperature. In addition, narrowing of the PL band was observed for higher annealing temperatures, the full width at the half maximum (FWHM) being largest for the lowest annealing temperature ($T_{ann} = 100$ °C), see lower inset graph in Figure 3.19. Two regions were observed in the dependence of the FWHM on the annealing temperature: above $T_{ann} = 200$ °C, the FWHM is almost constant ranging from 0.12 to 0.13 meV and below $T_{ann} = 200$ °C, the FWHM increased up to 0.16 meV with decreasing annealing temperature. It is also important to notice that the PL bands are located more than 0.2 eV below the bandgap energy of $\text{Cu}_2\text{CdSnS}_4$ that is reported to be 1.4 eV at room temperature [Paper IV, 94] and is even higher at low temperature ($T = 10$ K).

Table 3.4 Parameters describing the low temperature PL bands of the $\text{Cu}_2\text{CdSnS}_4$ polycrystalline powders annealed at different temperatures: γ – average depth of the spatial potential fluctuations, $h\nu_{max}$ – PL band peak position, E_T - thermal activation energy and FWHM – full width at the half maximum of the PL band. For two samples (175 and 300 °C, temperature dependencies were not measured).

Annealing temperature (°C)	γ (meV)	$h\nu_{max\#1}$ (eV)	$E_{T\#1}$ (meV)	FWHM (#1) (eV)	$h\nu_{max\#2}$ (eV)	$E_{T\#2}$ (meV)	FWHM (#2) (eV)
100	23	1.165	110 ± 4	0.13	1.245	60 ± 5	0.10
150	22	1.123	105 ± 6	0.13	1.189	62 ± 7	0.11
175	24	1.112	-	0.12	1.161	-	0.11
200	25	1.116	86 ± 8	0.12			
225	24	1.106	146 ± 7	0.13			
250	25	1.093	135 ± 7	0.12			
300	26	1.079	-	0.13			
350	27	1.065	151 ± 7	0.13			
400	27	1.064	133 ± 5	0.12			

To determine the recombination mechanisms behind the PL bands, temperature dependent PL measurements were performed. Due to the asymmetric shape of the PL bands, all the spectra were fitted with empirical asymmetric double sigmoid function [95] that describes well such broad and asymmetric PL bands with exponential tail in the low-energy side that are very common in multinary compound semiconductors with spatial potential fluctuations. The spatial potential fluctuations result from high concentration of randomly distributed charged native defects [59, 95, 96]. The asymmetric shape results from the band tails of the density of states function extending into the bandgap. The average depth of the fluctuations γ can be determined from the slope of the low energy side of the PL band [95-97]. The corresponding γ values of the PL bands of the $\text{Cu}_2\text{CdSnS}_4$ polycrystalline powders annealed at different temperatures can be found in Table 3.4. It was found that the average depth of the fluctuations is very similar in all samples, indicating similar large defect concentrations.

From the temperature dependencies of the PL spectra, the temperature dependence of the PL band maxima and integrated intensity were analyzed. It

was found that the PL bands measured from the $\text{Cu}_2\text{CdSnS}_4$ polycrystalline powders annealed at temperatures below $T_{\text{ann}} = 200$ °C are composed of two PL bands that are labeled #1 and #2 (an example of the fitting of the spectra is presented in Figure 3.20). The presence of two PL bands also explains the widening of the PL spectrum with decreasing annealing temperature. From the Arrhenius plots, the thermal activation energies of the quenching of the PL bands were determined by using the theoretical expression for discrete energy levels for fitting [98]:

$$\Phi(T) = \frac{\Phi_0}{1 + \alpha_1 T^{3/2} + \alpha_2 T^{3/2} \exp(-\frac{E_T}{kT})} \quad (1)$$

where Φ is integrated intensity, α_1 and α_2 are the process rate parameters and E_T is the thermal activation energy. The obtained values of the thermal activation energies E_T , as dependent on the annealing temperature, are listed in Table 3.4 together with the positions of the PL band maxima and FWHM. Two annealing temperature regions can be observed: two PL bands were detected in $\text{Cu}_2\text{CdSnS}_4$ annealed at temperatures below $T_{\text{ann}} = 200$ °C, showing thermal activation energies of around 60 meV and 110 meV, and one PL band was observed in $\text{Cu}_2\text{CdSnS}_4$ annealed at temperatures above $T_{\text{ann}} = 200$ °C having high thermal activation energy above 130 meV.

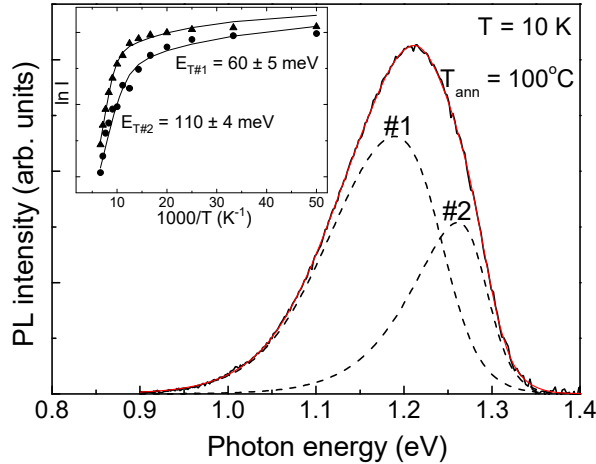


Figure 3.20 Low-temperature ($T = 10$ K) PL spectrum of $\text{Cu}_2\text{CdSnS}_4$ polycrystalline powder annealed at 100 °C for 1 week together with the fitting result. The inset graph presents the Arrhenius plots for the two PL bands used to determine the thermal quenching activation energies for #1 and #2.

It has been shown that in the disordered $\text{Cu}_2\text{ZnSnS}_4$ recombination mechanism that involves defect clusters inducing local bandgap energy, shrinkage is dominating [62]. The latter results in large bandgap fluctuations that create efficient recombination paths for photogenerated carriers in the material. In the ordered $\text{Cu}_2\text{ZnSnS}_4$, recombination involving deep acceptor defects (> 200 meV) is prevailing at low temperatures [62]. Similarly, high

concentration of $[\text{Cu}_{\text{Cd}} + \text{Cd}_{\text{Cu}}]$ and $[2\text{Cu}_{\text{Cd}} + \text{Sn}_{\text{Cd}}]$ defect complexes is predicted in $\text{Cu}_2\text{CdSnS}_4$ [43], being responsible for the Cu-Cd disordering. According to the theoretical calculations, the difference in the bandgap energies of disordered and ordered $\text{Cu}_2\text{CdSnS}_4$ is about 100 meV [42]. Therefore, recombination mechanism involving defect clusters is also expected in this material.

Considering that the bandgap energy of $\text{Cu}_2\text{CdSnS}_4$ at low temperatures is close to 1.5 eV, the PL bands are very far from the band edge, separation of the PL band from the bandgap is over 300 meV and over 200 meV for #1 and #2, respectively. Different thermal activation energies of the PL band quenching were found for #1 (above 100 meV) and #2 (below 100 meV), indicating a different recombination channel. Considering the thermal activation energies and the PL band positions with respect to the low temperature bandgap energy of $\text{Cu}_2\text{CdSnS}_4$, one can see that in both ordered and disordered $\text{Cu}_2\text{CdSnS}_4$, the dominating radiative recombination is related to the defect clusters inducing bandgap energy shrinkage that was also seen in disordered $\text{Cu}_2\text{ZnSnS}_4$ [93]. However, the dominating defect clusters are different in the ordered and disordered $\text{Cu}_2\text{CdSnS}_4$. We propose that in the disordered $\text{Cu}_2\text{CdSnS}_4$, the $[2\text{Cu}_{\text{Cd}} + \text{Sn}_{\text{Cd}}]$ defect complexes inducing large bandgap energy fluctuations (with depth > 0.4 eV [42]) dominate. In the ordered material, the coexistence of $[2\text{Cu}_{\text{Cd}} + \text{Sn}_{\text{Cd}}]$ and $[\text{Cu}_{\text{Cd}} + \text{Cd}_{\text{Cu}}]$ defect complexes is present, resulting in the two observed PL bands #1 and #2. However, based on the PL intensity analysis (see upper inset graph in Figure 3.19), the overall concentration of the mentioned defect complexes is reduced in the ordered material.

RT-PL measurements were also performed to the $\text{Cu}_2\text{CdSnS}_4$ polycrystalline powders annealed at different temperatures. Similar to low-temperature PL (10 K) results, a shift of the PL band towards lower energies with increasing annealing temperature was observed, the positions of the PL bands being 1.45 eV and 1.37 eV for samples annealed at 100 and 400 °C, respectively. For clearance, only the spectra of the ordered and disordered $\text{Cu}_2\text{CdSnS}_4$ (e.g. annealing temperatures 100 and 400 °C) are presented in Figure 3.21. Broader PL band was observed for the disordered material, most probably caused by larger bandgap fluctuations. Considering the room temperature bandgap energy of $\text{Cu}_2\text{CdSnS}_4$ around 1.4 eV [28, Paper IV], the observed PL bands result from the band-to-band recombination. Notice that it is not the same PL band that was observed at low temperature (10 K).

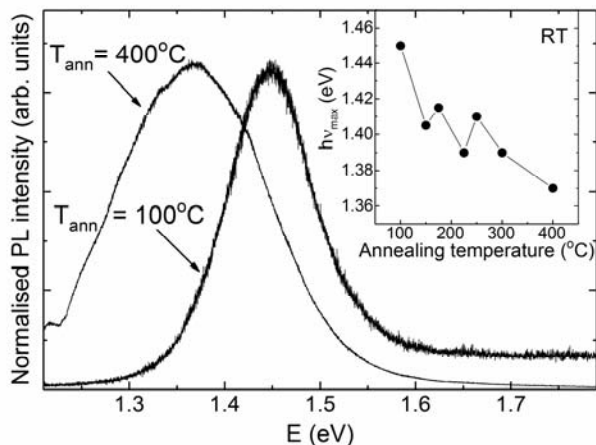


Figure 3.21 RT-PL spectra of $\text{Cu}_2\text{CdSnS}_4$ annealed at temperatures 100 and 400 °C for 1 week. The shift of the position of the PL band maximum towards lower energies with increasing annealing temperature was detected.

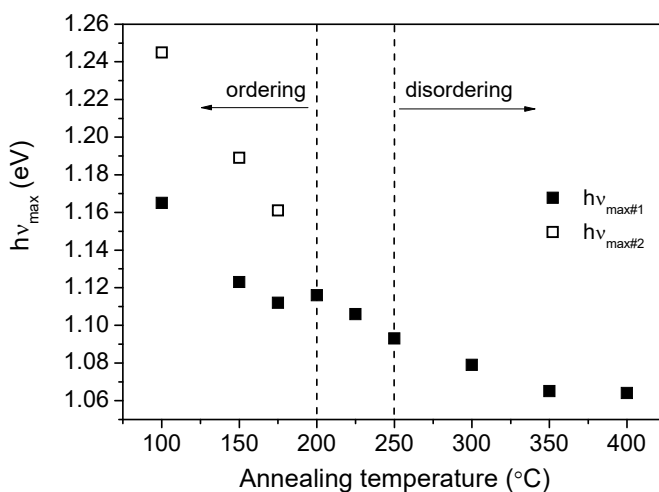


Figure 3.22 PL band positions of $\text{Cu}_2\text{CdSnS}_4$ polycrystalline powders depending on the low-temperature annealing in the range from 100 to 400 °C for 1 week.

Finally, Figure 3.22 shows the low-temperature PL band position of $\text{Cu}_2\text{CdSnS}_4$ depending on the annealing temperature in the range from 100 to 400 °C for 1 week. The vertical dashed lines in Figure 3.22 indicate the annealing temperature region where the PL band position is almost constant and no change in the recombination mechanism has taken place. Almost constant FWHM of the A_1 Raman mode was observed in the same annealing temperature region from 200 to 250 °C. We can conclude that it is possible to modify the degree of disordering with the low-temperature annealing treatments below the critical temperature that according to our study, lies in the temperature range from 200 to 250 °C.

Summary of ordering-disordering studies in $\text{Cu}_2\text{CdSnS}_4$ polycrystalline powders

From the Raman scattering and temperature dependent PL analysis of the $\text{Cu}_2\text{CdSnS}_4$ polycrystalline powder, we can conclude that the Cu-Cd disordering predicted by the theoretical first principles calculations [42] is present in this material. We have shown in this study that the degree of disordering can be reduced with the low-temperature annealing treatments below the critical temperature that according to our study, lies in the temperature range from 200 to 250 °C. It was found that similar to $\text{Cu}_2\text{ZnSnS}_4$, the change in the degree of disordering in $\text{Cu}_2\text{CdSnS}_4$ is accompanied with the change in the radiative recombination channel related to different types of defect clusters.

Finally, based on $\text{Cu}_2\text{ZnSnS}_4$ and $\text{Cu}_2\text{CdSnS}_4$ disordering studies, it can be concluded that $\text{Cu}_2\text{Zn}_{1-x}\text{Cd}_x\text{SnS}_4$ solid solutions reported in Paper I were disordered materials.

CONCLUSIONS

The investigations in this dissertation are divided to three main parts. The first part presents the systematic investigations of $\text{Cu}_2(\text{Zn}_{1-x}\text{Cd}_x)\text{SnS}_4$ ($x = 0-1$) solid solutions of monograin powders synthesized in KI molten salt. The compositional, structural and optoelectronic properties of these powders were studied to find the optimal Cd content in solid solutions for an ideal bandgap of $\text{Cu}_2(\text{Zn}_{1-x}\text{Cd}_x)\text{SnS}_4$ -based single junction solar cells. In the second part of the thesis, focus is on the influence of ordering-disordering in kesterite-type $\text{Cu}_2\text{ZnSnS}_4$ monograin powders on the compositional, structural and optoelectronic properties of these powders and on the performance of $\text{Cu}_2\text{ZnSnS}_4$ based monograin layer solar cells. The final part of the thesis explains the existence of disordering in stannite-type $\text{Cu}_2\text{CdSnS}_4$ and the influence of this phenomenon on the optoelectronic properties. Based on the studies, the following conclusions can be made:

- The entire range of $\text{Cu}_2(\text{Zn}_{1-x}\text{Cd}_x)\text{SnS}_4$ ($x = 0 - 1$) solid solutions of monograin powders in KI flux with the controllable Cd concentration were synthesized.

Structural studies showed that Cd incorporation to the $\text{Cu}_2\text{ZnSnS}_4$ lattice increases the a -axis lattice constant almost linearly from 5.433 to 5.593 Å as the Cd content increases from 0 to 1. XRD and Raman suggested that $\text{Cu}_2(\text{Zn}_{1-x}\text{Cd}_x)\text{SnS}_4$ solid solutions have kesterite-type structure in the region $0 \leq x \leq 0.3$ and they exist in the stannite-type structure in the region $0.4 \leq x \leq 1$.

The effective bandgap energy values (E_g^*) calculated from EQE measurements for $\text{Cu}_2(\text{Zn}_{1-x}\text{Cd}_x)\text{SnS}_4$ solid solutions changed from 1.55 eV to 1.37 eV. The optimal bandgap of 1.4 eV for $\text{Cu}_2(\text{Zn}_{1-x}\text{Cd}_x)\text{SnS}_4$ solid solution with the $x = 0.4$ was determined and was proposed to be a suitable material for an absorber layer in single junction solar cells.

- The degree of Cu-Zn disordering in $\text{Cu}_2\text{ZnSnS}_4$ monograin powders was feasible by using different cooling regimes after high-temperature treatment and by additional annealing at temperatures below critical temperature.

PL studies showed that slower cooling of $\text{Cu}_2\text{ZnSnS}_4$ monograin powders after HT-treatment shifted the typical broad asymmetric PL band position from 1.21 eV to 1.35 eV. The additional low-temperature annealing after different cooling processes shifted the corresponding PL band positions even to a higher energy side, giving hint to a further increase in the ordering degree. The behavior of the PL bands with increased Cu-Zn ordering is caused by two processes – improved Cu-Zn ordering of the crystals leading to increased bandgap energy and change in the radiative recombination

mechanism from band to tail to deep trap related recombination in most ordered material.

Optimal conditions for LT-annealing to improve $\text{Cu}_2\text{ZnSnS}_4$ MGL solar cells performance were found to be 4 h at 150 °C. These improvements resulted in $\text{Cu}_2\text{ZnSnS}_4$ MGL solar cell power conversion efficiency of 9.1%. The highest open circuit voltage 784 mV for $\text{Cu}_2\text{ZnSnS}_4$ based solar cells was obtained in lab conditions.

- For the first time, experimental evidence of the existence of Cu-Cd disordering in the stannite-type $\text{Cu}_2\text{CdSnS}_4$ material is presented and the critical temperature range of order-disorder transition for $\text{Cu}_2\text{CdSnS}_4$ is proposed. According to Raman and PL results, the critical temperature lies in the range from 200 to 250 °C.

Low temperature ($T = 10$ K) PL spectra of polycrystalline powders consist of one broad asymmetric PL band at 1.064 eV for the most disordered $\text{Cu}_2\text{CdSnS}_4$ and at 1.215 eV for the most ordered $\text{Cu}_2\text{CdSnS}_4$. It was also found that similar to $\text{Cu}_2\text{ZnSnS}_4$, the change in the degree of disordering in $\text{Cu}_2\text{CdSnS}_4$ is accompanied with the change in the radiative recombination channel related to different types of defect clusters. We propose that in the disordered $\text{Cu}_2\text{CdSnS}_4$, the $[\text{2Cu}_{\text{Cd}} + \text{Sn}_{\text{Cd}}]$ defect complexes dominate and in the ordered material, the coexistence of $[\text{2Cu}_{\text{Cd}} + \text{Sn}_{\text{Cd}}]$ and $[\text{Cu}_{\text{Cd}} + \text{Cd}_{\text{Cu}}]$ defect complexes is present.

ACKNOWLEDGEMENTS

This thesis is based on the experimental work carried out in the Laboratory of Photovoltaic Materials, Tallinn University of Technology.

Above all, I would like to express my sincerest gratitude to my supervisor Dr. Marit Kauk-Kuusik for her support and excellent guidance, understanding and encouragement over the years of my studies. I would not have been able to complete my dissertation without her assistance.

My special thanks go to Dr. Maarja Grossberg for her support and helpful discussions about Raman and photoluminescence studies and to Dr. Kristi Timmo helping me with the experiments, and being a great friend. I am truly thankful to all my colleagues in the laboratory for helping me with the experiments, measurements and guidance especially Dr. Tiit Varema, Dr. Jaan Raudoja, Dr. Mare Altosaar, Dr. Jüri Krustok, Dr. Taavi Raadik, Dr. Mati Danilson, Dr. Valdek Mikli, Dr. Arvo Mere and Dr. Rainer Traksmaa.

I would also like to thank Prof. Enn Mellikov for giving me the opportunity to join and work in the research group at the Chair of Materials Science.

I wish to thank Dr. Malle Krunks, Head of Department of Materials and Environmental Technology and Prof. Andres Öpik, the Director of the doctoral school “Functional materials and technologies” in Tallinn University of Technology for providing the opportunity to participate in the PhD studies of the faculty and in the graduate school.

I appreciate greatly Prof. Charlotte Platzer Björkman, University of Uppsala, Sweden and Dr. Vambola Kisand, University of Tartu, Estonia for the acceptance to be opponents of this thesis.

The work was financially supported by the Estonian Ministry of Education and Research under Projects SF0140099s08 (New materials and technologies for solar energetics), IUT19-28 (New materials and technologies for solar energetics), and by the Estonian Science Foundation grants G7678, G8964, G9346, and G9425, by the European Regional Development Funds Projects TK117 (Centre of Excellence: High-technology Materials for Sustainable Development), TK141 (Advanced materials and high-technology devices for sustainable energetics, sensorics and nanoelectronics), and AR10128 (New materials for solar energetics), by the FP7 Project CHEETAH Grant Agreement No. 609788, and by ERASMUS+ Project VER 674. I would also like to thank spin-off company crystalsol OÜ for pleasant collaboration through the Project Lep12065.

My warmest gratitude belongs to my family, to my daughters Miriam and Merili.

Tallinn, 2017
Maris Pilvet

ABSTRACT

$\text{Cu}_2\text{ZnSnS}_4$ quaternary compound has attracted much attention in the last years as a new abundant, low cost and non-toxic material with desirable properties for photovoltaic applications.

In this work, $\text{Cu}_2(\text{Zn}_{1-x}\text{Cd}_x)\text{SnS}_4$ monograin powders were grown using monograin powder growth technology and polycrystalline powder of $\text{Cu}_2\text{CdSnS}_4$ was synthesized by solid-state reaction. The structural properties of synthesised materials were characterized by Raman and X-ray diffraction (XRD), composition was analyzed by energy dispersive X-ray spectroscopy and photoluminescence (PL) was used to the investigated recombination processes in the materials. All monograin powders were used as absorber layers in monograin layer solar cells with the structure: graphite/ $\text{Cu}_2(\text{Zn}_{1-x}\text{Cd}_x)\text{SnS}_4$ /CdS/i-ZnO/ZnO:Al/Ag.

Focus was on the influence of Zn substitution by Cd atoms on the compositional, structural and optoelectronic properties of $\text{Cu}_2\text{ZnSnS}_4$ monograin powders. The aim was to find the optimal Cd content in $\text{Cu}_2(\text{Zn}_{1-x}\text{Cd}_x)\text{SnS}_4$ solid solutions that gives the ideal bandgap of absorber material for single junction solar cells. The entire range of $\text{Cu}_2(\text{Zn}_{1-x}\text{Cd}_x)\text{SnS}_4$ ($x = 0 - 1$) solid solutions of monograin powders in KI flux with the controllable Cd concentration were synthesized. Results of the study showed that Cd incorporation to the $\text{Cu}_2\text{ZnSnS}_4$ lattice increases the a -axis lattice constant almost linearly from 5.433 to 5.593 Å as the Cd content increases from 0 to 1. The expansion of lattice constant can be attributed to the larger ion radius of Cd than that of Zn or Cu. Structural studies by XRD and Raman suggested that $\text{Cu}_2(\text{Zn}_{1-x}\text{Cd}_x)\text{SnS}_4$ solid solutions have kesterite-type structure in the region $0 \leq x \leq 0.3$ and they exist in stannite-type structure in the region $0.4 \leq x \leq 1$. Corresponding effective bandgap energy values (E_g^*) for solid solutions were calculated from EQE measurements. Results showed the correlation between the Cd content ($x = 0 - 1$) in the $\text{Cu}_2(\text{Zn}_{1-x}\text{Cd}_x)\text{SnS}_4$ absorber material and the values of E_g^* that changed from 1.55 to 1.37 eV, respectively. It was concluded that $\text{Cu}_2(\text{Zn}_{1-x}\text{Cd}_x)\text{SnS}_4$ solid solution with the $x = 0.4$ has optimal bandgap of 1.4 eV and is a suitable material for an absorber layer in single junction solar cells.

The main limitation of the power conversion efficiency in $\text{Cu}_2\text{ZnSnS}_4$ based solar cells is low open circuit voltage (V_{oc}) as compared to the bandgap energy values. The existence of Cu and Zn cation disorder in $\text{Cu}_2\text{ZnSnS}_4$ kesterite crystal structure could be one reason for the large V_{oc} deficit limiting the efficiency of the solar cell device. The second part of the investigations was dedicated to the systematic study of the influence of ordering-disordering in $\text{Cu}_2\text{ZnSnS}_4$ monograin powders on the compositional, structural and optoelectronic properties of these powders and on the performance of $\text{Cu}_2\text{ZnSnS}_4$ based monograin layer solar cells.

The degree of Cu-Zn disordering was changed by using different cooling regimes after high-temperature (HT) treatment and by additional annealing at temperatures below critical temperature ($T_c \sim 260$ °C).

Low-temperature ($T=10$ K) and RT-PL measurements were used to estimate the Cu-Zn disorder level in $\text{Cu}_2\text{ZnSnS}_4$ monograin powders. PL studies showed that slower cooling of $\text{Cu}_2\text{ZnSnS}_4$ monograin powders after HT-treatment shifted the typical broad asymmetric PL band position from 1.21 to 1.35 eV. The additional low-temperature (LT) annealing after different cooling processes shifted the corresponding PL band positions even to a higher energy side, giving hint to the further increase in the ordering degree. The behavior of the PL bands with increased Cu-Zn ordering is caused by two processes – improved Cu-Zn ordering of the crystals leading to increased band gap energy and change in the radiative recombination mechanism from band to tail to deep trap related recombination in most ordered materials.

Current-voltage measurements of MGL solar cells revealed that increased ordering in the $\text{Cu}_2\text{ZnSnS}_4$ absorber material had significant impact on the characteristics, mainly the values of V_{oc} were increased. Optimal conditions for LT-annealing to improve the performance of $\text{Cu}_2\text{ZnSnS}_4$ MGL solar cells were found to be 4 h at 150 °C. These improvements resulted in the $\text{Cu}_2\text{ZnSnS}_4$ MGL solar cell power conversion efficiency of 9.1%. The highest open circuit voltage 784 mV for $\text{Cu}_2\text{ZnSnS}_4$ based solar cells was obtained in lab conditions.

The last part of the investigations in this thesis presents for the first time experimental evidence of the existence of Cu-Cd disordering in stannite-type $\text{Cu}_2\text{CdSnS}_4$ material and proposes the critical temperature range of order-disorder transition for $\text{Cu}_2\text{CdSnS}_4$. The degree of Cu-Cd disordering in $\text{Cu}_2\text{CdSnS}_4$ polycrystalline powder was changed by LT-annealing at temperatures from 100 to 400 °C.

Low temperature ($T=10$ K) PL spectra of all studied $\text{Cu}_2\text{CdSnS}_4$ polycrystalline powders consist of one broad asymmetric PL band. The lowest energy PL band was detected at 1.064 eV, corresponding to the most disordered $\text{Cu}_2\text{CdSnS}_4$ and PL band position for the most ordered $\text{Cu}_2\text{CdSnS}_4$ was situated at 1.215 eV. According to Raman and PL results, the critical temperature lies in the range from 200 to 250 °C. It was also found that similar to $\text{Cu}_2\text{ZnSnS}_4$, the change in the degree of disordering in $\text{Cu}_2\text{CdSnS}_4$ is accompanied with the change in the radiative recombination channel related to different types of defect clusters. We proposed that in the disordered $\text{Cu}_2\text{CdSnS}_4$, the $[2\text{Cu}_{\text{Cd}} + \text{Sn}_{\text{Cd}}]$ defect complexes dominate and in the ordered material, the coexistence of $[2\text{Cu}_{\text{Cd}} + \text{Sn}_{\text{Cd}}]$ and $[\text{Cu}_{\text{Cd}} + \text{Cd}_{\text{Cu}}]$ defect complexes is present. However, based on the PL intensity analysis, the overall concentration of the mentioned defect complexes is reduced in the ordered material.

KOKKUVÕTE

Viimasel aastakümnel on hüppeliselt kasvanud $\text{Cu}_2\text{ZnSnS}_4$ kui absorbermaterjali uuringud päikeseenergeetika rakendustes. Antud materjali koostiselemendid on keskkonnasõbralikud ja maapõues laialdaselt levinud. $\text{Cu}_2\text{ZnSnS}_4$ omab absorbermaterjalile sobivaid optilisi ja elektrilisi omadusi: otsene keelutsoon laiusega 1,55 eV, neeldumiskoeffitsent $> 10^4 \text{ cm}^{-1}$, p -tüüpi juhtivus.

Tänaseks on $\text{Cu}_2\text{ZnSnS}_4$ -baasil valmistatud päikeseplatereide suurimaks kasuteguriks mõõdetud 9,5%. Sellele tasemele on areng peatuma jäänud juba mitu viimast aastat. Schockley-Queisser teooria kohaselt on võimalik saavutada päikeseplaterei maksimaalne teoreetiline kasutegur absorbermaterjali keelutsooniga vahemikus 1,0 ja 1,5 eV. Seda arvestades tuleks $\text{Cu}_2\text{ZnSnS}_4$ absorbermaterjali keelutsooni laiust vähendada. Keelutsooni on võimalik vähendada ühendpooljuhtmaterjalides asendades samasse rühma kuuluva kergema elemendi aatomi raskema elemendi aatomiga, näiteks Zn asendamine Cd.

Käesolevas töös kasutati $\text{Cu}_2\text{ZnSnS}_4$ absorbermaterjali keelutsooni varieerimiseks monoterapulber-tehnoloogiat. Erineva Cd-sisaldusega $\text{Cu}_2(\text{Zn}_{1-x}\text{Cd}_x)\text{SnS}_4$ monoterapulbrid sünteesiti sünteeskasvatusel KI sulandaja keskkonnas. Kõikide sünteesitud monoterapulbrite elementkoostise ja morfoloogia iseloomustamiseks kasutati EDX ja SEM analüüsi, struktuuri kirjeldamiseks XRD ja Raman spektroskoopiat, rekombinatsiooni protsesside iseloomustamiseks PL mõõtmisi, efektiivse keelutsooni laiuse määramiseks EQE mõõtmisi.

Elementkoostise analüüsi tulemused näitasid, et monoterapulber-tehnoloogiaga on võimalik sünteesida $\text{Cu}_2(\text{Zn}_{1-x}\text{Cd}_x)\text{SnS}_4$ tahkeid lahuseid kogu koostise ulatuses $x = 0 - 1$. Struktuurianalüüsid näitasid, et suurem Cd sisaldus $\text{Cu}_2(\text{Zn}_{1-x}\text{Cd}_x)\text{SnS}_4$ tahke lahuse kristallvõres suurendab võrekonstanti a 5,433 Å-lt 5,593 Å-le. Võrekonstandi suurenemist võib omistada Cd suuremale ioonraadiusele võrreldes Zn või Cu-ga. XRD ja Raman analüüsid näitasid, et $\text{Cu}_2(\text{Zn}_{1-x}\text{Cd}_x)\text{SnS}_4$ tahked lahused on kesteriitse kristallstruktuuriga, kui Cd sisaldus $x < 0,3$ ning stanniitse kristallstruktuuriga, kui Cd sisaldus $x > 0,4$. Efektiivset keelutsooni laiust saab muuta 1,55 eV ($x = 0$) kuni 1,37 eV-ni ($x = 1$). Leiti, et optimaalse keelutsooni laiuse 1,4 eV saamiseks peab $\text{Cu}_2(\text{Zn}_{1-x}\text{Cd}_x)\text{SnS}_4$ monoterapulbrites Cd-sisaldus olema $\sim 0,4$.

On leitud, et $\text{Cu}_2\text{ZnSnS}_4$ -baasil valmistatud päikeseplatereide kasutegurit limiteerivaks parameetrik on avatud vooluahela pinge (V_{oc}) puudujääk võrreldes antud materjalile vastava keelutsooni väärtusega. Teoreetiliselt võiks 1,5 eV keelutsooniga absorbermaterjalist valmistatud päikeseplatereide V_{oc} väärtus olla $\sim 1\text{V}$. Üheks põhjuseks on Cu-Zn korrastamatuse esinemine $\text{Cu}_2\text{ZnSnS}_4$ kristallvõres, mis põhjustab keelutsooni vähenemist. Cu-Zn korrastatust kristallvõres on võimalik reguleerida jahtumiskiirusega peale kõrgtemperatuurset käsitlusi või madaltemperatuursete lõõmutustega alla kriitilist temperatuuri ($T_c = 260 \text{ }^\circ\text{C}$).

Käesolevas doktoritöös uuriti süstemaatiliselt Cu-Zn korrastatuse mõju $\text{Cu}_2\text{ZnSnS}_4$ monoterapulbrite elementkoostisele, struktuursetele ja optoelektronsetele omadustele ning nende materjalide baasil valmistatud monoterakiht-päikesepatareide väljundparameetritele.

Cu-Zn korrastatuse hindamiseks $\text{Cu}_2\text{ZnSnS}_4$ monoterapulbrites kasutati madaltemperatuurset ($T = 10$ K) kui ka toatemperatuurset fotoluminestsents-spektroskoopiat.

PL mõõtmised näitasid, et $\text{Cu}_2\text{ZnSnS}_4$ monoterapulbrite aeglasem jahtumine peale kõrgtemperatuurset käsitlust nihutas PL riba asukohta 1,2 eV-lt kuni 1,35 eV-ni. Madaltemperatuurne lõõmutus peale erinevaid jahtumisrežiime nihutas PL ribade asukohti veelgi suurema energia poole. Selline PL ribade nihkumine on tingitud kahest asjaolust - Cu-Zn korrastatus suurendab keelutsooni energia väärtust ja toimub muutus erinevat tüüpi defektide kiirguslikes rekombinatsiooni kanalites.

$\text{Cu}_2\text{ZnSnS}_4$ -baasil valmistatud monoterakiht-päikesepatareide voolu-pinge sõltuvuste mõõtmistest järeldus, et madaltemperatuurne käsitus avaldab suurt mõju päikesepatarei väljundparameetritele, suurendades peamiselt avatud vooluahela pinget (V_{oc}) väärtusi. Leiti, et optimaalne madaltemperatuurne lõõmutusrežiim $\text{Cu}_2\text{ZnSnS}_4$ monoterapulbri struktuurse korrastatuse parandamiseks on 4 tundi 150 °C juures. Sellist töötlusrežiimi rakendades paranes monoterakiht-päikesepatareide kasutegur 8,1%-lt 9,1%-le. Antud uurimistöö raames saadud 784 mV on seni teadaolevalt kõrgeim $\text{Cu}_2\text{ZnSnS}_4$ -baasil päikesepatareides mõõdetud V_{oc} väärtus.

Käesolevas doktoritöös näitasime esmakordselt eksperimentaalselt, et stanniitse struktuuriga $\text{Cu}_2\text{CdSnS}_4$ materjalis esineb sarnaselt kesteriitse struktuuriga $\text{Cu}_2\text{ZnSnS}_4$ materjalile Cu-Cd korrastamatus kristallstruktuuris, mida on samuti võimalik reguleerida madaltemperatuurse lõõmutusega. Töös uuriti madaltemperatuurse lõõmutuse mõju temperatuuride vahemikus 100-400 °C $\text{Cu}_2\text{CdSnS}_4$ polükristallilise pulbri struktuursetele ja optoelektronsetele omadustele.

Erinevatel temperatuuridel lõõmutatud polükristallilise $\text{Cu}_2\text{CdSnS}_4$ materjali PL spektrid koosnevad ühest laiast asümmeetrilisest ribast. Väiksema energiaga piigi asukoht 1,064 eV vastab kõige väiksema korrastatusega materjalile ja 1,215 eV vastab kõige suurema korrastatusega materjalile.

Raman ja madaltemperatuurse PL analüüsi põhjal leiti, et kriitline temperatuur (T_c) asub vahemikus 200 kuni 250 °C.

Leiti, et sarnaselt $\text{Cu}_2\text{ZnSnS}_4$ materjalile muutuvad koos kristallstruktuuri korrastatuse astmega $\text{Cu}_2\text{CdSnS}_4$ materjalis ka optoelektronsete omadused, sealhulgas kiirgusliku rekombinatsiooni mehhanism.

Võimalikuks domineerivaks defektikompleksiks vähekorrasstatud $\text{Cu}_2\text{CdSnS}_4$ materjalis on $[2\text{Cu}_{\text{Cd}} + \text{Sn}_{\text{Cd}}]$ ja suurima korrastatusega $\text{Cu}_2\text{CdSnS}_4$ materjalis esinevad koos $[2\text{Cu}_{\text{Cd}} + \text{Sn}_{\text{Cd}}]$ ja $[\text{Cu}_{\text{Cd}} + \text{Cd}_{\text{Cu}}]$ defektikompleksid. Võttes arvesse PL riba intensiivsuse analüüsi, võib järeldada, et üldine eelpool nimetatud defektikomplekside kontsentratsioon korrastatud materjalis väheneb.

REFERENCES

- [1] <https://yearbook.enerdata.net/energy-consumption-data.html>.
- [2] A. Walsh, S. Chen, S.-H. Wey, X.-G. Gong, Kesterite thin-film solar cells: Advances in Materials modelling of $\text{Cu}_2\text{ZnSnS}_4$, *Adv. Energy Mater.* (2012) 2, 400–409.
- [3] <https://www.ise.fraunhofer.de/content/dam/ise/de/documents/publications/studies/Photovoltaics-Report.pdf>.
- [4] K. Yoshikawa, H. Kawasaki, W. Yoshida, T. Irie, K. Konishi, K. Nakano, T. Uto, D. Adachi, M. Kanematsu, H. Uzu, K. Yamamoto, Silicon heterojunction solar cell with interdigitated back contacts for a photoconversion efficiency over 26%, *Nature Energy* (2017) 2, 17032; DOI:10.1038/nenergy.2017.32.
- [5] <http://investor.firstsolar.com>.
- [6] P. Jackson, R. Wuerz, D. Hariskos, E. Lotter, W. Witte, M. Powalla, Effects of heavy alkali elements in $\text{Cu}(\text{In,Ga})\text{Se}_2$ solar cells with efficiencies up to 22.6%, *Phys. Status Solidi RRL* (2016) 10, No. 8, 583–586; DOI:10.1002/pssr.201600199.
- [7] J. Kim, H. Hiroi, T.K. Todorov, O. Gunawan, M. Kuwahara, T. Gokemen, D. Nair, M. Hopstaken, B. Shin, Y. S. Lee, W. Wang, H. Sugimoto, D.B. Mitzi, High efficiency $\text{Cu}_2\text{ZnSn}(\text{S,Se})_4$ solar cell by applying a double $\text{In}_2\text{S}_3/\text{CdS}$ emitter, *Adv. Mater.* (2014) 26, 7427–7431; DOI: 10.1002/adma.201402373.
- [8] T. Gokmen, O. Gunawan, T.K. Todorov, D.B. Mitzi, Band tailing and efficiency limitation in kesterite solar cells, *Appl. Phys. Lett.* (2013) 103, 103506; DOI:10.1063/1.4820250.
- [9] D.B. Mitzi, O. Gunawan, T.K. Todorov, K. Wang and S. Guha, The path towards a high-performance solution-processed kesterite solar cell, *Sol. Energy Mater. Sol. Cells* (2011) 95, 1421–1436; DOI: 10.1016/j.solmat.2010.11.028.
- [10] M. Kumar, A. Dubey, N. Adhikari, S. Venkatesan, Q. Qiao, Strategic review of secondary phases, defects and defect-complexes in kesterite CZTS–Se solar cells, *Energy Environ. Sci.* (2015) 8, 3134–3159; DOI: 10.1039/C5EE02153G.
- [11] M.A. Green, K. Emery, Y. Hishikawa, W. Warta, E.D. Dunlop, D.H. Levi, A.W.Y. Ho-Baillie, Solar cell efficiency tables (version 49). *Prog. Photovoltaic* (2017) 25, 3–13.
- [12] S. Rühle, Tabulated values of the Shockley-Queisser limit for single junction solar cells, *Solar Energy* (2016) 130, 139–147, DOI: 10.1016/j.solener.2016.02.015.
- [13] T. Tanaka, T. Nagatomo, D. Kawasaki, M. Nishio, Q. Guo, A. Wakahara, A. Yoshida, H. Ogawa, Preparation of $\text{Cu}_2\text{ZnSnS}_4$ thin films by hybrid sputtering, *J. phys. Chem. Solids* (2005) 66, 1978–1981; DOI:10.1016/j.jpcs.2005.09.037

- [14] M. Dimitrievska, A. Fairbrother, R. Gunder, G. Gurieva, H. Xie, E. Saucedo, A. Pérez-Rodríguez, V. Izquierdo-Roca, S. Schorr, Role of S and Se atoms on the microstructural properties of kesterite $\text{Cu}_2\text{ZnSn}(\text{S}_x\text{Se}_{1-x})_4$ thin film solar cells, *Phys. Chem. Chem. Phys.* (2016) 18, 8692-8700.
- [15] J. Paier, R. Asahi, A. Nagoya, G. Kresse, $\text{Cu}_2\text{ZnSnS}_4$ as a potential photovoltaic material: a hybrid Hartree-Fock density functional theory study, *Phys. Rev. B.* (2009) 115 126.
- [16] A. Nagoya, R. Asahi, R. Wahl, G. Kresse, Defect formation and phase stability of $\text{Cu}_2\text{ZnSnS}_4$ photovoltaic material, *Physical review B* (2010) 81, 113202.
- [17] K. Ito, T. Nakazawa, Electrical and optical properties of stannite-type quaternary semiconductor thin films, *Jpn. J. Appl. Phys.* 27 (1988) 2094-2097.
- [18] H. Matsushita, T. Ichikawa, A. Katsui, Structural, thermodynamical and optical properties of $\text{Cu}_2\text{-II-IV-VI}_4$ quaternary compounds, *Journal of Materials Science* (2005) 40, 2003-2005; DOI: 10.1007/s10853-005-1223-5.
- [19] Y. Cui, G. Wang, D. Pan, Synthesis and photoresponse of novel $\text{Cu}_2\text{CdSnS}_4$ semiconductor nanorods, *J. Mater. Chem.* (2012) 22, 12471.
- [20] L. Meng, Y. Li, B. Yao, Z. Ding, G. Yang, R. Liu, R. Deng, L. Liu, Visible-blind ultraviolet photodetector based on p- $\text{Cu}_2\text{CdSnS}_4$ /n-ZnS heterojunction with a type-I band alignment, *J. Appl. Phys* (2016) 120, 235306.
- [21] H. Katagiri, N. Sasaguchi, S. Hando, S. Hoshino, J. Ohashi, T. Yokota, Preparation and evaluation of $\text{Cu}_2\text{ZnSnS}_4$ thin films by sulfurization of e-b evaporated precursors, *Sol. Energy Mater. Sol. Cells* (1997) 49, 407-414.
- [22] T.K. Todorov, K.B. Reuter, D.B. Mitzi, High-Efficiency Solar Cell with Earth-Abundant Liquid-Processed Absorber, *Advanced Materials* (2010) 22 (20): E156; DOI:10.1002/adma.200904155.
- [23] W. Wang, M.T. Winkler, O. Gunawan, T. Gokmen, T.K Todorov, Y. Zhu, D.B. Mitzi, A 12.6% $\text{Cu}_2\text{ZnSnS}_x\text{Se}_{4-x}$ (CZTSSe) solar cell is presented with detailed device characteristics. *Advanced Materials* (2013) 4 (7): 1301465; DOI:10.1002/aenm.201301465.
- [24] M. Altosaar, J. Raudoja, K. Timmo, M. Danilson, M. Grossberg, M. Krunk, T. Varema, E. Mellikov, $\text{Cu}_2\text{ZnSnSe}_4$ monograin powders for solar cell application, *Proceedings of the 2006 IEEE WCPEC-4*, Hawaii, May 7–12, 2006.
- [25] <https://crystalsol.com>.
- [26] S. Wagner and P. M. Bridenbaugh, *J. Cryst. Growth* (1977) 39, 151.
- [27] W. Zhao, G. Wang, Q. Tian, L. Huang, S. Gao, D. Pan, Solution-processed $\text{Cu}_2\text{CdSn}(\text{S,Se})_4$ thin film solar cells, *Sol. Energy Mater. Sol. Cells* (2015) 133, 15–20.

- [28] Z. Su, J.M.R. Tan, X. Li, X. Zeng, S.K. Batabyal, L.H. Wong, Cation Substitution of Solution-Processed $\text{Cu}_2\text{ZnSnS}_4$ Thin Film Solar Cell with over 9% Efficiency, *Adv. Energy Mater.* (2015) 5, 1500682; DOI: 10.1002/aenm.20.
- [29] C. Yan, K. Sun, J. Huang, S. Johnston, F. Liu, B.P. Veettil, K. Sun, A. Pu, F. Zhou, J.A. Stride, M.A. Green, X. Hao, Beyond 11% Efficient Sulfide Kesterite $\text{Cu}_2\text{Zn}_x\text{Cd}_{1-x}\text{SnS}_4$ Solar Cell: Effects of Cadmium Alloying, *ACS Energy Lett.* (2017) 2, 930–936; DOI: 10.1021/acseenergylett.7b00129.
- [30] T. Shibuya, Y. Goto, Y. Kamihara, M. Matoba, K. Yasuoka, L.A. Burton, A Walsh, From kesterite to stannite photovoltaics: Stability and band gaps of the $\text{Cu}_2(\text{Zn,Fe})\text{SnS}_4$ alloy, *Appl. Phys.* (2014) 104, 021912; DOI: 10.1063/1.4862030.
- [31] S. Schorr, H. J. Hoebler, M. Tovar, A neutron diffraction study of the stannite-kesterite solid solution series, *Eur. J. Mineral.* (2007) 19, 65-73; DOI: 10.1127/0935-1221/2007/0019-0065.
- [32] C. Persson, Electronic and optical properties of $\text{Cu}_2\text{ZnSnS}_4$ and $\text{Cu}_2\text{ZnSnSe}_4$, *Journal of Applied Physics* (2010) 107, 5, 053710-053710-8; DOI: 10.1063/1.3318468.
- [33] S. Schorr, The crystal structure of kesterite type compounds: A neutron and X-ray diffraction study, *Sol. Energy Mater. Sol. Cells* (2011) 95, 1482-1488.
- [34] H. Nozaki, T. Fukano, S. Ohta, Y. Seno, H. Katagiri, K. Jimbo, Crystal structure determination of solar cell materials: $\text{Cu}_2\text{ZnSnS}_4$ thin films using X-ray anomalous dispersion, *J. Alloy. Compd.* (2012) 524, 22–25.
- [35] S. Siebentritt, S. Schorr, Kesterites-a challenging material for solar cells, *Prog. Photovoltaics Res. Appl.* (2012) 20, 512–519.
- [36] S. Chen, X.G. Gong, A. Walsh, S.H. Wei, Electronic structure and stability of quaternary chalcogenide semiconductors derived from cation cross-substitution of II–VI and I–III–VI₂ compounds, *Phys. Rev. B* (2009) 79, 165211.
- [37] W. Schäfer, R. Nitsche: *Mater. Res. Bull.* (1974) 9, 645.
- [38] S. A. Kissin, D. R. Owens, Cernite, a copper-cadmium-tin sulfide with the stannite structure, *Canadian Mineralogist* (1978) 16, 139-146.
- [39] S. Chen, A. Walsh, X.-G. Gong, S.-H. Wei, Classification of lattice defects in the kesterite $\text{Cu}_2\text{ZnSnS}_4$ and $\text{Cu}_2\text{ZnSnSe}_4$ earth-abundant solar cell absorbers, *Adv. Mater.* (2013) 25, 1522-1539.
- [40] S. Chen, X. Gong, A. Walsh, S.-H. Wei, Defect physics of the kesterite thin-film solar cell absorber $\text{Cu}_2\text{ZnSnS}_4$, *Appl. Phys. Lett.* (2010) 96, 021902.
- [41] A. Nagoya, R. Asahi, R. Wahl, G. Kresse, Defect formation and phase stability of $\text{Cu}_2\text{ZnSnS}_4$ photovoltaic material, *Physical review B* (2010) 81, 113202.
- [42] Z.-K. Yuan, S. Chen, H. Xiang, X.-G. Gong, A. Walsh, J.S. Park, I. Repins, S.-H. Wei, Engineering solar cell absorbers by exploring the

band alignment and defect disparity: the case of Cu- and Ag-based kesterite compounds, *Adv. Funct. Mater.* (2015) 25, 6733-6743.

- [43] <https://www.webelements.com>.
- [44] S. Chen, J.H. Yang, X.G. Gong, A. Walsh, S.H. Wei, Intrinsic point defects and complexes in the quaternary kesterite semiconductor $\text{Cu}_2\text{ZnSnS}_4$, *Physical Review B* (2010) 81(24), 245204.
- [45] I. Repins, N. Vora, C. Beall, S.H. Wei, Y. Yan, M. Romero, G. Teeter, H. Du, B. To, M. Young, R. Noufi, Kesterites and chalcopyrites: A comparison of close cousins, *Proceedings of the Materials Research Society Spring Meeting* (2011), San Francisco (USA) (2011) NREL/CP-5200-51286.
- [46] X. Liu, Y. Feng, H. Cui, F. Liu, X. Hao, G. Conibeer, D.B. Mitzi, M. Green, The current status and future prospects of kesterite solar cells: a brief review, *Prog. Photovolt: Res. Appl.* (2016) 24, 879-898, DOI: 10.1002/pip.2741.
- [47] H. Katagiri, K. Jimbo, W.S. Maw, K. Oishi, M. Yamazaki, H. Araki, Development of CZTS-based thin film solar cells, *Thin Solid Films* (2009) 517, 2455-2460.
- [48] K. Tanaka, M. Oonuki, N. Moritake, H. Uchiki, $\text{Cu}_2\text{ZnSnS}_4$ thin film solar cells prepared by non-vacuum processing, *Sol. Energy Mater. Sol. Cells* (2009) 93, 583-587.
- [49] A. Ennaoui, M. Lux-Steiner, A. Weber, D. Abou-Ras, I. Kötschau, H.W. Schock, R. Schurr, A. Hölzing, S. Jost, R. Hock, T. Voß, J. Schulze, A. Kirbs, $\text{Cu}_2\text{ZnSnS}_4$ thin film solar cells from electroplated precursors: Novel low-cost perspective, *Thin Solid Films* (2009) 517, 2511-2514. DOI: 10.1016/j.tsf.2008.11.061.
- [50] Q. Cao, O. Gunawan, M. Copel, K.B. Reuter, S.J. Chey, V.R. Deline, D.B. Mitzi, Defects in $\text{Cu}(\text{In,Ga})\text{Se}_2$ Chalcopyrite Semiconductors: A Comparative Study of Material Properties, Defect States, and Photovoltaic Performance *Adv. Energy Mater.* (2011) 1, 845-853.
- [51] Y. Cao, M.S. Denny Jr., J.V. Caspar, W.E. Farneth, Q. Guo, A.S. Ionkin, L.K. Johnson, M. Lu, I. Malajovich, D. Radu, H.D. Rosenfeld, K.R. Choudhury, W. Wu, High-efficiency solution-processed $\text{Cu}_2\text{ZnSn}(\text{S,Se})_4$ thin-film solar cells prepared from binary and ternary nanoparticles, *J. Am. Chem. Soc.* (2012) 134, 15644.
- [52] J.J.S. Scragg, L. Choubrac, A. Lafond, T. Ericson, C. Platzer-Björkman. A low-temperature order–disorder transition in $\text{Cu}_2\text{ZnSnS}_4$ thin films, *Applied Physics Letters* (2014) 104, 041911.
- [53] G. Rey, A. Redinger, J. Sendler, T.P. Weiss, M. Thevenin, M. Guennou, B. El Adib, S. Siebentritt, The band gap of $\text{Cu}_2\text{ZnSnSe}_4$: effect of order–disorder, *Applied Physics Letters* (2014) 105, 112106.
- [54] G. Krämmmer, C. Huber, T. Schnabel, C. Zimmermann, M. Lang, E. Ahlswede, H. Kalt, M. Hetterich, Order-disorder related band gap changes in $\text{Cu}_2\text{ZnSn}(\text{S,Se})_4$: Impact on solar cell performance, *Proc. 42nd IEEE Photovoltaic Specialist Conference (PVSC)* (2015).

- [55] L. Choubrac, M. Paris, A. Lafond, C. Guillot-Deudon, X. Rocquefelte, S. Jobic, Multinuclear (^{67}Zn , ^{119}Sn and ^{65}Cu) NMR spectroscopy – an ideal technique to probe the cationic ordering in $\text{Cu}_2\text{ZnSnS}_4$ photovoltaic materials, *Phys. Chem. Chem. Phys.* (2013) 15, 10722-10725; DOI: 10.1039/c3cp51320c.
- [56] M. Grossberg, J. Krustok, J. Raudoja, T. Raadik, The role of structural properties on deep defect states in $\text{Cu}_2\text{ZnSnS}_4$ studied by photoluminescence spectroscopy, *Appl. Phys. Lett.* (2012) 101, 102102; DOI: 10.1063/1.4750249.
- [57] J.J.S. Scragg, J.K. Larsen, M. Kumar, C. Persson, J. Sandler, S. Siebentritt, C.P. Björkman, Cu-Zn disorder and band gap fluctuation in $\text{Cu}_2\text{ZnSn}(\text{S},\text{Se})_4$: Theoretical and experimental investigations, *Phys. Status Solidi B* (2016) 253, 2, 247-254; DOI 10.1002/pssb.201552530.
- [58] S. Bourdais, C. Choné, B. Delatouche, A. Jacob, G. Larramona, C. Moisan, A. Lafond, F. Donatini, G. Rey, S. Siebentritt, A. Walsh, G. Dennler, Is the Cu/Zn disorder the main culprit for the voltage deficit in kesterite solar cells?, *Adv. Energy Mater.* (2016) 1502276.
- [59] G.H. Vineyard, Theory of order–disorder kinetics, *Phys. Rev* (1956) 102, 981–992.
- [60] A. Ritscher, M. Hoelzel, M. Lerch, The order-disorder transition in $\text{Cu}_2\text{ZnSnS}_4$ – A neutron scattering investigation, *Journal of Solid State Chemistry* (2016) 238, 68-73.
- [61] M. Grossberg, J. Krustok, T. Raadik, M. Kauk-Kuusik, J. Raudoja. Photoluminescence study of disordering in the cation sublattice of $\text{Cu}_2\text{ZnSnS}_4$, *Current Applied Physics* (2014) 14, 1424-1427.
- [62] T. Gürel, C. Sevik, T. Çağın, Characterization of vibrational and mechanical properties of quaternary compounds $\text{Cu}_2\text{ZnSnS}_4$ and $\text{Cu}_2\text{ZnSnSe}_4$ in kesterite and stannite structures, *Phys. Rev. B* (2011) 84205201; DOI: 10.1103/PhysRevB.84.205201.
- [63] M.Y. Valakh, O.F. Kolomys, S.S. Ponomaryov, V.O. Yukhymchuk, I.S. Babichuk, V. Izquierdo-Roca, E. Saucedo, A. Perez-Rodriguez, J.R. Morante, S. Schorr, I.V. Bodnar, Raman scattering and disorder effect in $\text{Cu}_2\text{ZnSnS}_4$, *Phys. Status Solidi RRL* 7 (2013) 4, 258–261; DOI: 10.1002/pssr.201307073.
- [64] S. Chen, X.G. Gong, A. Walsh, S.-H. Wei, Crystal and electronic band structure of $\text{Cu}_2\text{ZnSnS}_4$ (X=S and Se) photovoltaic absorbers: first-principles insights, *Appl. Phys. Lett* (2009) 94 (4), 041903; DOI: 10.1063/1.3074499.
- [65] M. Grossberg, T. Raadik, J. Raudoja, J. Krustok, Photoluminescence study of defect clusters in $\text{Cu}_2\text{ZnSnS}_4$ polycrystals, *Curr. Appl. Phys.* (2014) 14, 447.
- [66] W. Schockley, H. J. Queisser, *Journal of Applied Physics* (1961) 32, 519.
- [67] K. Timmo, M. Altosaar, J. Raudoja, K. Muska, M. Pilvet, M. Kauk, T.Varema, M. Danilson, O. Volobujeva, E. Mellikov, Sulfur-containing

- Cu₂ZnSnSSe₄ monograin powders for solar cells, *Sol. Energy Mater. Sol. Cells* (2010) 94, 1889;
- [68] Y. Cao, Y. Xiao, J.-Y. Jung, H.-D. Um, S.-W. Jee, H. M. Choi, J.H. Bang, J.-H. Lee, Highly Electrocatalytic Cu₂ZnSn(S_{1-x}Se_x)₄ Counter Electrodes for Quantum-Dot-Sensitized Solar Cells, *Appl. Mater. Interfaces*, (2013) 5, 479; DOI: 10.1021/am302522c.
- [69] Y.P. Wang, S. Levenco, D.O. Dumcenco, Y.S. Huang, C.H. Ho, K.K. Tiong, Composition Dependent Band Gaps of Single Crystal Cu₂ZnSn(S_xSe_{1-x})₄ Solid Solutions, *Solid State Phenomena* (2013) 194, 139-143.
- [70] Y. Zhang, Y. Sun, Investigation of S/Se ratio on the properties of solution-processed, CZTSSe solar cell, *Chalcogenide Letters* (2016) 9, 397 – 402.
- [71] Z.-Y. Xiao, Y.-Fe. Li, B. Yao, R. Deng, Z.-H. Ding, T. Wu, G. Yang, C.-R. Li, Z.-Y. Dong, L. Liu, L.-G. Zhang, H.-Fe. Zhao, Bandgap engineering of Cu₂Cd_xZn_{1-x}SnS₄ alloy for photovoltaic applications: A complementary experimental and first-principles study, *J. Appl. Phys.* (2013) 114, 183506; DOI: 10.1063/1.4829457.
- [72] Q. Zhang, H. Deng, L. Chen, L. Yu, J. Tao, L. Sun, P. Yang, J. Chu, Cation substitution induced structural transition, band gap engineering and grain growth of Cu₂Cd_xZn_{1-x}SnS₄ thin films, *Journal of Alloys and Compounds* (2017) 695, 482-488; DOI: 10.1016/j.jallcom.2016.11.121.
- [73] S. Bag, O. Gunawan, T. Gokmen, Y. Zhu, D.B. Mitzi, Hydrazine-processed Ge-substituted CZTSe solar cells, *Chem. Mater.* (2012) 24, 4588–4593; DOI: 10.1021/cm302881g.
- [74] X. Peng, S. Zhang, Y. Xiang, Solvothermal synthesis of Cu₂Zn(Sn_{1-x}Ge_x)S₄ and Cu₂(Sn_{1-x}Ge_x)S₃ nanoparticles with tunable band gap energies, *Journal of Alloys and Compounds* (2015) 640, 75–81; DOI: 10.1016/j.jallcom.2015.03.248.
- [75] M. Grossberg, K. Timmo, T. Raadik, E. Kärber, V. Mikli, J. Krustok, Study of structural and optoelectronic properties of Cu₂Zn(Sn_{1-x}Ge_x)Se₄ (x = 0 to 1) alloy compounds, *Thin Solid Films*, (2015) 582, 176-179; DOI: 10.1016/j.tsf.2014.10.055.
- [76] <http://plasticphotovoltaics.org/lc/lc-solarcells/lc-introduction.html>.
- [77] E. Mellikov, M. Altosaar, M. Kauk-Kuusik, K. Timmo, D. Meissner, M. Grossberg, J. Krustok, O. Volobujeva, Growth of CZTS-based monograins and application to membrane solar cells, Copper Zinc Tin Sulfide-Based Thin-Film Solar Cells, First Edition. Edited by K. Ito. Published (2015) by John Wiley & Sons, Ltd.
- [78] T.S. te Velde, G.W.T. van Helden, Monograin layers, Philips technical review, volume 29.
- [79] T. Bergfors, “Tutorial 6: Ostwald Ripening” (online); <http://xray.bmc.uu.se/terese/tutorial6.html>.
- [80] I.D. Olekseyuk, I.V. Dudchak, L.V. Piskach, Phase equilibria in the Cu₂S-ZnS-SnS₂ system, *J. Alloys Compd* (2004) 368, 135-143.

- [81] R. Wagner, H. D. Wiemhöfer, Hall effect and conductivity in thin films of low temperature chalcocite Cu_2S at 20 °C as a function of stoichiometry, *Journal of Physics and Chemistry of Solids* (1983) 44, 801–805.
- [82] C. Wu, Z. Hu, C. Wang, H. Sheng, J. Yang, Y. Xie, Hexagonal Cu_2SnS_3 with metallic character: Another category of conducting sulfides, *Applied Physics Letters* (2007) 91, 143104.
- [83] L.V. Piskach, O.V. Parasyuk, I.D. Olekseyuk, The phase equilibria in the quasi-ternary Cu_2S - CdS - SnS_2 system, *J. Alloys Compd* (1998) 279, 142–152.
- [84] E.G. Osadchii, Solid solutions and phase relations in the system Cu_2SnS_3 - ZnS - CdS at 850°C and 700°C, *Reviews in Mineralogy and Geochemistry*, (1996).
- [85] M. Kauk-Kuusik, K. Timmo, M. Danilson, M. Altosaar, M. Grossberg, K. Ernits, P-n junction improvements of $\text{Cu}_2\text{ZnSnS}_4/\text{CdS}$ monograin layer solar cells, *Applied Surface Science* (2015) 357, 795–798, <http://doi.org/10.1016/j.apsusc.2015.09.094>.
- [86] K. Timmo, M. Altosaar, J. Raudoja, M. Grossberg, M. Danilson, O. Volobujeva, E. Mellikov, Chemical etching of $\text{Cu}_2\text{ZnSn}(\text{S},\text{Se})_4$ monograin powder, *Proc. of the 35th IEEE Photovoltaic Specialists Conference*, June 20-25, Honolulu, Hawaii (2010), 001982.
- [87] M. Kauk, K. Muska, M. Altosaar, J. Raudoja, M. Pilvet, T. Varema, K. Timmo, O. Volobujeva, Effects of sulphur and tin disulphide vapour treatments of $\text{Cu}_2\text{ZnSnS}(\text{Se})_4$ absorber materials for monograin solar cells, *Energy Procedia* (2011) 10, 197–202; DOI: 10.1016/j.egypro.2011.10.177.
- [88] M. Danilson, Temperature dependent electrical properties of kesterite monograin layer solar cells: doctoral theses. Tallinn, Tallinn University of Technology, 2013.
- [89] J. Krustok, R. Josepson, T. Raadik, M. Danilson, Potential fluctuations in $\text{Cu}_2\text{ZnSnS}_4$ solar cells studied by temperature dependence of quantum efficiency curves, *Physica B* (2010) 405, 3186.
- [90] T. Maeda, S. Nakamura, T. Wada First-principles study on Cd doping in $\text{Cu}_2\text{ZnSnS}_4$ and $\text{Cu}_2\text{ZnSnSe}_4$, *Jpn. J. Appl. Phys.* (2012) 51 (10NC11-1-10NC-6).
- [91] M. Grossberg, J. Krustok, J. Raudoja, K. Timmo, M. Altosaar, T. Raadik, Photoluminescence and Raman study of $\text{Cu}_2\text{ZnSn}(\text{Se}_x\text{S}_{1-x})_4$ monograins for photovoltaic applications, *Thin Solid Films* (2011) 519, 7403–7406.
- [92] X. Fontané, V. Izquierdo-Roca, E. Saucedo, S. Schorr, V.O. Yukhymchuk, M.Y. Valakh, A. Pérez-Rodríguez, J.R. Morante, Vibrational properties of stannite and kesterite type compounds: Raman scattering analysis of $\text{Cu}_2(\text{Fe},\text{Zn})\text{SnS}_4$, *J. Alloys Compd.* (2012) 539, 190–194.
- [93] M. Paris, L. Choubrac, A. Lafond, C. Guillot-Deudon, and S. Jobic, Solid-State NMR and Raman Spectroscopy To Address the Local

Structure of Defects and the Tricky Issue of the Cu/Zn Disorder in Cu-Poor, Zn-Rich CZTS Materials, *Inorg. Chem.* (2014) 53, 8646-8653.

- [94] H. Guo, Y. Li, X. Fang, K. Zhang, J. Ding, Co-sputtering deposition and optical-electrical characteristic of $\text{Cu}_2\text{CdSnS}_4$ thin films for use in solar cells, *Materials Letters* (2016) 162, (1) 97–100.
- [95] J. Krustok, H. Collan, M. Yakushev, K. Hjelt, The role of spatial potential fluctuations in the shape of the PL bands of multinary semiconductor compounds, *Physica Scripta*, T79 (1999) 179-182.
- [96] M. Grossberg, J. Krustok, K. Timmo, M. Altosaar, Radiative recombination in $\text{Cu}_2\text{ZnSnSe}_4$ monograins studied by photoluminescence spectroscopy, *Thin Solid Films* (2009) 517, 2489 – 2492.
- [97] A.P. Levanyuk, V.V. Osipov, Edge luminescence of direct-gap semiconductors, *Sov. Phys. Usp.* (1981) 24, 187 – 215.
- [98] J. Krustok, H. Collan, K. Hjelt, Does the low temperature Arrhenius plot of the photoluminescence intensity in CdTe point towards an erroneous activation energy?, *J. Appl. Phys.* (1997) 81, 1442 – 1445.

APPENDIX A

PAPER I

M. Pilvet, M. Kauk-Kuusik, M. Altosaar, M. Grossberg, M. Danilson, K. Timmo, A. Mere, V. Mikli, Compositionally tunable structure and optical properties of $\text{Cu}_{1.85}(\text{Cd}_x\text{Zn}_{1-x})_{1.1}\text{SnS}_{4.1}$ ($0 \leq x \leq 1$) monograin powders, *Thin Solid Films* 582 (2015) 180–183.



Compositionally tunable structure and optical properties of $\text{Cu}_{1.85}(\text{Cd}_x\text{Zn}_{1-x})_{1.1}\text{SnS}_{4.1}$ ($0 \leq x \leq 1$) monograin powders

M. Pilvet^{*}, M. Kauk-Kuusik, M. Altosaar, M. Grossberg, M. Danilson, K. Timmo, A. Mere, V. Mikli

Tallinn University of Technology, Ehitajate tee 5, 19086 Tallinn, Estonia

ARTICLE INFO

Available online 5 November 2014

Keywords:

Kesterite
Stannite
Solid solutions
Monograin powder

ABSTRACT

$\text{Cu}_{1.85}(\text{Cd}_x\text{Zn}_{1-x})_{1.1}\text{SnS}_{4.1}$ ($0 \leq x \leq 1$) solid solutions were synthesized in the form of monograin powders and characterized by X-ray diffraction (XRD), Raman spectroscopy, photoluminescence (PL) and quantum efficiency (QE) measurements. From the XRD data, the lattice parameters for all powders were calculated. The XRD peaks were shifted linearly to the lower angle side with increasing cadmium content and the splitting of (220) peak appeared for the sample $x = 0.4$. With increasing the value of x from 0 to 0.4, a linear shift of the A_1 Raman mode from 338 cm^{-1} to 332 cm^{-1} , a shift of the PL band from 1.3 eV to 1.1 eV and the change of effective bandgap from 1.55 eV to 1.41 eV calculated from QE measurements were observed. Further increase in Cd content over $x = 0.4$ did not have a major impact to these parameters. We attributed this phenomenon to the phase transition from kesterite to stannite in the series of $\text{Cu}_{1.85}(\text{Cd}_x\text{Zn}_{1-x})_{1.1}\text{SnS}_{4.1}$ ($0 \leq x \leq 1$) solid solutions.

© 2014 Elsevier B.V. All rights reserved.

1. Introduction

Lately, quaternary chalcogenide semiconductors, $\text{Cu}_2\text{M}^{\text{II}}\text{M}^{\text{IV}}(\text{S}; \text{Se})_4$ ($\text{M}^{\text{II}} = \text{Mn, Fe, Co, Ni, Zn, Cd, and Hg}$; $\text{M}^{\text{IV}} = \text{Si, Ge, and Sn}$), have attracted considerable interest for applications in solar cells and other optical devices due to their appropriate direct band gap and low-cost manufacturing [1–3]. Solar cells with efficiencies as high as 12.6% have already been achieved using $\text{Cu}_2\text{ZnSn}(\text{S,Se})_4$ (CZTSSe) [4]. Other quaternary chalcogenides, such as $\text{Cu}_2\text{Zn}(\text{Sn,Ge})\text{Se}_4$ [5] and $\text{Cu}_2\text{CdSnS}_4$ [6], have shown efficiencies up to 9.1% and 2.7%, respectively.

Theoretical calculations suggest that the best fit with solar spectrum and therefore the optimal bandgap for absorber materials is around 1.4 eV. To reach the ideal bandgap for CZTSSe-based single junction solar cells, the ratio of S/Se is modified in several studies [7–9]. Recently, synthesis of $\text{Cu}_2\text{Cd}_x\text{Zn}_{1-x}\text{SnS}_{4.1}$ ($0 \leq x \leq 1$) (CCdZTS) alloy thin films by sol-gel method has been reported [10] to realize the goal of bandgap engineering in $\text{Cu}_2\text{ZnSnS}_4$ -based solar cells. Xiao et al. reported that the optical bandgap of CCdZTS alloy can be also modified continuously from 1.55 to 1.09 eV as Cd varies from 0 to 1. However, it is not the case for monograin powders. In our previous study [6], we found that the effective bandgap energy of $\text{Cu}_2\text{CdSnS}_4$ is 1.4 eV. In order to clarify the mismatch, the (CCdZTS) solid solutions in the form of monograin powders were synthesized and studied. $\text{Cu}_2\text{ZnSnS}_4$ compound has been found to exist in the kesterite structure ($\bar{I}4$) with lattice parameter values $a = 5.428 \text{ \AA}$ and $c = 10.864 \text{ \AA}$ [11] and $\text{Cu}_2\text{CdSnS}_4$ in the stannite structure ($\bar{I}42m$) with lattice parameters $a = 5.586 \text{ \AA}$ and $c = 10.834 \text{ \AA}$ [12]. In the case of CCdZTS solid solutions, the region of their crystal

structure transition is unclear. The present work reports the results of the synthesis and characterization of the (CCdZTS) solid solutions with the aim of finding the optimal Cd content in solid solutions for ideal band gap of CCdZTS-based single junction solar cells.

2. Experimental details

$\text{Cu}_{1.85}(\text{Cd}_x\text{Zn}_{1-x})_{1.1}\text{SnS}_{4.1}$ solid solutions with $0 \leq x \leq 1$ were synthesized from high purity CuS, ZnS, CdS, SnS binary compounds and elemental S in the molten phase of KI by using monograin powder technology. The precursors mixture and KI were ground in desired amounts in an agate mortar. The milled powder was placed in quartz ampoules which were sealed under vacuum. For the synthesis, the temperature of the furnace was increased from room temperature to 1013 K with a rate of 240 K/min and kept at elevated temperature for 120 h. The formation of CCdZTS monograin powders takes place during the heating process in the molten phase of the flux. Initial solid particles of low-solubility precursors react with each other in the molten salt media, and the formed solid particles of the product compound start to recrystallize and grow by the mechanism of Ostwald ripening [13]. More details about monograin powder formation is given in [14]. The crystals growth was discontinued by cooling the ampoules in the air. The flux was removed by leaching with deionized water and released monograin powders were dried. For future technological processes, the grains with diameters of 63–75 μm were selected by sieving. As-grown monograins were chemically etched in fresh-made 1% bromine ethanol for 5 min followed by 10% KCN aqueous solution for 5 min. After etching, the powders were annealed at 1013 K for 1 h with the presence of sulfur atmosphere. The process parameters for chemical etching and thermal annealing were based on the earlier studies [15,16].

^{*} Corresponding author.

Table 1
Compositional ratios of $\text{Cu}_{1.85}(\text{Cd}_x\text{Zn}_{1-x})_{1.1}\text{SnS}_{4.1}$ monograin powders.

[Cd]/([Cd] + [Zn]) in precursors	Compositional ratios in powders				
	[Cd]/([Cd] + [Zn])	[Cu]/([Cd] + [Zn] + [Sn])	([Cd] + [Zn])/[Sn]	[Cu]/[Sn]	[S]/[Met]
0	0	0.93	1.03	1.90	1.01
0.2	0.18	0.92	1.06	1.89	1.02
0.4	0.38	0.89	1.08	1.87	1.03
0.6	0.57	0.90	1.05	1.84	1.03
0.8	0.78	0.90	1.02	1.82	1.02
1	1	0.92	0.97	1.82	1.04

The chemical composition of the synthesized monograin powders was analyzed by energy dispersive X-ray spectroscopy (EDX) on Zeiss HR SEM ULTRA 55 with accelerating voltage of 20 kV and a beam current of 3 nA. The phase composition of the powders was studied by room-temperature micro-Raman spectroscopy using Horiba's LabRam HR spectrometer with incident laser light with wavelength of 532 nm. The crystalline structure was characterized by X-ray diffraction (XRD) using a Rigaku Ultima IV diffractometer with monochromatic Cu α radiation $\lambda = 1.54056 \text{ \AA}$ at 40 kV and 40 mA, using a D/teX Ultra silicon strip detector. For photoluminescence (PL) measurements, the powder samples were mounted in the closed-cycle He cryostat and cooled down to 10 K. The 658 nm laser line was used for PL excitation and the PL spectra were detected by InGaAs detector. The annealed CCdZTS monograin powders were used as absorber materials in monograin layer (MGL) solar cells. MGL consists of a monolayer of powder grains embedded into a layer of epoxy resin with thickness of two-thirds of the grain diameter. The open surface of the monograins was covered with CdS buffer layer by chemical bath deposition followed by radio frequency sputtering of $i\text{-ZnO}$ and ZnO:Al layers. Silver paste was applied for front contact and graphite paste for back contact. The bandgap values of the synthesized absorber materials were estimated by quantum efficiency (QE) measurements of monograin layer MGL solar cells. QE measurements were performed using a computer controlled SPM-2 monochromator and a 250 W halogen lamp.

3. Results and discussions

3.1. Composition and crystal structure of CCdZTS solid solutions

The compositional ratios of elements of the CCdZTS solid solutions determined from EDX analysis are listed in Table 1. The results confirm

that the value of $x = [\text{Cd}]/([\text{Cd}] + [\text{Zn}])$ in synthesized powders is close to the input value of x in precursors. It can be seen that the [Cu]/[Sn] ratio in the monograin powders decreases by increasing Cd content in precursors. We suppose that the [Cu]/[Sn] ratio decreases due to the partial substitution of Cu vacancies by Cd atoms in Cu-poor CCdZTS. Fig. 1a shows the XRD patterns of monograin powders of CCdZTS solid solutions. The major diffraction peaks are indexed as corresponding to the (112), (200), (220), (312) and (332) planes of kesterite phase of $\text{Cu}_2\text{ZnSnS}_4$ (ICDD PDF2008, 01-075-4122) and stannite phase of $\text{Cu}_2\text{CdSnS}_4$ (ICDD (PDF2008), 00-029-0537). Fig. 1b shows the enlarged view of the (112) diffraction peaks. The peaks are shifted to the lower angle side with increasing Cd content in the CCdZTS solid solutions. The splitting of the profiles of (220) and (204) reflections due to the lattice distortion caused by the replacement of Zn by Cd for different x values is shown in Fig. 1c. The splitting of the (220) peak increases up to $x = 0.4$. Then, besides the splitting, the high angle peak (204) appears and both (220) and (204) peaks are visible separately. The high angle peak (204) narrows with increasing Cd content.

Lattice constants for all powders were calculated from the XRD data (Fig. 2). The a -axis lattice constant increases almost linearly from 5.433 to 5.593 \AA as the Cd content increases from 0 to 1. The expansion of lattice constant can be attributed to the larger ion radius of Cd than that of Zn or Cu. The simplest possibility is that Cd substitutes other metal atoms at their sites in crystal lattice of CCdZTS. As the theoretically calculated substitution energies of Cd atoms at Cu, Sn and Zn atom sites in CZTS lattice are $E_{\text{sub}}(\text{Cd}_{\text{Cu}}) = 0.69 \text{ eV}$, $E_{\text{sub}}(\text{Cd}_{\text{Sn}}) = 1.07 \text{ eV}$ and $E_{\text{sub}}(\text{Cd}_{\text{Zn}}) = 0.53 \text{ eV}$ [17], the most likely is the isoelectronic substitution of Cd at the Zn site. The presence of Cu vacancies, formed easily in Cu-poor and Zn-rich growth conditions, promotes Cd substitution at Cu sites and formation of charge-neutral ($\text{Cd}_{\text{Cu}} + \text{V}_{\text{Cu}}$) pairs [17].

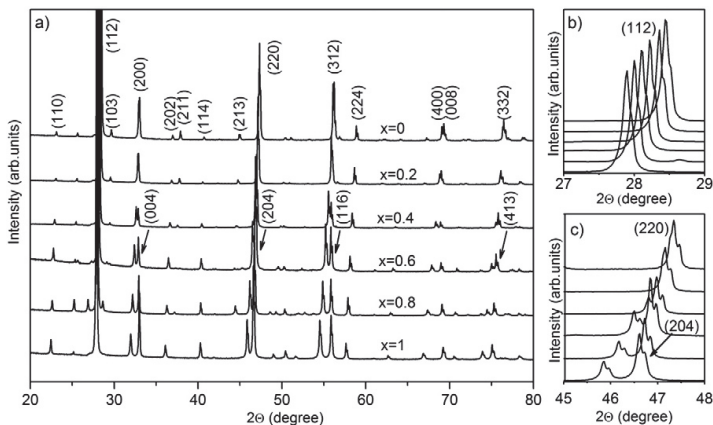


Fig. 1. a) XRD patterns of monograin powders of $\text{Cu}_{1.85}(\text{Cd}_x\text{Zn}_{1-x})_{1.1}\text{SnS}_{4.1}$ solid solutions with $0 \leq x \leq 1$; b) enlarged view of the (112) diffraction peaks and c) splitting of the profiles of the (220) and (204) reflections.

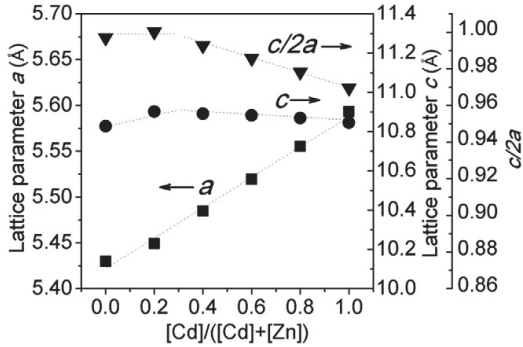


Fig. 2. Lattice parameters of a, c and c/2a as a function of Cd content in $\text{Cu}_{1.85}(\text{Cd}_x\text{Zn}_{1-x})_{1.1}\text{SnS}_{4.1}$.

The ratio of the lattice parameters c/2a for CCdZTS in dependence of chemical composition is shown also in Fig. 2. Schorr et al. carried out a neutron diffraction study of the $\text{Cu}_2\text{Fe}_{1-x}\text{Zn}_x\text{SnS}_4$ solid solutions, obtaining that the ratio of the lattice constants c/2a is equal to or greater than 1.0 for kesterite-type structure [11]. According to this, we could assume that CCdZTS solid solutions have kesterite-type structure in the region $0 \leq x \leq 0.3$ and in the region $0.4 \leq x \leq 1$ they exist in stannite-type structure.

In order to find out the existence of the secondary phases and confirm the stannite–kesterite transition point, the Raman measurements were performed. A linear shift of the A_1 Raman mode of CCdZTS towards lower wavenumbers (from 338 cm^{-1} to 332 cm^{-1}) with increasing Cd content in powders is demonstrated in the region $0 \leq x < 0.4$ (Fig. 3). Subsequent increasing of Cd concentration did not change the frequency of A_1 mode. The other Raman peaks for $\text{Cu}_2\text{ZnSnS}_4$ and for $\text{Cu}_2\text{CdSnS}_4$ correspond well to data in the literatures [6,18,19]. No Raman peaks of the secondary phases were observed in the spectra. The frequency and full width at half maximum (FWHM) of the main A_1 mode versus the chemical composition of the solid solution are plotted in the inset graph of Fig. 3. A significant broadening of the A_1 mode for powder with the value of $x = 0.4$ is observed. This could be attributed to the existence of disorder effects in the mixed crystals, related to the structural transition from kesterite to the stannite structure.

3.2. Optical properties of CCdZTS solid solutions

Normalized PL spectra of CCdZTS solid solutions with different Cd contents measured at $T = 10 \text{ K}$ are presented in Fig. 4. Low-temperature PL spectra are consisted of one broad asymmetric PL band at 1.3 eV in $\text{Cu}_2\text{ZnSnS}_4$ and at 1.1 eV in $\text{Cu}_2\text{CdSnS}_4$. PL bands with such an asymmetric shape are often observed in multinary compounds that contain large concentrations of charged defects [18]. A shift of the PL band of CCdZTS monograin powders towards lower energies with increasing Cd content is observed in the region $0 \leq x < 0.4$. The further increase in Cd concentration did not change the PL band position significantly.

The QE data allow to estimate the bandgap of absorber material using the following equation: $QE \approx A(E - E_g^*)^{1/2} / E$, where E_g^* is an effective band gap energy and constant A includes all parameters that do not depend on E [20]. The normalized QE spectra of MGL solar cells based on $\text{Cu}_{1.85}(\text{Cd}_x\text{Zn}_{1-x})_{1.1}\text{SnS}_{4.1}$ solid solutions show a shift of the absorption edge to longer wavelength in the region $0 \leq x < 0.4$ (Fig. 5). E_g^* values calculated from QE measurements for $\text{Cu}_{1.85}\text{ZnSnS}_{4.1}$ and $\text{Cu}_{1.85}\text{CdSnS}_{4.1}$ devices are 1.55 eV and 1.37 eV, respectively. The linear change of effective bandgap from 1.55 eV to 1.41 eV was observed in the region $0 \leq x < 0.4$ and subsequent increasing of Cd content in

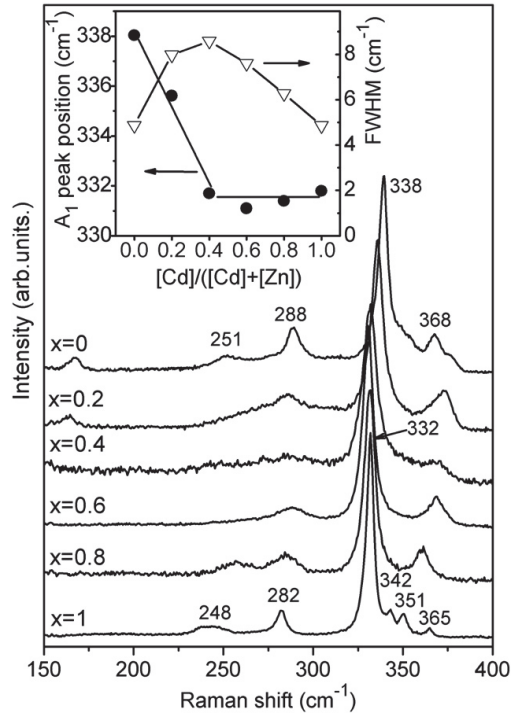


Fig. 3. The Raman spectra of $\text{Cu}_{1.85}(\text{Cd}_x\text{Zn}_{1-x})_{1.1}\text{SnS}_{4.1}$ ($0 \leq x \leq 1$) monograin powders. Inset graph: frequency and FWHM of the A_1 Raman mode versus Cd content in $\text{Cu}_{1.85}(\text{Cd}_x\text{Zn}_{1-x})_{1.1}\text{SnS}_{4.1}$.

absorber material changed bandgap value only up to 1.37 eV (inset graph in Fig. 5).

4. Conclusion

In summary, stable solid solutions of CCdZTS ($x = 0.2, 0.4, 0.6$ and 0.8) compounds were obtained by isothermal recrystallization

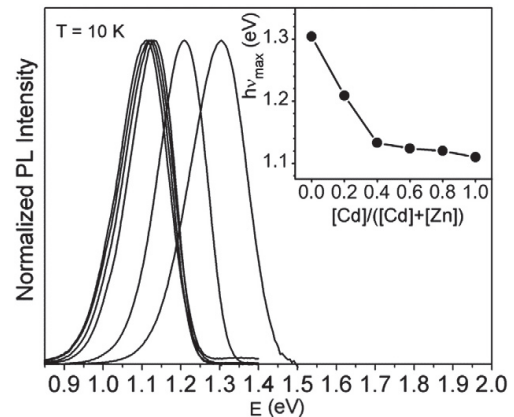


Fig. 4. Normalized PL spectra of $\text{Cu}_{1.85}(\text{Cd}_x\text{Zn}_{1-x})_{1.1}\text{SnS}_{4.1}$ ($0 \leq x \leq 1$) monograin powders.

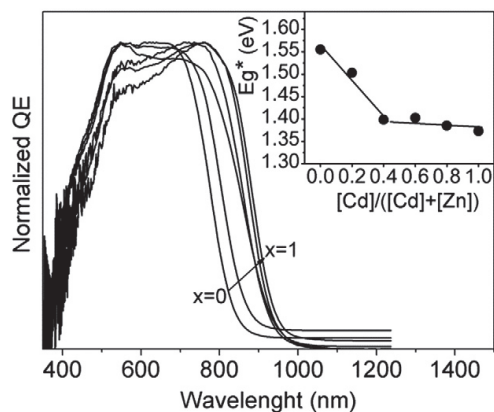


Fig. 5. The normalized QE spectra of monograin layer solar cells based on $\text{Cu}_{1.85}(\text{Cd}_x\text{Zn}_{1-x})_{1.1}\text{SnS}_{4.1}$ solid solutions and the band gap energy values of $\text{Cu}_{1.85}(\text{Cd}_x\text{Zn}_{1-x})_{1.1}\text{SnS}_{4.1}$ solid solutions determined from QE measurements.

of monograin powders. The analysis of CCdZTS solid solutions with different compositions allowed to determine the dependence of the Raman modes, PL band position and band gap energy of absorber on the composition of the solid solutions. The obtained results showed that incorporation of Cd into the CZTS decreased linearly the values of band gap from 1.55 to 1.41 eV, A_1 Raman mode from 338 to 332 cm^{-1} and PL band position from 1.3 to 1.1 eV in the region $0 \leq x < 0.4$. Subsequent increasing of Cd concentration x did not change these values significantly. Structural studies indicated that the phase transition from kesterite to stannite occurs around $x = 0.4$.

Our results suggest that CCdZTS, with the x value around 0.4, has optimal bandgap of 1.41 eV and could be a suitable material for absorber layer in single junction solar cells.

Acknowledgments

This work was supported by the Estonian Science Foundation grants ETF9346, ETF9425 and ETF8964 by institutional research funding IUT (IUT19-28) of the Estonian Ministry of Education and Research, Projects TK117T, AR10128 and AR12128.

References

- [1] F. Lopez-Vergara, A. Galdamez, V. Manriquez, P. Barahona, O. Pena, $\text{Cu}_2\text{Mn}_{1-x}\text{Co}_x\text{SnS}_4$: novel kesterite type solid solutions, *J. Solid State Chem.* 198 (2013) 386.
- [2] D.B. Mitzi, O. Gunawan, T.K. Todorov, K. Wang, S. Guha, The path towards a high-performance solution-processed kesterite solar cell, *Sol. Energy Mater. Sol. Cells* 95 (2011) 1421.
- [3] T.K. Todorov, J. Tang, S. Bag, O. Gunawan, T. Gokmen, Y. Zhu, D.B. Mitzi, Beyond 11 % efficiency: characteristics of state-of-the-art $\text{Cu}_2\text{ZnSn}(\text{S}, \text{Se})_4$ solar cells, *Adv. Energy Mater.* 3 (2013) 34.
- [4] W. Wang, M.T. Winkler, O. Gunawan, T. Gokmen, T.K. Todorov, Y. Zhu, D.B. Mitzi, Device characteristics of CZTSSe thin-film solar cells with 12.6 % efficiency, *Adv. Energy Mater.* (2013) 1.
- [5] S. Bag, O. Gunawan, T. Gokmen, Y. Zhu, D.B. Mitzi, Hydrazine-processed Ge-substituted CZTSSe solar cells, *Chem. Mater.* 24 (2012) 4588.
- [6] K. Timmo, M. Kauk-Kuusik, M. Altsaar, J. Raudoja, T. Raadik, M. Grossberg, T. Varema, M. Pilvet, I. Leinemann, O. Volobujeva, E. Mellikov, Novel $\text{Cu}_2\text{CdSnS}_4$ and $\text{Cu}_2\text{ZnGeSe}_4$ absorber materials for monograin layer solar cell applications, Proceedings of the 28th European Photovoltaic Solar Energy Conference and Exhibition, Paris, France, September 30–October 04 2013, p. 2385.
- [7] K. Timmo, M. Altsaar, J. Raudoja, K. Muska, M. Pilvet, M. Kauk, T. Varema, M. Danilson, O. Volobujeva, E. Mellikov, Sulfur-containing $\text{Cu}_2\text{ZnSnSe}_4$ monograin powders for solar cells, *Sol. Energy Mater. Sol. Cells* 94 (2010) 1889.
- [8] Y. Cao, Y. Xiao, J.-Y. Jung, H.-D. Um, S.-W. Jee, H.M. Choi, J.H. Bang, J.-H. Lee, Highly electrocatalytic $\text{Cu}_2\text{ZnSn}(\text{S}_{1-x}\text{Se}_x)_4$ counter electrodes for quantum-dot-sensitized solar cells, *Appl. Mater. Interfaces* 5 (2013) 479.
- [9] Y.-P. Wang, S. Levchenko, D.O. Dumcenco, Y.-S. Huang, C.-H. Ho, K.-K. Tiong, Composition dependent band gaps of single crystal $\text{Cu}_2\text{ZnSn}(\text{S}, \text{Se}_{1-x})_4$ solid solutions, *Solid State Phenom.* 194 (2013) 139.
- [10] Z.-Y. Xiao, Y.-F. Li, B. Yao, R. Deng, Z.-H. Ding, T. Wu, C. Yang, C.-R. Li, Z.-Y. Dong, L. Liu, L.-G. Zhang, H.-F. Zhao, Bandgap engineering of $\text{Cu}_2\text{Cd}_x\text{Zn}_{1-x}\text{SnS}_4$ alloy for photovoltaic application: a complementary experimental and first-principles study, *J. Appl. Phys.* 114 (2013) 183506.
- [11] S. Schorr, H.-J. Hoebler, M. Tovar, A neutron diffraction study of the stannite-kesterite solid solution series, *Eur. J. Mineral.* 19 (2007) 65.
- [12] L.V. Piskach, O.V. Parasyuk, I.D. Oleksyuk, The phase equilibria in the quasi-ternary $\text{Cu}_2\text{S}-\text{CdS}-\text{SnS}_2$ system, *J. Alloys Compd.* 279–2 (1998) 142.
- [13] R. Boistelle, J.P. Astier, Crystallization mechanisms in solution, *J. Cryst. Growth* 90 (1–3) (July 2 1988) 14.
- [14] K. Muska, M. Kauk, M. Grossberg, M. Altsaar, J. Raudoja, O. Volobujeva, Influence of compositional deviations on the properties of $\text{Cu}_2\text{ZnSnSe}_4$ monograin powders, *Energy Procedia* 10 (2011) 203.
- [15] K. Timmo, M. Altsaar, J. Raudoja, M. Grossberg, M. Danilson, O. Volobujeva, E. Mellikov, Chemical etching of $\text{Cu}_2\text{ZnSnS}(\text{S}, \text{Se})_4$ monograin powder, Proceedings of the 35th IEEE Photovoltaic Specialists Conference, June 20–25, Honolulu, Hawaii, 2010, p. 001982.
- [16] M. Kauk, K. Muska, M. Altsaar, J. Raudoja, M. Pilvet, T. Varema, K. Timmo, O. Volobujeva, Effects of sulphur and tin disulphide vapour treatments of $\text{Cu}_2\text{ZnSn}(\text{S}, \text{Se})_4$ absorber materials for monograin solar cells, *Energy Procedia* 10 (2011) 197.
- [17] T. Maeda, S. Nakamura, T. Wada, First-principles study on Cd doping in $\text{Cu}_2\text{ZnSnS}_4$ and $\text{Cu}_2\text{ZnSnSe}_4$, *Jpn. J. Appl. Phys.* 51 (2012) (10NC11-1-10NC-6).
- [18] M. Grossberg, J. Krustok, J. Raudoja, K. Timmo, M. Altsaar, T. Raadik, Photoluminescence and Raman study of $\text{Cu}_2\text{ZnSn}(\text{S}, \text{Se}_{1-x})_4$ monograin powders for photovoltaic applications, *Thin Solid Films* 519 (2011) 7403.
- [19] X. Fontané, V. Izquierdo-Roca, E. Saucedo, S. Schorr, V.O. Yuhymchuk, M.Y. Valakh, A. Pérez-Rodríguez, J.R. Morante, Vibrational properties of stannite and kesterite type compounds: Raman scattering analysis of $\text{Cu}_2(\text{Fe}, \text{Zn})\text{SnS}_4$, *J. Alloys Compd.* 539 (2012) 190.
- [20] J. Krustok, R. Josepson, T. Raadik, M. Danilson, Potential fluctuations in $\text{Cu}_2\text{ZnSnSe}_4$ solar cells studied by temperature dependence of quantum efficiency curves, *Physica B* 405 (2010) 3186.

PAPER II

K. Timmo, M. Kauk-Kuusik, **M. Pilvet**, T. Raadik, M. Altosaar, M. Danilson, M. Grossberg, J. Raudoja, K. Ernits, Influence of order-disorder in $\text{Cu}_2\text{ZnSnS}_4$ powders on the performance of monograin layer solar cells, *Thin Solid Films* 633 (2017) 122–126.



Influence of order-disorder in $\text{Cu}_2\text{ZnSnS}_4$ powders on the performance of monograin layer solar cells



K. Timmo^{a,*}, M. Kauk-Kuusik^a, M. Pilvet^a, T. Raadik^a, M. Altosaar^a, M. Danilson^a, M. Grossberg^a, J. Raudoja^a, K. Ernits^b

^a Department of Materials Science, Tallinn University of Technology, Ehitajate tee 5, 19086 Tallinn, Estonia

^b Crystalsol OÜ, Akadeemia tee 15a, 12618 Tallinn, Estonia

ARTICLE INFO

Article history:

Received 6 May 2016

Received in revised form 7 October 2016

Accepted 7 October 2016

Available online 8 October 2016

Keywords:

Copper zinc tin selenide

Kesterite

Order-disorder transition

Solar cells

Crystalline powder

ABSTRACT

In this study the influence of low-temperature structural ordering in absorber material to the performance of $\text{Cu}_2\text{ZnSnS}_4$ (CZTS) monograin layer (MGL) solar cells was investigated. The shift of peak position in low temperature and room temperature photoluminescence measurements was used to estimate the Cu–Zn disorder level in CZTS monograin powders. The degree of Cu–Zn ordering was changed by using different cooling times after annealing CZTS powders in S atmosphere at 740 °C and by additional annealing at temperatures below critical temperature ($T_c \sim 260$ °C) for different time periods. Current–voltage measurements revealed that the low-temperature thermal treatments resulting in increased ordering of CZTS absorber material had significant impact on the MGL solar cell characteristics, mostly, the values of open circuit voltage (V_{oc}) were increased. The highest V_{oc} of 784 mV was measured for the solar cell based on the powder that was cooled from 740 °C to room temperature for 5 min followed by annealing at 150 °C for 24 h. Optimal conditions for low-temperature annealing to improve CZTS MGL solar cells' performance were found to be 4 h at 150 °C. These improvements resulted in CZTS MGL solar cell power conversion efficiency of 9.1% (active area).

© 2016 Elsevier B.V. All rights reserved.

1. Introduction

Kesterite $\text{Cu}_2\text{ZnSn}(\text{S,Se})_4$ (CZTSSe) is a candidate for absorber material for solar cells due to its non-toxic, earth-abundant elemental constituents and suitable optoelectronic properties. Different methods are used for the growth of $\text{Cu}_2\text{ZnSn}(\text{S,Se})_4$ absorber materials and remarkable progress has been made in solar cell efficiency from 1988, when Ito and Nakazawa for the first time recorded the photovoltaic effect in the hetero-diode consisting of a cadmium-tin-oxide transparent conductive film and a $\text{Cu}_2\text{ZnSnS}_4$ (CZTS) thin film [1]. In 2013, the IBM group reported 12.6% efficiency of a $\text{Cu}_2\text{ZnSn}(\text{S,Se})_4$ solar cell produced by hydrazine-based solution processing [2]. One prerequisite for obtaining high-efficiency solar cells is the control over the defect structure of the absorber material including defect clusters, Cu–Zn disorder and the presence of secondary phases [3–8] influencing the bulk and interface recombination of the photogenerated charge carriers and resulting in lower open circuit voltage (V_{oc}) than could be expected from the given band gap of CZTS (about 1.5 eV [9]). More precisely, low V_{oc} values can be caused by bulk recombination related to deep defects, interface recombination, recombination of the charge carriers in the potential wells caused by the band gap and/or potential fluctuations

[3,4,6,10]. By first-principle calculations the band gap energy difference between ordered and disordered kesterite phases was predicted to be around 0.1 eV in CZTS [8]. From photoluminescence (PL) studies [11] it was proposed that the difference between PL band energies of ordered and disordered structures is about 80 meV, the latter being smaller. Neutron diffraction measurements in [12] showed that the degree of disorder depends on cooling rate after sample synthesis. Rapid cooling gives the highest degree of disorder, while slow cooling tends to give more ordered CZTS. Degree of Cu–Zn disordering can be changed by using different cooling regimes after high temperature treatments or low-temperature post-annealing at temperature below the critical temperature ($T_c \sim 260$ °C) [13,14].

Currently, there are few experimental results about the influence of the degree of order-disorder to the kesterite solar cell parameters [7,15,16]. It has been shown that increased Cu–Zn ordering improves $\text{Cu}_2\text{ZnSnSe}_4$ [7] and $\text{Cu}_2\text{ZnSn}(\text{S,Se})_4$ [15,16] V_{oc} , however the V_{oc} deficit considering the increasing bandgap of the material due to improved ordering is still remarkable.

In this study $\text{Cu}_2\text{ZnSnS}_4$ monograin layer (MGL) solar cells were performed and an improved ordering of the crystal lattice due to developed low temperature thermal treatments allowed us to obtain record V_{oc} of 784 mV for CZTS solar cells. We investigated the influence of different cooling regimes after high-temperature (HT) treatment of CZTS powder in S vapor to the performance of MGL solar cells. In the first

* Corresponding author.

E-mail address: kristi.timmo@ttu.ee (K. Timmo).

experimental series the powders were cooled to room-temperature (RT) by using different cooling rates and in the second series, the powders were annealed additionally at low-temperatures (LT) for different time periods.

2. Experimental

The investigated CZTS monograin powders were synthesized under Cu-poor and Zn-rich conditions from elemental and binary precursors in molten KI as flux in sealed quartz ampoules at 740 °C. The materials were cooled down naturally to RT. Detailed procedure about monograin powder synthesis is described elsewhere [17].

Two as-grown CZTS monograin powder batches with slightly different compositions were divided into small portions, annealed in the sealed ampoules in two-temperature-zone furnace at 740 °C in sulphur atmosphere of 1.33×10^5 Pa pressure for 1 h and then cooled to RT with different rates. The bulk compositions of as-grown CZTS monograin powders determined by energy dispersive X-ray spectroscopy (EDX) were $[\text{Cu}]/([\text{Zn}] + [\text{Sn}]) = 0.91$ and $[\text{Zn}]/[\text{Sn}] = 1.06$ for Series I and $[\text{Cu}]/([\text{Zn}] + [\text{Sn}]) = 0.96$ and $[\text{Zn}]/[\text{Sn}] = 1.02$ for Series II.

In the first experimental series 4 different cooling regimes were applied: the fastest cooling rate was performed by quenching the ampoule with powder into cold water to freeze the HT thermal equilibrium of lattice defects, corresponding to the state of maximum Cu-Zn disorder [13, 18]. The other powders were cooled from 740 °C to RT for 5 (cooled naturally in air), 15 and 510 min (natural cooling of the furnace) with the aim to obtain various degree of ordering. In the Series I, all powders had parallel samples, which were subsequently annealed at 150 °C for 4 h, followed by natural cooling in air to RT.

In the second experimental series, HT treatment in S atmosphere followed by cooling powders from 740 °C to RT for 5 min and the second step was additional annealing at temperatures below T_c - at 100, 125, 150, 175, 200, 225 and 250 °C for different time periods from 5 min to 4 h. After LT-annealing, all powders were cooled naturally in air to RT. In addition, some samples were induced to attain highly ordered structure by annealing at 150 °C for 24–168 h.

After above described annealing procedures, the powders were used as absorber materials in MGL solar cells. The photoactive MGL was formed by embedding the CZTS grains halfway to thin epoxy layer. CdS buffer layer was deposited from chemical solution containing CdI_2 as Cd source, ammonia and thiourea as a sulphur precursor. Before CdS buffer layer deposition, RT KCN etching was used, as reported in our previous work [19]. The devices were completed by sputtering a two-layer ZnO film (i-ZnO and Al-doped ZnO) on the top of CdS layer. More detailed description of the preparation and structure of MGL solar cells can be found in [20]. The solar cells were characterized by measuring the current density versus voltage (J-V) characteristics by Keithley 2400 electrometer under standard test conditions (AM 1.5, 100 mW/cm²). The measurement error in V_{oc} values can be considered up to 10 mV. As the working area of the MGL solar cells is around 80% of the total area, the MGL solar cell efficiency values are re-calculated for active area (η_{active}). Spectral response measurements were performed using computer controlled SPM-2 prism monochromator. The generated photocurrent was detected at 0 V bias voltage at RT by using 250 W halogen lamp.

The microstructure and the bulk composition of CZTS powder crystals were analysed by high resolution scanning electron microscope Zeiss ULTRA 55 (20 keV) equipped with backscattered electron detector and by EDX Bruker Esprit 1.8 system. The measurement error for elemental analysis is about 0.5 at.%. For PL measurements, the samples were mounted in the closed-cycle He cryostat and cooled down to 10 K. The 441 nm laser line was used for PL excitation and the spectra were detected by using InGaAs detector. The measurement error in the values of the PL peak positions is 0.005 eV. Room-temperature photoluminescence (RT-PL) and Raman spectra were measured by Horiba LabRam 800HR spectrometer using 532 nm laser for excitation.

3. Compositional analysis

Compositional analysis by EDX were made from polished cross-section of individual crystals (Fig. 1) of CZTS powders cooled from 740 °C to RT by using different cooling rates and crystals that were annealed additionally at 150 °C for 4 h after different cooling processes. For each of the cooling conditions the analysis was performed on at least 8 different polished crystals. The average chemical compositions of CZTS powders are presented in Table 1. It can be seen that the bulk composition of CZTS monograin powders did not change significantly by increasing cooling time after post-treatment. Furthermore, no changes were seen in the chemical composition of the powders annealed additionally at 150 °C for 4 h. Only ZnS secondary phase as separate crystals in the powder was detected and it is usually found to be present in CZTS monograin powders with Zn-rich composition (see Fig. 1).

4. Photoluminescence results

Previously, the Cu-Zn disordering has been probed by Raman spectroscopy [14,21,22] and by PL measurements [6,13]. Scragg et al. measured the 785-nm Raman spectra of nominally ordered and disordered CZTS films and calculated the ratio of $Q = I(m_{2A}) / I(m_{3A})$, where $I(m_{2A})$ and $I(m_{3A})$ are the Raman peak intensities for the A modes at 288 and 304 cm⁻¹, showing that there exists the correlation: the larger the Q value, the more ordered is the structure [14]. In addition, the full width half maximum (FWHM) of the dominating A₁ Raman peak of CZTS at 338 cm⁻¹ is also found to be in correlation with the degree of Cu-Zn ordering, the FWHM being smaller for more ordered material [13,14]. Unfortunately, Raman studies on our CZTS monograin powders have shown that different crystal planes show different intensity of the Raman peaks used for calculating Q values, therefore we have used the FWHM of the A₁ mode to evaluate the degree of ordering. In present study, the values of 6.5 cm⁻¹ and 3.6 cm⁻¹ of FWHM of A₁ Raman peak were found for the most disordered and ordered material, respectively (inset in Fig. 2).

Scragg et al. also showed that there is remarkable correlation between the RT-PL peak energy and the order parameter S in CZTS. In the most ordered sample (S ~ 0.8), the RT-PL peak energy reaches 1.43 eV [6]. In our previous study we have shown correlation in PL peak energies (T = 10 K) and degree of Cu-Zn ordering [13]. PL and RT-PL are therefore used to estimate the degree of Cu-Zn ordering in studied CZTS monograin powders.

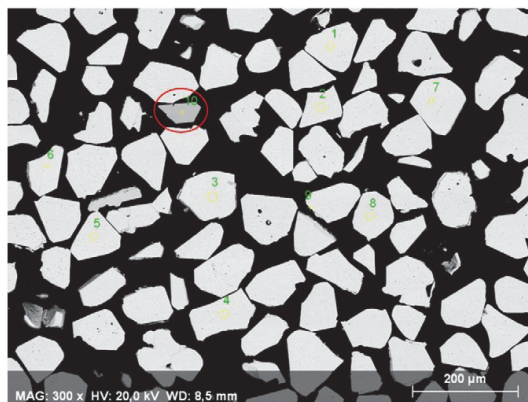


Fig. 1. Scanning electron microscope image of polished cross-section of individual crystals of CZTS powder. The highlighted red circle indicates darker gray area, signifying secondary phase of ZnS.

Table 1

Chemical composition and PL band position of CZTS powders cooled from 740 °C to RT after S-treatment by using different cooling times and powders that were additionally annealed at 150 °C for 4 h (low-temperature annealing - LTA) after different cooling processes and corresponding values of V_{oc} for solar cells based on these powders.

	[Cu]/[Zn] + [Sn]	[Zn]/[Sn]	[S]/[Met]	V_{oc} (mV)	PL_{max} (eV)
Quenching	0.91	1.05	1.00	582	1.21
Quenching + LTA	0.92	1.07	1.00	613	1.31
5 min to RT	0.92	1.07	1.00	685	1.26
5 min to RT + LTA	0.91	1.07	1.00	759	1.34
15 min to RT	0.92	1.06	1.00	724	1.29
15 min to RT + LTA	0.92	1.06	1.00	748	1.35
LTA					
510 min to RT	0.91	1.06	1.00	648	1.35
510 min to RT + LTA	0.92	1.07	1.00	691	1.35

In the experimental Series I, the PL studies showed that slower cooling of CZTS monograin powders after HT treatment shifted the typical broad asymmetric PL band position from 1.21 eV to 1.35 eV (~140 meV) (Fig. 2). The additional annealing at 150 °C for 4 h after different cooling processes shifts the PL band position to higher energy side giving hint to the further increase in ordering degree (the PL band positions are listed in Table 1). The shift of the PL band position of the slowest cooled powder by additional LT-annealing is only 5 meV indicating that maximum ordering is already reached with the first cooling step. The behavior of the PL bands with increased Cu-Zn ordering is in correspondence with our previous PL study of CZTS with different cooling regimes [13], where it was shown that the shift of the PL bands is caused by two processes – improved Cu-Zn ordering of the crystals leading to increased bandgap energy by about 100 meV and change in recombination type from band to tail to band to impurity type, the latter involving deep acceptor defect with the ionization energy of about 200 meV.

Although the PL band position of the slowest cooled powder indicates to the most ordered material, interestingly the value of V_{oc} for corresponding CZTS monograin layer solar cell is not the highest (Table 1). The value of V_{oc} increases from 582 mV to 724 mV by increasing the time of cooling up to 15 min from 740 °C to RT, but further increase of the cooling time results in lower values of V_{oc} (648 mV) for the corresponding solar cell. This could be explained by the change in the radiative recombination mechanism since in the slowest cooled powder the

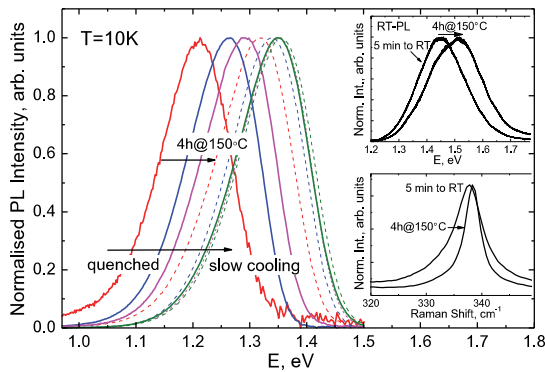


Fig. 2. PL spectra of CZTS monograins with different cooling regimes (data in Table 1) are shown by solid lines and the parallel samples, subsequently annealed at 150 °C for 4 h, are shown by dashed lines with the same colors. The shift in the RT-PL band position and in the FWHM of the A_1 Raman peak of the best performing CZTS monograin powder due to the LT-annealing is shown in the inset graphs.

deep trap (~200 meV) related recombination dominates and reduces the positive effect of the band gap increase to the V_{oc} in the most ordered material. Therefore we can conclude that the change in the defect structure of CZTS monograins accompanying the improved Cu-Zn ordering is most probably leading to the change in Fermi level position determining the V_{oc} value. This is in agreement with the results of Bourdais et al. [16], showing that the bandgap changes induced by the Cu-Zn disorder are not fully responsible for the V_{oc} deficit in the kesterite solar cells. It has to be stated here that beside changes in the bulk, the presence of secondary phases and also compositional changes in the near surface layer induced by very slow cooling after sulphur treatment resulting in changed CZTS/CdS interface properties can be responsible for the decrease in the solar cell parameters, including V_{oc} . Since ZnS was found to be present in all our samples, we can exclude its influence to the changes in PL spectra and solar cell parameters. The studies of junction formation between ordered CZTS and buffer layer are a subject for further studies.

As a result of the experimental Series I, the best performing solar cell is based on the powder that was cooled from 740 °C to RT for 5 min (reference sample 1 in Fig. 3), the corresponding J-V characteristic is shown in Fig. 4 (black curve). The same cooling regime was used in the experimental Series II for second powder (reference sample 2 in Fig. 3), where the powders were additionally annealed at different temperatures from 100 to 250 °C for different time periods.

PL and Raman spectra were measured for the powders annealed at 150 °C for 4 h. PL peak positions and corresponding values of V_{oc} are shown in Fig. 5 as a function of LT-annealing temperature. The behavior of PL band position and the corresponding V_{oc} value (see Fig. 5) are in a good correlation. There is a continuous shift of PL band maxima by 100 meV from 1.25 eV to 1.35 eV accompanied by the decrease in FWHM of the A_1 Raman peak with increasing temperature of LT-annealing from 100 to 175 °C. Further increase in LT-annealing temperature resulted in PL band positions at lower energy values and in increase in the FWHM of the A_1 Raman peak indicating increasing disordering. Again, the same trend was observed in the RT-PL spectra, where the band-band emission is detected. We can conclude that the highest degree of ordering in CZTS has been gained by annealing materials at temperatures between 150 and 175 °C.

5. Solar cell characterization

The values of V_{oc} of CZTS MGL solar cells in dependence of LT-annealing at temperatures from 100 °C to 250 °C for different time periods are

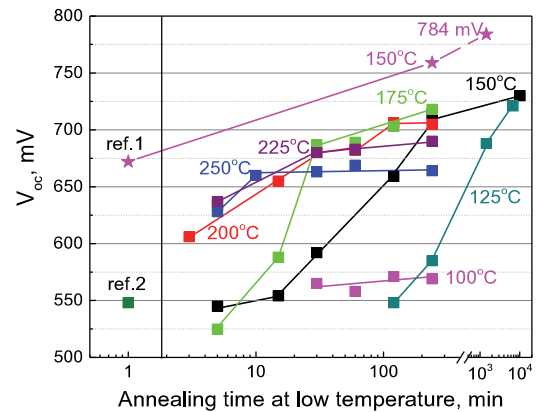


Fig. 3. Evolution of V_{oc} of CZTS MGL solar cells for Series II (squares) by additional annealing at different temperatures in dependence of time. Improvement of V_{oc} for reference cell 1 (from Series I) by additional annealing at 150 °C for 4 and 24 h is shown by stars.

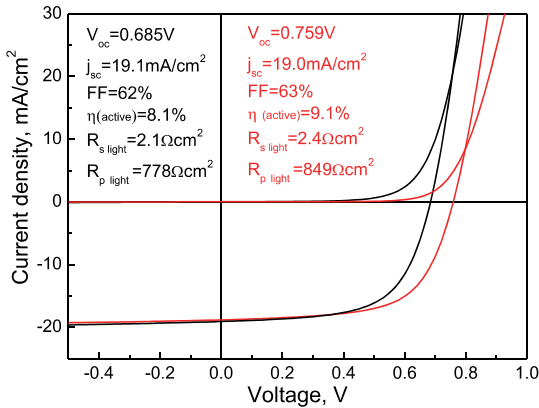


Fig. 4. The J-V curves before (black) and after (red) annealing powders at 150 °C for 4 h.

presented in Fig. 3. LT-annealing at 150 °C and 175 °C for 4 h increased the values of V_{oc} from 548 mV (reference sample 2) up to 714 mV and 718 mV, respectively. Annealing at temperatures higher than 175 °C (for example at 200 °C) improves the values of V_{oc} to the level, which corresponds to the maximum possible value of ordering degree at this temperature, and is constant thereafter. LT-annealing at temperatures lower than 150 °C will take longer time to reach the same level of V_{oc} , for example the annealing at 125 °C for 5 days is equal to the annealing at 175 °C for 4 h. Considering all solar cell output parameters, the optimal conditions for LT-annealing to improve monograin layer solar cells performance was found to be 4 h at 150 °C, although the highest V_{oc} value of 784 mV was gained by annealing the powder at 150 °C for 24 h (presented in Fig. 3 by stars).

The optimal LT-annealing conditions were also applied to the powder of reference cell 1, the corresponding J-V curve is shown in Fig. 4. The LT-annealing increased V_{oc} value by 74 mV giving more than 10% higher efficiency ($\eta_{active} = 9.1\%$) compared to the reference cell ($\eta_{active} = 8.1\%$).

The external quantum efficiency (EQE) of these solar cells was measured as a function of the wavelength of the incident light at room temperature (see Fig. 6). From the linear segment of the low-energy side of the construction $(E^*QE)^2$ vs. E curves the effective band gap energy E_g^* can be evaluated [23]. The E_g^* values of CZTS monograin powders before and after annealing at 150 °C for 4 h are 1.53 eV and 1.55 eV,

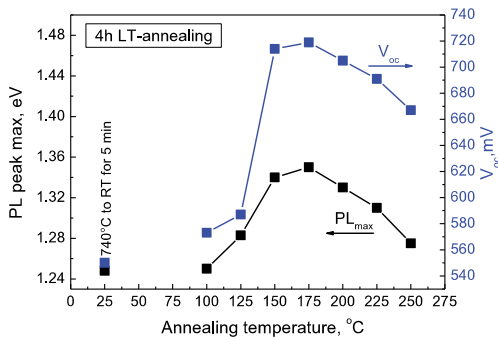


Fig. 5. PL peak positions of powders LT-annealed at different temperatures for 4 h and V_{oc} values of corresponding MGL solar cells.

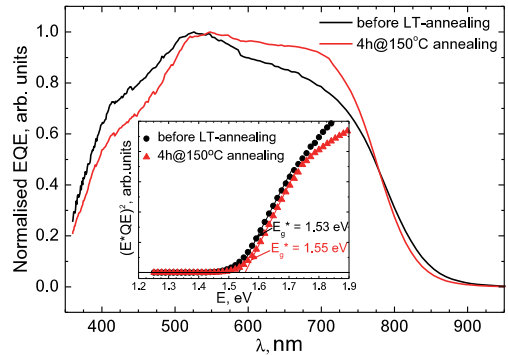


Fig. 6. EQE spectra of MGL solar cell devices based on powders with different cooling regimes: before LT-annealing (black) and after annealing powder at 150 °C for 4 h (red). The inset graph shows the E_g^* determined from EQE data.

respectively (see inset graph in Fig. 6), showing the band gap increase with improved ordering. This is in correspondence with the shift in band to band peak position in RT-PL spectra (1.47 eV and 1.53 eV, respectively), however the shift in E_g^* value is smaller. This could be explained by the fact that E_g^* is connected to the change in the absorption, but RT-PL band position is determined by the recombination of the photogenerated charge carriers.

6. Conclusion

The influence of Cu-Zn ordering level in Cu_2ZnSnS_4 monograin powders to the performance of CZTS based MGL solar cells was studied. The ordering level was changed by different cooling and LT-annealing regimes and estimated by PL and Raman spectroscopy. It was shown that improved ordering increases the band gap energy of the CZTS material resulting in increased value of V_{oc} of the corresponding MGL solar cells. The optimal conditions for LT-annealing to improve monograin layer solar cells' performance were found to be 4 h at 150 °C after cooling from 740 °C to RT for 5 min, resulting in CZTS MGL solar cell efficiency of 9.1% (active area). The highest V_{oc} value 784 mV was obtained by annealing the powder at 150 °C for 24 h.

It was found that change in Cu-Zn ordering is accompanied with change in the radiative recombination mechanism from band to tail to deep trap related recombination in most ordered material reducing the positive effect to the CZTS solar cell performance. Also the compositional changes in the near surface layer induced by very slow cooling after sulphur treatment could modify the interface properties of CZTS/CdS that can be responsible for the decrease in the solar cell parameters, including V_{oc} . The studies of junction formation between ordered CZTS and buffer layer are a subject for further studies.

Acknowledgements

This work was supported by the Estonian Science Foundation grants ETF9346, ETF9425, ETF9369 and by institutional research funding IUT (IUT19-28) of the Estonian Ministry of Education and Research, and by the European Union through the European Regional Development Fund, Project TK141, and by the FP7 Project CHEETAH Grant Agreement No. 609788.

References

- [1] K. Ito, T. Nakazawa, Electrical and optical properties of stannite-type quaternary semiconductor thin films, *Jpn. J. Appl. Phys.* 27 (1988) 2094–2097.

- [2] W. Wang, M.T. Winkler, O. Gunawan, T. Gokmen, T.K. Todorov, Y. Zhu, D.B. Mitzi, Device characteristics of CZTSSe thin-film solar cells with 12.6% efficiency, *Adv. Energy Mater.* 4 (2014) 1301465.
- [3] J.J.S. Scragg, T. Kubart, J.T. Wätjen, T. Ericson, M.K. Linnarsson, C. Platzer-Björkman, Effects of back contact instability on $\text{Cu}_2\text{ZnSnS}_4$ devices and processes, *Chem. Mater.* 25 (2013) 3162–3171.
- [4] A. Redinger, D.M. Berg, P.J. Dale, S. Siebentritt, The consequences of kesterite equilibria for efficient solar cells, *J. Am. Chem. Soc.* 133 (2011) 3320–3323.
- [5] D. Huang, C. Persson, Band gap change induced by defect complexes in $\text{Cu}_2\text{ZnSnS}_4$, *Thin Solid Films* 535 (2013) 265–269.
- [6] J.J.S. Scragg, J.K. Larsen, M. Kumar, C. Persson, J. Sendler, S. Siebentritt, C. Platzer-Björkman, Cu–Zn disorder and band gap fluctuations in $\text{Cu}_2\text{ZnSn}(\text{S,Se})_4$: theoretical and experimental investigations, *Phys. Status Solidi B* 253 (2016) 247–254.
- [7] G. Rey, T.P. Weiss, J. Sendler, A. Finger, S. Spindler, F. Werner, M. Melchiorre, M. Håla, M. Guennou, S. Siebentritt, Ordering kesterite improves solar cells: a low temperature post-deposition annealing study, *Sol. Energy Mater. Sol. Cells* 151 (2016) 131–138.
- [8] S. Chen, X.G. Gong, A. Walsh, S.H. Wei, Crystal and electronic band structure of $\text{Cu}_2\text{ZnSnX}_4$ ($X = \text{S}$ and Se) photovoltaic absorbers: first-principles insights, *Appl. Phys. Lett.* 94 (2009) 041903.
- [9] T. Tanaka, T. Nagatomo, D. Kawasaki, M. Nishio, Q. Guo, A. Wakahara, A. Yoshida, H. Ogawa, Preparation of $\text{Cu}_2\text{ZnSnS}_4$ thin films by hybrid sputtering, *J. Phys. Chem. Solids* 66 (2005) 1978–1981.
- [10] M. Danilson, E. Kask, N. Pokharel, M. Grossberg, M. Kauk-Kuusik, T. Varema, J. Krustok, Temperature dependent current transport properties in $\text{Cu}_2\text{ZnSnS}_4$ solar cell, *Thin Solid Films* 582 (2015) 162–165.
- [11] M. Grossberg, J. Krustok, J. Raudoja, T. Raadik, The role of structural properties on deep defect states in $\text{Cu}_2\text{ZnSnS}_4$ studied by photoluminescence spectroscopy, *Appl. Phys. Lett.* 101 (2012) 102102.
- [12] S. Schorr, The crystal structure of kesterite type compounds: a neutron and X-ray diffraction study, *Sol. Energy Mater. Sol. Cells* 95 (2011) 1482–1488.
- [13] M. Grossberg, J. Krustok, T. Raadik, M. Kauk-Kuusik, J. Raudoja, Photoluminescence study of disordering in the cation sublattice of $\text{Cu}_2\text{ZnSnS}_4$, *Curr. Appl. Phys.* 14 (2014) 1424–1427.
- [14] J.J.S. Scragg, L. Choubrac, A. Lafond, T. Ericson, C. Platzer-Björkman, A low-temperature order-disorder transition in $\text{Cu}_2\text{ZnSnS}_4$ thin films, *Appl. Phys. Lett.* 104 (2014) 041911.
- [15] S. Bourdais, C. Chone, B. Delatouche, A. Jacob, G. Larramona, C. Moisan, A. Lafond, F. Donatini, G. Rey, S. Siebentritt, A. Walsh, G. Dennler, Is the Cu/Zn disorder the main culprit for the voltage deficit in kesterite solar cells? *Adv. Energy Mater.* 1502276 (2016).
- [16] C. Krämmer, C. Huber, T. Schnabel, C. Zimmermann, M. Lang, E. Ahlswede, H. Kalt, M. Hetterich, Order-disorder related band gap changes in $\text{Cu}_2\text{ZnSn}(\text{S,Se})_4$: impact on solar cell performance, Proc. 42nd IEEE Photovoltaic Specialist Conference (PVSC), 2015, <http://dx.doi.org/10.1109/PVSC.2015.7356096>.
- [17] M. Pilvet, M. Kauk-Kuusik, M. Altsaar, M. Grossberg, M. Danilson, K. Timmo, A. Mere, V. Mikli, Compositionally tunable structure and optical properties of $\text{Cu}_{1.85}(\text{Cd}_x\text{Zn}_{1-x})_{1.1}\text{SnS}_{4.1}$ ($0 \leq x \leq 1$) monograin powders, *Thin Solid Films* 582 (2015) 180.
- [18] L. Choubrac, M. Paris, A. Lafond, C. Guillot-Deudon, X. Rocquefelte, S. Jobic, Multinuclear (^{67}Zn , ^{119}Sn and ^{65}Cu) NMR spectroscopy—an ideal technique to probe the cationic ordering in $\text{Cu}_2\text{ZnSnS}_4$ photovoltaic materials, *Phys. Chem. Chem. Phys.* 15 (2013) 10722–10725.
- [19] M. Kauk-Kuusik, K. Timmo, M. Danilson, M. Altsaar, M. Grossberg, K. Ernits Applied, *Surf. Sci.* 357 (2015) 795–798.
- [20] E. Mellikov, M. Altsaar, M. Kauk-Kuusik, K. Timmo, D. Meissner, M. Grossberg, J. Krustok, O. Volobujeva, Growth of CZTS-based monograins and their application to membrane solar cells, in: K. Ito (Ed.), *Copper Zinc Tin Sulfide-Based Thin Film Solar Cells*, 2015, Wiley-VCH 2015, pp. 289–309.
- [21] G. Rey, A. Redinger, J. Sendler, T.P. Weiss, M. Thevenin, M. Guennou, B.E. Adib, S. Siebentritt, The band gap of $\text{Cu}_2\text{ZnSnSe}_4$: effect of order-disorder, *Appl. Phys. Lett.* 105 (2014) 112106.
- [22] M. Paris, L. Choubrac, A. Lafond, C. Guillot-Deudon, S. Jobic, Solid-state NMR and Raman spectroscopy to address the local structure of defects and the tricky issue of the Cu/Zn disorder in Cu-poor, Zn-rich CZTS materials, *Inorg. Chem.* 53 (2014) 8646–8653.
- [23] J. Krustok, R. Josepson, T. Raadik, M. Danilson, Potential fluctuations in $\text{Cu}_2\text{ZnSnSe}_4$ solar cells studied by temperature dependence of quantum efficiency curves, *Physica B* 405 (2010) 3186.

PAPER III

M. Pilvet, M. Kauk-Kuusik, M. Grossberg, T. Raadik, V. Mikli, R. Traksmäa, J. Raudoja, K. Timmo, J. Krustok, Modification of the optoelectronic properties of $\text{Cu}_2\text{CdSnS}_4$ through low-temperature annealing treatments, *Journal of Alloys and Compounds* 723 (2017) 820–825.



Modification of the optoelectronic properties of $\text{Cu}_2\text{CdSnS}_4$ through low-temperature annealing



M. Pilvet^{a,*}, M. Kauk-Kuusik^a, M. Grossberg^a, T. Raadik^a, V. Mikli^a, R. Traksmaa^b, J. Raudoja^a, K. Timmo^a, J. Krustok^{a,c}

^a Department of Materials and Environmental Technology, Tallinn University of Technology, Ehitajate tee 5, 19086, Tallinn, Estonia

^b Department of Mechanical and Industrial Engineering, Tallinn University of Technology, Ehitajate tee 5, 19086, Tallinn, Estonia

^c Division of Physics, Tallinn University of Technology, Ehitajate tee 5, 19086, Tallinn, Estonia

ARTICLE INFO

Article history:

Received 20 March 2017

Received in revised form

26 June 2017

Accepted 27 June 2017

Available online 30 June 2017

Keywords:

$\text{Cu}_2\text{CdSnS}_4$

Stannite

Polycrystalline powder

Photoluminescence

Raman scattering

Structural transition

ABSTRACT

In this study the experimental evidence of the existence of Cu–Cd disordering in $\text{Cu}_2\text{CdSnS}_4$ is presented. The influence of low-temperature annealing from 100 °C to 400 °C to the optical and structural properties of $\text{Cu}_2\text{CdSnS}_4$ polycrystalline powder was studied. Raman scattering and temperature dependent photoluminescence analysis were used to show that the degree of disordering can be reduced with the low-temperature annealing below the critical temperature. According to our study the critical temperature lies in the range from 200 °C to 250 °C. It was found that, the change in the degree of disordering in $\text{Cu}_2\text{CdSnS}_4$ is accompanied with the change in the radiative recombination channel related to different type of defect clusters.

© 2017 Elsevier B.V. All rights reserved.

1. Introduction

The $\text{I}_2\text{-II-IV-VI}_4$ quaternary compounds have attracted considerable interest as potential absorber materials in photovoltaic solar cells due to suitable energy band gaps, high absorption coefficient and earth abundant elements. Solar cells based on $\text{Cu}_2\text{ZnSnS}_4$ absorber have achieved the power conversion efficiency as high as 9.2% [1]. Because of the similar properties, $\text{Cu}_2\text{CdSnS}_4$ is also considered as possible photovoltaic material. Nitché et al. synthesized single crystal of $\text{Cu}_2\text{CdSnS}_4$ by iodine vapor transport and identified the crystal structure as a stannite type $\overline{142m}$ [2]. The compound has direct band gap $E_g \sim 1.4$ eV and an absorption coefficient larger than $1 \times 10^4 \text{ cm}^{-1}$ in the visible range of spectrum [3,4]. According to Shockley–Queisser efficiency limit for solar cells using a single p - n junction, the bandgap of $\text{Cu}_2\text{CdSnS}_4$ is closer to the ideal bandgap 1.34 eV [5] (using an AM1.5 solar spectrum) than $\text{Cu}_2\text{ZnSnS}_4$ ($E_g \sim 1.5$ eV) to reach higher device efficiency. $\text{Cu}_2\text{CdSnS}_4$ is an intrinsic p -type semiconductor and the p -type conductivity is attributed to Cu vacancies (V_{Cu}) [6] and/or copper in cadmium site

(Cu_{Cd}) acceptor defects [7].

Different methods have been studied to prepare $\text{Cu}_2\text{CdSnS}_4$ thin films, such as atom beam sputtering [3], solution method [8,9], co-sputtering deposition [10], spin coating [11,12], spray pyrolysis [13], sol-gel method [14], etc. We have used monograin powder technology and reported 2.7% efficiency for pure $\text{Cu}_2\text{CdSnS}_4$ solar cells [15]. Recently, we presented improved monograin layer solar cell efficiency of 4.2% at the PVSEC-26 conference. Despite of the suitable material properties the performance of $\text{Cu}_2\text{CdSnS}_4$ devices is still low. In $\text{Cu}_2\text{ZnSnS}_4$, the main limitation is due to low open circuit voltage (V_{oc}) as compared to the band gap energy value E_g . Recently, it has been shown in several studies [16–18] that the existence of Cu and Zn cation disorder in $\text{Cu}_2\text{ZnSnS}_4$ kesterite crystal structure could be one reason for the large open circuit voltage deficit. Main reason for poor performance of $\text{Cu}_2\text{CdSnS}_4$ solar cells is not yet clarified and more information about the optoelectronic properties is needed.

Similarly to $\text{Cu}_2\text{ZnSnS}_4$, density functional theory calculations in Ref. [7] indicate that the Cu–Cd cation disorder is also possible in $\text{Cu}_2\text{CdSnS}_4$. These first principles calculations have shown that the antisite defect Cu_{Cd} and self-compensated defect complex $\text{Cu}_{\text{Cd}} + \text{Cd}_{\text{Cu}}$ have very low formation energies, 0.59 eV/atom and

* Corresponding author.

E-mail address: Maris.pilvet@ttu.ee (M. Pilvet).

0.21 eV/atom, respectively. It was also shown that the random distribution of different defect pairs induces spatial band gap fluctuations, in the case of $\text{Cu}_{\text{Cd}} + \text{Cd}_{\text{Cu}}$ with the depth of about 0.1 eV. Another defect pair $2\text{Cu}_{\text{Cd}} + \text{Sn}_{\text{Cd}}$ has also low formation energy and in case of high concentrations it may result in very large band gap fluctuations of about 0.43–0.65 eV [7]. Since these unfavorable defect clusters have very low formation energies throughout all the compositional range of $\text{Cu}_2\text{CdSnS}_4$ [7] only thermal treatments could be used to modify the type of prevailing defect clusters. Among single native defects, the calculated acceptor level of Cu_{Cd} is 0.13 eV above the valence band edge. The donor level Cd_{Cu} is shallow (~ 0.05 eV below the conduction band edge), but Sn_{Cd} is a deep donor (~ 0.8 eV below the conduction band edge) that may act as electron-hole recombination center [7]. However, there is no experimental evidence of the Cu–Cd cation disorder in $\text{Cu}_2\text{CdSnS}_4$ available in literature. Moreover, there is lack of experimental data about the defects and related recombination mechanisms in $\text{Cu}_2\text{CdSnS}_4$. This information is of crucial importance for the development of efficient solar cells. In this study we used temperature dependent photoluminescence (PL) spectroscopy and Raman spectroscopy for exploring the optoelectronic properties of $\text{Cu}_2\text{CdSnS}_4$ polycrystalline powder that was modified by low-temperature heat-treatments.

2. Experimental

Polycrystalline powder of $\text{Cu}_2\text{CdSnS}_4$ was synthesized from elemental Cu (99.9%), Sn (99.9%), S (99.999%) and binary CdS (99.999%) powders by solid-state reaction in sealed evacuated quartz ampoules. For the synthesis, the starting materials were weighted in appropriate metal ratios (Cu: Sn: CdS = 1.85: 1: 1) with addition of sulfur and grounded in an agate mortar. The mixture of precursors was mounted into quartz ampoule, sealed under vacuum and placed in the chamber furnace. The temperature of the furnace was increased from room temperature (RT) to 200 °C with a rate of 10°/min. Sulfurization process of metal components was obtained by keeping the mixture at 200 °C for 24 h. Subsequently, the temperature of the furnace was increased to 900 °C with the rate of 12°/min and powder was homogenized at this temperature for 168 h. A complete homogenization was obtained by decreasing the temperature to 740 °C and keeping the powder at this temperature for 168 h. Finally, the powder was cooled from 740 °C to RT for 19 h.

It has been previously shown that the optoelectronic properties are strongly influenced by the structural disordering in kesterite-type materials [19,20] and the degree of disordering can be reduced by low-temperature annealing treatments below the critical temperature ($T_c \sim 260$ °C for $\text{Cu}_2\text{ZnSnS}_4$ and $T_c \sim 200$ °C for $\text{Cu}_2\text{ZnSnSe}_4$) [21,22]. In present study similar low-temperature annealing was applied on $\text{Cu}_2\text{CdSnS}_4$ polycrystalline powder to

identify the existence of structural disordering and to investigate the corresponding changes in the optical and structural properties of $\text{Cu}_2\text{CdSnS}_4$.

For this study, the synthesized polycrystalline powder was ground in an agate mortar and divided to equal amounts to the quartz ampoules, which were subsequently evacuated to 10^{-2} Torr vacuum and sealed with $\text{C}_3\text{H}_8/\text{O}_2$ flame. All sealed ampoules were heated up to 740 °C, annealed at this temperature for 1 h and then cooled by quenching into cold water. This annealing was done for healing out the mechanical damages on the powder particle surfaces caused by grinding process.

Subsequent low-temperature annealing study was done at following temperatures (T_{ann}): 100 °C, 150 °C, 175 °C, 200 °C, 225 °C, 250 °C, 300 °C, 350 °C and 400 °C for different time periods from 1 h to 2 weeks. After low-temperature annealing, the ampoules were quenched to cold water. Our experiments showed that the stable PL band position was reached by annealing at least 1 week at temperature below 200 °C, annealing at higher temperatures ($T_{\text{ann}} > 200$ °C) needed less time to reach stability. To be sure that the degree of ordering at a given temperature is reached, all powders used for the structural and optical studies were annealed for 1 week.

The structural investigation of the $\text{Cu}_2\text{CdSnS}_4$ polycrystalline powders was carried out by X-ray diffraction (XRD) and Raman spectroscopy. XRD patterns of the powders were recorded on a Bruker AXS X-ray diffractometer D5005 using Cu $K\alpha 1$ radiation ($\lambda = 1.5406$ Å) with variable slit V12. Obtained data was analyzed by ICDD PDF 2015 database (International Center for Diffraction Data). Raman spectra were recorded by using the Horiba's LabRam HR800 spectrometer equipped with a multichannel CCD detection system in the backscattering configuration using 532 nm laser line with spot size of 5 μm . The same equipment was used for room temperature photoluminescence (RT-PL) measurements.

The chemical composition of polycrystalline powder was analyzed by energy dispersive X-ray spectroscopy (EDX) using Bruker Esprit 1.8 system. The morphology of crystals was studied with the high-resolution scanning electron microscope (HR-SEM) Zeiss ULTRA 55. EDX mapping was carried out over the polycrystalline surface to investigate the elemental distribution and compositional uniformity over large area and different polycrystals. For low temperature PL measurements, the powder crystals were mounted in the closed-cycle He cryostat and cooled down to 10 K. The 441 nm He–Cd laser line was used for PL excitation and the spectra were detected by using InGaAs detector.

3. Results and discussion

3.1. Results of structural and compositional analysis

The elemental composition of synthesized $\text{Cu}_2\text{CdSnS}_4$

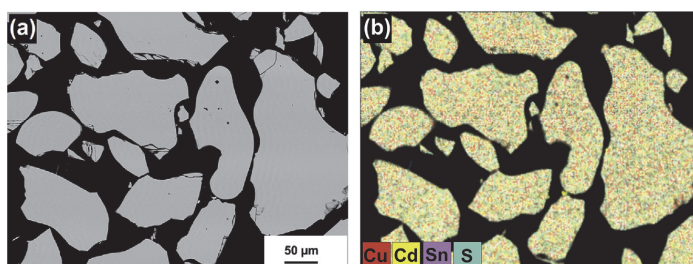


Fig. 1. (a) SEM image of the polished cross-section and (b) elemental mapping by EDX for Cu, Cd, Sn and S of individual $\text{Cu}_2\text{CdSnS}_4$ crystals.

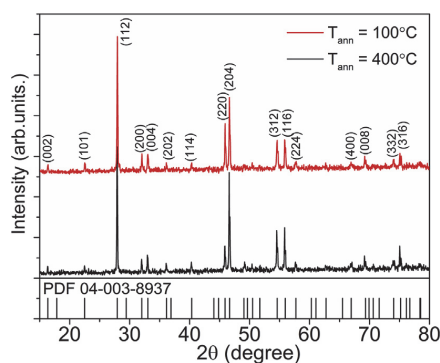


Fig. 2. XRD patterns of the $\text{Cu}_2\text{CdSnS}_4$ polycrystals annealed at 100 °C and 400 °C for 1 week.

polycrystalline powder was determined from polished cross-section of individual crystals. Fig. 1 presents SEM micrographs of (a) the polished cross-section and (b) the elemental mapping of Cu, Cd, Sn and S of individual $\text{Cu}_2\text{CdSnS}_4$ crystals. Fig. 1b reveals that the elements are homogeneously distributed in the bulk of the powder crystals.

The average bulk composition of synthesized $\text{Cu}_2\text{CdSnS}_4$ polycrystalline powder determined by EDX analysis is [Cu] = 24.5 at %, [Cd] = 13.0 at %, [Sn] = 12.5 at % and [S] = 50.0 at %. After different low-temperature annealing experiments, the composition of the powder did not change.

For structural studies, XRD and Raman analysis were performed. The XRD patterns of the $\text{Cu}_2\text{CdSnS}_4$ polycrystalline powders annealed at $T_{\text{ann}} = 100$ °C and $T_{\text{ann}} = 400$ °C, are presented in Fig. 2. The major diffraction peaks can be attributed to (112), (200), (004), (220), (204), (312) and (116) planes of stannite type $\text{Cu}_2\text{CdSnS}_4$ with the space group $I\bar{4}2m$ (ICDD PDF 04-003-8937). The *a*- and *c*-lattice constants were calculated from the XRD data and are $a = 5.592$ Å and $c = 10.857$ Å for both samples. All annealed $\text{Cu}_2\text{CdSnS}_4$ polycrystalline powders showed similar XRD pattern and no other phases were detected.

Raman spectra of the $\text{Cu}_2\text{CdSnS}_4$ polycrystalline powder annealed at $T_{\text{ann}} = 100$ °C and $T_{\text{ann}} = 400$ °C are presented in Fig. 3. The spectra of $\text{Cu}_2\text{CdSnS}_4$ annealed at different temperatures are all similar except for the widths of the peaks and for clearance only the

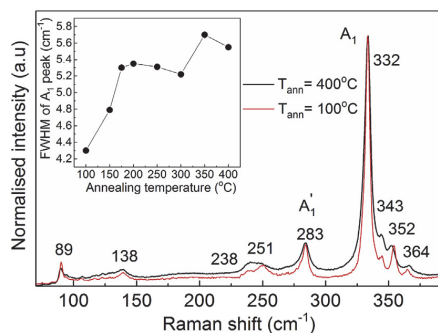


Fig. 3. Raman spectra of $\text{Cu}_2\text{CdSnS}_4$ annealed at temperatures 100 °C and 400 °C for 1 week. The inset graph shows the dependence of the FWHM of the A_1 Raman mode at 332 cm^{-1} on the annealing temperature.

spectra for the material annealed at the lowest ($T_{\text{ann}} = 100$ °C) and at the highest temperature ($T_{\text{ann}} = 400$ °C) used in this study are presented. The observed Raman spectra are in agreement with previously published data [10,15,23] and the two Raman active A_1 symmetry modes characteristic for the stannite type structured $\text{Cu}_2\text{CdSnS}_4$ can be found at 332 cm^{-1} and 283 cm^{-1} . These modes result from the motions of anions only. Other symmetry Raman modes (*E* and B_2 modes) were detected at 89 cm^{-1} , 138 cm^{-1} , 237 cm^{-1} , 268 cm^{-1} , 343 cm^{-1} , 352 cm^{-1} and 364 cm^{-1} .

No significant difference in the Raman peak positions of $\text{Cu}_2\text{CdSnS}_4$ polycrystalline powder annealed at different temperatures could be detected. From the inset graph in Fig. 3 a clear tendency towards increasing full width at the half maximum (FWHM) of the dominating A_1 mode with increasing annealing temperature can be seen. It has been shown that in kesterite $\text{Cu}_2\text{ZnSnS}_4$ and $\text{Cu}_2\text{ZnSnSe}_4$ the low-temperature annealing at different temperatures below and above the critical temperature leads to the changes in the degree of Cu-Zn ordering and in the width and symmetry of the A_1 Raman peak [21,22,24,25]. Broadening of the A_1 Raman peak with increasing annealing temperature was observed and attributed to the higher degree of disordering. It was found that the asymmetry of the A_1 peak is caused by a shoulder peak at low wavenumber side that was attributed to the A_1 mode of the disordered $\text{Cu}_2\text{ZnSnS}_4$. The same trend as was seen in $\text{Cu}_2\text{ZnSnS}_4$ is observed in present study for $\text{Cu}_2\text{CdSnS}_4$ indicating higher level of disordering with increasing annealing temperature. An example of the fitting of the A_1 Raman peak of $\text{Cu}_2\text{CdSnS}_4$ annealed at $T_{\text{ann}} = 100$ °C and $T_{\text{ann}} = 400$ °C with two Lorentzian peaks is shown in Fig. 4. The shoulder peak at the low wavenumber side at 331 cm^{-1} can be attributed to the disordered $\text{Cu}_2\text{CdSnS}_4$ and its relative intensity decreases with decreasing annealing temperature.

3.2. Photoluminescence analysis results

To determine the influence of low-temperature annealing to the defect structure of $\text{Cu}_2\text{CdSnS}_4$ temperature dependent photoluminescence (PL) measurements were performed. PL spectroscopy is non-contact and one of the most sensitive tools for studying the defects in semiconductors. Low temperature ($T = 10$ K) PL spectra of all studied $\text{Cu}_2\text{CdSnS}_4$ polycrystalline powders annealed at different temperatures consist of one broad asymmetric PL band, see Fig. 5. We observe a shift in the PL band position towards lower energies with increasing annealing temperature. The highest energy PL band is situated at 1.215 eV corresponding to the $\text{Cu}_2\text{CdSnS}_4$

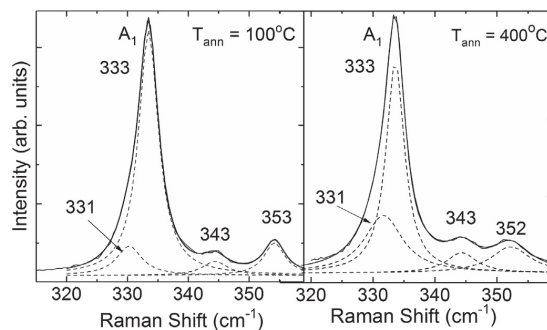


Fig. 4. Fitting of the A_1 Raman peak of $\text{Cu}_2\text{CdSnS}_4$ annealed at 100 °C and 400 °C for 1 week, with two Lorentzian peaks. The shoulder peak at the low wavenumber side at 331 cm^{-1} can be attributed to the disordered $\text{Cu}_2\text{CdSnS}_4$.

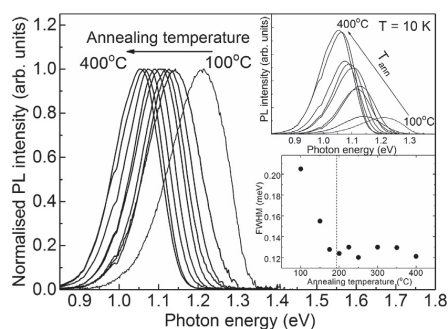


Fig. 5. The normalized low-temperature ($T = 10$ K) PL spectra of $\text{Cu}_2\text{CdSnS}_4$ polycrystalline powders annealed at different temperatures in the range from 100°C to 400°C for 1 week. A shift of the PL band towards lower energies with increasing annealing temperature can be seen. The upper inset graph presents the original PL spectra showing the decrease in the PL intensity with decreasing annealing temperature. In the lower inset graph, the dependence of the FWHM of the PL band on the annealing temperature is shown.

polycrystalline powder annealed at 100°C for 1 week (sample will be named as “ordered” based on the Raman results). The lowest energy PL band is detected at 1.064 eV corresponding to the $\text{Cu}_2\text{CdSnS}_4$ polycrystalline powder annealed at 400°C for 1 week (sample will be named as “disordered”).

The overall difference in the PL band positions of the ordered and disordered $\text{Cu}_2\text{CdSnS}_4$ is about 150 meV. As can be seen from the upper inset graph in Fig. 5, the intensity of the PL signal decreases with decrease in the annealing temperature. In addition, narrowing of the PL band is observed for higher annealing temperatures, the full width at the half maximum (FWHM) being largest for the lowest annealing temperature ($T_{\text{ann}} = 100^\circ\text{C}$), see lower inset graph in Fig. 5. Two regions were observed in the dependence of the FWHM on the annealing temperature: above $T_{\text{ann}} = 200^\circ\text{C}$, the FWHM is almost constant ranging from 0.12 to 0.13 meV, and below $T_{\text{ann}} = 200^\circ\text{C}$ the FWHM increases up to 0.16 eV with decreasing annealing temperature. It is also important to notice that the PL bands are located more than 0.2 eV below the bandgap energy of $\text{Cu}_2\text{CdSnS}_4$ that is reported to be 1.4 eV at room temperature [15] and is even higher at low temperature ($T = 10$ K).

In order to determine the recombination mechanisms behind the PL bands temperature dependent PL measurements were performed. Due to the asymmetric shape of the PL bands, all the spectra were fitted with empirical asymmetric double sigmoid function [26] that describes well such broad and asymmetric PL bands with exponential tail in the low-energy side that are very common in multinary compound semiconductors with spatial

potential fluctuations. The spatial potential fluctuations result from high concentration of randomly distributed charged native defects [25–27]. The asymmetric shape results from the band tails of the density of states function extending into the band gap. The average depth of the fluctuations γ can be determined from the slope of the low energy side of the PL band [26–28]. The corresponding γ values of the PL bands of the $\text{Cu}_2\text{CdSnS}_4$ polycrystalline powders annealed at different temperatures can be found in Table 1 and it was found that the average depth of the fluctuations is very similar in all samples indicating to similar large defect concentrations.

From the temperature dependencies of the PL spectra the temperature dependence of the PL band maxima and integrated intensity were analyzed. It was found that the PL bands measured from the $\text{Cu}_2\text{CdSnS}_4$ polycrystalline powders annealed at temperatures below $T_{\text{ann}} = 200^\circ\text{C}$ are composed of two PL bands that are labeled #1 and #2 (an example of the fitting of the spectra is presented in Fig. 6). The presence of two PL bands also explains the widening of the PL spectrum with decreasing annealing temperature. From the Arrhenius plots the thermal activation energies of the quenching of the PL bands were determined by using the theoretical expression for discrete energy levels for fitting [29]:

$$\Phi(T) = \frac{\Phi_0}{1 + \alpha_1 T^{3/2} + \alpha_2 T^{3/2} \exp(-E_T/kT)}, \quad (1)$$

where Φ is integrated intensity, α_1 and α_2 are the process rate parameters and E_T is the thermal activation energy. The obtained values of the thermal activation energies E_T in dependence of the annealing temperature are listed in Table 1 together with the positions of the PL band maxima and FWHM. Two annealing temperature regions can be observed: two PL bands were detected in $\text{Cu}_2\text{CdSnS}_4$ annealed at temperatures below $T_{\text{ann}} = 200^\circ\text{C}$ showing thermal activation energies of around 60 meV and 110 meV, and one PL band was observed in $\text{Cu}_2\text{CdSnS}_4$ annealed at temperatures above $T_{\text{ann}} = 200^\circ\text{C}$ having high thermal activation energy above 130 meV.

It has been shown that in disordered $\text{Cu}_2\text{ZnSnS}_4$ recombination mechanism involving defect clusters inducing local bandgap energy shrinkage is dominating [24]. The latter results in large band gap fluctuations that create efficient recombination paths for photogenerated carriers in the material. In ordered $\text{Cu}_2\text{ZnSnS}_4$ recombination involving deep acceptor defects (>200 meV) is prevailing at low temperatures [24]. Similarly, high concentration of $\text{Cu}_{\text{Cd}} + \text{Cd}_{\text{Cu}}$ and $2\text{Cu}_{\text{Cd}} + \text{Sn}_{\text{Cd}}$ defect complexes is predicted in $\text{Cu}_2\text{CdSnS}_4$ [7], being responsible for the Cu-Cd disordering. According to the theoretical calculations, the difference in the bandgap energies of disordered and ordered $\text{Cu}_2\text{CdSnS}_4$ is about 100 meV [7]. Therefore, recombination mechanism involving defect clusters is also expected in this material.

Considering that the bandgap energy of $\text{Cu}_2\text{CdSnS}_4$ at low

Table 1

Parameters describing the low temperature PL bands of the $\text{Cu}_2\text{CdSnS}_4$ polycrystalline powders annealed at different temperatures: γ – average depth of the spatial potential fluctuations, $h\nu_{\text{max}}$ – PL band peak position, E_T – thermal activation energy and FWHM – full width at the half maximum of the PL band. For two samples (175°C and 300°C , temperature dependencies were not measured).

Annealing temperature ($^\circ\text{C}$)	γ (meV)	$h\nu_{\text{max}\#1}$ (eV)	$E_{T\#1}$ (meV)	FWHM(#1) (eV)	$h\nu_{\text{max}\#2}$ (eV)	$E_{T\#2}$ (meV)	FWHM(#2) (eV)
100	23	1.165	110 ± 4	0.13	1.245	60 ± 5	0.10
150	22	1.123	105 ± 6	0.13	1.189	62 ± 7	0.11
175	24	1.112	–	0.12	1.161	–	0.11
200	25	1.116	86 ± 8	0.12	–	–	–
225	24	1.106	146 ± 7	0.13	–	–	–
250	25	1.093	135 ± 7	0.12	–	–	–
300	26	1.079	–	0.13	–	–	–
350	27	1.065	151 ± 7	0.13	–	–	–
400	27	1.064	133 ± 5	0.12	–	–	–

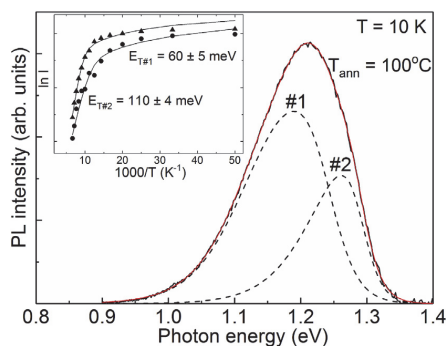


Fig. 6. The low-temperature ($T = 10$ K) PL spectrum of $\text{Cu}_2\text{CdSnS}_4$ polycrystalline powder annealed at 100°C for 1 week together with the fitting result. The inset graph presents the Arrhenius plots for the two PL bands used for determining the thermal quenching activation energies for #1 and #2.

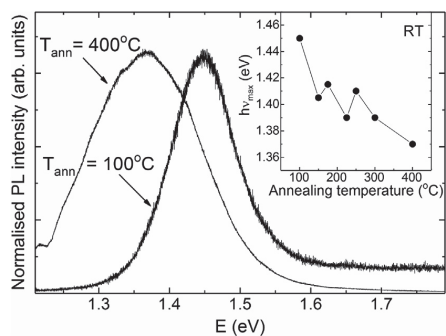


Fig. 7. RT-PL spectra of $\text{Cu}_2\text{CdSnS}_4$ annealed at temperatures 100°C and 400°C for 1 week. The shift of the position of the PL band maximum towards lower energies with increasing annealing temperature is detected.

temperatures is close to 1.5 eV, the PL bands are very far from the band edge, separation of the PL band from the band gap is over 300 meV and over 200 meV for #1 and #2, respectively. Different thermal activation energies of the PL band quenching were found for #1 (above 100 meV) and #2 (below 100 meV), indicating to a different recombination channel. Considering the thermal

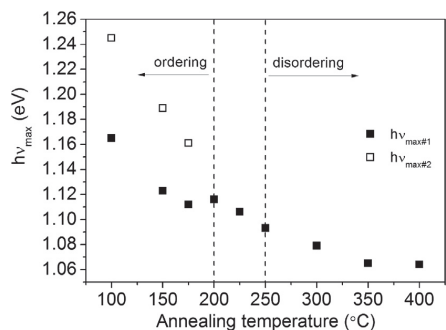


Fig. 8. PL band positions of $\text{Cu}_2\text{CdSnS}_4$ polycrystalline powders depending on the low-temperature annealing in the range from 100°C to 400°C for 1 week.

activation energies and the PL band positions with respect to the low temperature bandgap energy of $\text{Cu}_2\text{CdSnS}_4$, one can see that in both ordered and disordered $\text{Cu}_2\text{CdSnS}_4$ the dominating radiative recombination is related to the defect clusters inducing bandgap energy shrinkage that was also seen in disordered $\text{Cu}_2\text{ZnSnS}_4$ [30]. However, the dominating defect clusters are different in ordered and disordered $\text{Cu}_2\text{CdSnS}_4$. We propose that in disordered $\text{Cu}_2\text{CdSnS}_4$ the $2\text{Cu}_{\text{Cd}} + \text{Sn}_{\text{Cd}}$ defect complexes inducing large bandgap energy fluctuations (with depth > 0.4 eV [7]) dominate. In ordered material the coexistence of $2\text{Cu}_{\text{Cd}} + \text{Sn}_{\text{Cd}}$ and $\text{Cu}_{\text{Cd}} + \text{Cd}_{\text{Cu}}$ defect complexes is present resulting in the two observed PL bands #1 and #2. However, based on the PL intensity analysis (see upper inset graph in Fig. 5) the overall concentration of the mentioned defect complexes is reduced in ordered material.

RT-PL measurements were also performed to the $\text{Cu}_2\text{CdSnS}_4$ polycrystalline powders annealed at different temperatures. Similarly to low-temperature PL (10 K) results a shift of the PL band towards lower energies with increasing annealing temperature was observed, the positions of the PL bands being 1.45 eV and 1.37 eV for samples annealed at 100°C and 400°C , respectively. For clearance, only the spectra of ordered and disordered $\text{Cu}_2\text{CdSnS}_4$ (e.g. annealing temperatures 100°C and 400°C) is presented in Fig. 7. Much broader PL band is observed for the disordered material, most probably caused by larger band gap fluctuations. Considering the room temperature bandgap energy of $\text{Cu}_2\text{CdSnS}_4$ around 1.4 eV [3,4], the observed PL bands result from the band-to-band recombination. Notice, that it is not the same PL band that was observed at low temperature (10 K).

Finally, Fig. 8 shows low-temperature PL band position of $\text{Cu}_2\text{CdSnS}_4$ depending on the annealing temperature in the range from 100°C to 400°C for 1 week. The vertical dashed lines in Fig. 8 indicate to the annealing temperature region where the PL band position is almost constant and change in the recombination mechanism has not yet taken place. Almost constant FWHM of the A_1 Raman mode was observed in the same annealing temperature region from 200°C to 250°C . We can conclude that it is possible to modify the degree of disordering with the low-temperature annealing treatments below the critical temperature that according to our study lies in the temperature range from 200°C to 250°C .

4. Conclusions

From the Raman scattering and temperature dependent PL analysis of the $\text{Cu}_2\text{CdSnS}_4$ polycrystalline powder we can conclude that the Cu-Cd disordering predicted by the theoretical first principles calculations [7] is present in this material. We have shown in this study that the degree of disordering can be reduced with the low-temperature annealing treatments below the critical temperature that according to our study lies in the temperature range from 200°C to 250°C . It was found the change in the degree of disordering in $\text{Cu}_2\text{CdSnS}_4$ is accompanied with the change in the radiative recombination channel related to different type of defect clusters.

Acknowledgements

This work was supported by institutional research funding IUT (IUT19-28) of the Estonian Ministry of Education and Research, by the European Union through the European Regional Development Fund, Project TK141, and by FP7 Project CHEETAH Grant Agreement No. 609788.

References

- [1] T. Kato, H. Hiroi, N. Sakai, S. Muraoka, H. Sugimoto, Characterization of front

- and back interface on $\text{Cu}_2\text{ZnSnS}_4$ thin-film solar cells, in: Proc. of 27th EUPVSEC, 2012, pp. 2236–2239. <http://dx.doi.org/10.4229/27thEUPVSEC2012-3C0.4.2>.
- [2] W. Schäfer, R. Nitsche, Tetrahedral quaternary chalcogenides of the type $\text{Cu}_2\text{-II-IV-S}_4(\text{Se}_4)$, Mater. Res. Bull. 9 (1974) 645–654. [http://dx.doi.org/10.1016/0025-5408\(74\)90135-4](http://dx.doi.org/10.1016/0025-5408(74)90135-4).
- [3] K. Ito, T. Nakazawa, Electrical and optical properties of stannite-type quaternary semiconductor thin films, Jpn. J. Appl. Phys. 27 (1988) 2094–2097. <http://iopscience.iop.org/article/10.1143/JJAP.27.2094/pdf>.
- [4] H. Matsushita, T. Ichikawa, A. Katsui, Structural, thermodynamical and optical properties of $\text{Cu}_2\text{-II-IV-VI}_4$ quaternary compounds, J. Mater. Sci. 40 (2005) 2003–2005. <http://doi.org/10.1007/s10853-005-1223-5>.
- [5] S. Rühle, Tabulated values of the Shockley-Queisser limit for single junction solar cells, Sol. Energy 130 (2016) 139–147. <http://dx.doi.org/10.1016/j.solener.2016.02.015>.
- [6] L. Meng, Y. Li, B. Yao, Z.-H. Ding, G. Yang, R.-J. Liu, R. Deng, L. Liu, Mechanism of effect of intrinsic defects on electrical and optical properties of $\text{Cu}_2\text{CdSnS}_4$: an experimental and first-principles study, J. Phys. D: Appl. Phys. 48 (2015), 445005 (7pp). <https://doi.org/10.1088/0022-3727/48/4/445005>.
- [7] Z.-K. Yuan, S. Chen, H. Xiang, X.-G. Gong, A. Walsh, J.-S. Park, I. Repins, S.-H. Wei, Engineering solar cell absorbers by exploring the band alignment and defect disparity: the case of Cu- and Ag-based kesterite compounds, Adv. Funct. Mater. 25 (2015), 6766–6743. <http://dx.doi.org/10.1002/adfm.201522272>.
- [8] H. Guan, J. Zhao, X. Wang, F. Yu, $\text{Cu}_2\text{CdSnS}_4$ thin film prepared by a simple solution method, Chalcogenide Lett. 10 (10, October) (2013) 367–372.
- [9] W. Zhao, G. Wang, Q. Tian, L. Huang, S. Gao, D. Pan, Solution-processed $\text{Cu}_2\text{CdSn(S,Se)}_4$ thin film solar cells, Sol. Energy Mater. Sol. Cells 133 (February) (2015) 15–20. <http://dx.doi.org/10.1016/j.solmat.2014.10.040>.
- [10] H. Guo, Y. Li, X. Fang, K. Zhang, J. Ding, Co-sputtering deposition and optical-electrical characteristic of $\text{Cu}_2\text{CdSnS}_4$ thin films for use in solar cells, Mater. Lett. 162 (1) (2016) 97–100. <http://dx.doi.org/10.1016/j.matlet.2015.09.112>.
- [11] A.S. Ibraheem, Y. Al-Douri, U. Hashim, D. Prakash, K.D. Verma, M. Ameri, Fabrication, analysis and characterization of $\text{Cu}_2\text{Zn}_{1-x}\text{Cd}_x\text{SnS}_4$ quaternary alloy nanostructures deposited on GaN, J. Mater. Sci. 51 (14) (2016) 6876–6885. <http://dx.doi.org/10.1007/s10853-016-9975-7>.
- [12] A.A. Odeh, Y. Al-Douri, R.M. Ayub, A.S. Ibraheem, Ultrasonic effect on optical, topographical and morphological studies of $\text{Cu}_2\text{CdSnS}_4$ quaternary alloy nanostructures, J. Alloys Compd. 686 (2016) 883–895. <http://dx.doi.org/10.1016/j.jallcom.2016.06.235>.
- [13] L. Nie, S. Liu, Y. Chai, R. Yuan, Spray pyrolysis deposition and photoresponse of $\text{Cu}_2\text{CdSnS}_4$ thin films, J. Anal. Appl. Pyrolysis 112 (2015) 363–368. <http://dx.doi.org/10.1016/j.jaap.2014.12.020>.
- [14] A.S. Ibraheem, Y. Al-Douri, U. Hashim, M.R. Ghezzer, A. Addou, W.K. Ahmed, Cadmium effect on optical properties of $\text{Cu}_2\text{Zn}_{1-x}\text{Cd}_x\text{SnS}_4$ quaternary alloys nanostructures, Sol. Energy 114 (2015) 39–50. <http://dx.doi.org/10.1016/j.solener.2015.01.018>.
- [15] K. Timmo, M. Kauk-Kuusik, M. Altsaar, J. Raudoja, T. Raadik, M. Grossberg, T. Varema, M. Pilvet, I. Leinemann, O. Volobujeva, E. Mellikov, Novel $\text{Cu}_2\text{CdSnS}_4$ and $\text{Cu}_2\text{ZnGeSe}_4$ absorber materials for monograin layer solar cell applications, Proceedings of the 28th European Photovoltaic Solar Energy Conference and Exhibition, Paris, France (September 30–October 04 2013), p. 2385, DOI: 10.4229/28thEUPVSEC2013-3BV.6.14.
- [16] S. Bourdais, C. Choné, B. Delatouche, A. Jacob, G. Larramona, C. Moisan, A. Lafond, F. Donatini, G. Rey, S. Siebentritt, A. Walsh, G. Dennler, Is the Cu/Zn disorder the main culprit for the voltage deficit in kesterite solar cells? Adv. Energy Mater. (2016) 1502276. <http://dx.doi.org/10.1002/aenm.201502276>.
- [17] G. Krämmer, C. Huber, T. Schnabel, C. Zimmermann, M. Lang, E. Ahlswede, H. Kalt, M. Hetterich, Order-disorder related band gap changes in $\text{Cu}_2\text{ZnSn(S,Se)}_4$: impact on solar cell performance, in: Proc. 42nd IEEE Photovoltaic Specialist Conference (PVSC), 2015. <http://dx.doi.org/10.1109/PVSC.2015.7356096>.
- [18] K. Timmo, M. Kauk-Kuusik, M. Pilvet, T. Raadik, M. Altsaar, M. Danilson, M. Grossberg, J. Raudoja, K. Ernits, Influence of order-disorder in $\text{Cu}_2\text{ZnSnS}_4$ powders of monograin layer solar cells, Thin Solid Films (2016). <http://dx.doi.org/10.1016/j.tsf.2016.10.017>.
- [19] M. Grossberg, J. Krustok, J. Raudoja, T. Raadik, The role of structural properties on deep defect states in $\text{Cu}_2\text{ZnSnS}_4$ studied by photoluminescence spectroscopy, Appl. Phys. Lett. 101 (2012) 102102. <http://dx.doi.org/10.1063/1.4750249>.
- [20] T. Raadik, J. Krustok, M. Kauk-Kuusik, K. Timmo, M. Grossberg, K. Ernits, J. Bleuse, Low temperature time resolved photoluminescence in ordered and disordered $\text{Cu}_2\text{ZnSnS}_4$ single crystals, Phys. B 508 (2017) 47–50. <http://dx.doi.org/10.1016/j.physb.2016.12.011>.
- [21] G. Rey, A. Redinger, J. Sendl, T.P. Weiss, M. Thevenin, M. Guennou, B. El Adiband, S. Siebentritt, The band gap of $\text{Cu}_2\text{ZnSnSe}_4$: effect of order-disorder, Appl. Phys. Lett. 105 (2014) 112106. <http://dx.doi.org/10.1063/1.4896315>.
- [22] J.J.S. Scragg, L. Choubrac, A. Lafond, T. Ericson, C. Platzer-Björkman, A low-temperature order-disorder transition in $\text{Cu}_2\text{ZnSnS}_4$ thin films, Appl. Phys. Lett. 104 (2014) 041911. <http://dx.doi.org/10.1063/1.4863685>.
- [23] M. Pilvet, M. Kauk-Kuusik, M. Altsaar, M. Grossberg, M. Danilson, K. Timmo, A. Mere, V. Mikli, Compositionally tunable structure and optical properties of $\text{Cu}_{1.85}(\text{Cd}_x\text{Zn}_{1-x})_{1.15}\text{SnS}_4$ ($0 \leq x \leq 1$) monograin powders, Thin Solid Films 582 (2015) 180. <http://dx.doi.org/10.1016/j.tsf.2014.10.091>.
- [24] T. Gürel, C. Sevik, T. Cagin, Characterization of vibrational and mechanical properties of quaternary compounds $\text{Cu}_2\text{ZnSnS}_4$ and $\text{Cu}_2\text{ZnSnSe}_4$ in kesterite and stannite structures, Phys. Rev. B 84 (2011) 205201. <https://doi.org/10.1103/PhysRevB.84.205201>.
- [25] M. Grossberg, J. Krustok, T. Raadik, M. Kauk-Kuusik, J. Raudoja, Photoluminescence study of disordering in the cation sublattice of $\text{Cu}_2\text{ZnSnS}_4$, Curr. Appl. Phys. 14 (2014) 1424–1427. <http://dx.doi.org/10.1016/j.cap.2014.08.013>.
- [26] J. Krustok, H. Collan, M. Yakushev, K. Hjelt, The role of spatial potential fluctuations in the shape of the PL bands of multinary semiconductor compounds, Phys. Scr. 379 (1999) 179–182. <http://iopscience.iop.org/1402-4896/1999/179/041>.
- [27] M. Grossberg, J. Krustok, K. Timmo, M. Altsaar, Radiative recombination in $\text{Cu}_2\text{ZnSnSe}_4$ monograins studied by photoluminescence spectroscopy, Thin Solid Films 517 (2009) 2489–2492. <http://dx.doi.org/10.1016/j.tsf.2008.11.024>.
- [28] A.P. Levanyuk, V.V. Osipov, Edge luminescence of direct-gap semiconductors, Sov. Phys. Usp. 24 (1981) 187–215. <https://doi.org/10.1070/PU1981v024n03ABEH004770>.
- [29] J. Krustok, H. Collan, K. Hjelt, Does the low temperature Arrhenius plot of the photoluminescence intensity in CdTe point towards an erroneous activation energy? J. Appl. Phys. 81 (1997) 1442–1445. <http://dx.doi.org/10.1063/1.363903>.
- [30] S. Chen, X.G. Gong, A. Walsh, S.-H. Wei, Crystal and electronic band structure of $\text{Cu}_2\text{ZnSnX}_4$ ($X=\text{S}$ and Se) photovoltaic absorbers: first-principles insights, Appl. Phys. Lett. 94 (2009) 041903. <http://dx.doi.org/10.1063/1.3074499>.

PAPER IV

K. Timmo, M. Kauk-Kuusik, M. Altsaar, J. Raudoja, T. Raadik, M. Grossberg, T. Varema, **M. Pilvet**, I. Leinemann, O. Volobujeva, E. Mellikov, Novel $\text{Cu}_2\text{CdSnS}_4$ and $\text{Cu}_2\text{ZnGeSe}_4$ absorber materials for monograin layer solar cell application, Proceeding of *EU PVSEC 2013 (2013)*, Wiley-Blackwell 2385–2388.

NOVEL $\text{Cu}_2\text{CdSnS}_4$ AND $\text{Cu}_2\text{ZnGeSe}_4$ ABSORBER MATERIALS FOR MONOGRAIN LAYER SOLAR CELL APPLICATION

Timmo K. *, Kauk-Kuusik M., Altsaar M., Raudoja J., Raadik T., Grossberg M., Varema T., Pilvet M., Leinemann I., Volobujeva O., Mellikov E.

Department of Materials Science, Tallinn University of Technology
Ehitajate tee 5, 19086 Tallinn, Estonia
timmokas@yahoo.com

ABSTRACT: This study shows the additional ability for tuning bandgap of CZTSSe solar cell absorber materials through substitution of Sn by Ge or Zn by Cd atoms in the crystal lattice forming new $\text{Cu}_2\text{ZnGeSe}_4$ or $\text{Cu}_2\text{CdSnS}_4$ compounds in the monograin powder form. $\text{Cu}_2\text{CdSnS}_4$ and $\text{Cu}_2\text{ZnGeSe}_4$ monograin powders were synthesized from binary compounds in molten CdI_2 and KI as flux materials in sealed quartz ampoules at 610°C and 710°C, respectively. The phase composition of synthesized powders was determined by XRD and Raman spectroscopy. Raman spectrum of the $\text{Cu}_2\text{ZnGeSe}_4$ powder revealed dominating A_1 Raman peak at 204 cm^{-1} , other Raman peaks were detected at 92, 173, 177, 271, 283, and 292 cm^{-1} . Raman spectra of $\text{Cu}_2\text{CdSnS}_4$ powder crystals showed the characteristic Raman frequencies at 90, 250, 283, 333 and 353 cm^{-1} . The effective bandgap energy values determined from the EQE data of the $\text{Cu}_2\text{ZnGeSe}_4$ and $\text{Cu}_2\text{CdSnS}_4$ devices are 1.35 and 1.4 eV. Solar cells based on the $\text{Cu}_2\text{ZnGeSe}_4$ monograin powder showed the best conversion efficiency of 1.3 %. The solar cells based on the $\text{Cu}_2\text{CdSnS}_4$ monograin powder showed the best conversion efficiency of 2.7 %.

Keywords: $\text{Cu}_2\text{CdSnS}_4$, $\text{Cu}_2\text{ZnGeSe}_4$, Photoluminescence, Spectral Response, Recrystallization, Solar cell

1 INTRODUCTION

Advancements in $\text{Cu}_2\text{ZnSn}(\text{S}_x\text{Se}_{1-x})_4$ (CZTSSe) based solar cells have recently achieved power conversion efficiencies over 11%, indicating the potential of this low cost, earth abundant material system as a viable alternative to $\text{Cu}(\text{In,Ga})\text{Se}_2$ and CdTe absorbers [1]. An ideal solar energy absorber material should have a bandgap around 1.3-1.4 eV and therefore the bandgap of solar cell absorber material needs to be adjusted to this energy region. The bandgap of CZTSSe solid solutions have been optimized mainly by varying the S/Se ratio [2].

$\text{Cu}_2\text{ZnGeSe}_4$ (CZGeSe) and $\text{Cu}_2\text{CdSnS}_4$ (CCdTS), members of $\text{Cu}_2\text{-II-IV-VI}_4$ family, are promising materials for absorber layer in thin film heterojunction solar cells owing direct bandgaps, high absorption coefficients and *p*-type conductivity. Both quaternary compounds are known to have a stannite structure [3, 4, 5]. The bandgap of CZGeSe, as determined experimentally and theoretically [6, 7, 8] is between 1.2-1.6 eV and the bandgap of $\text{Cu}_2\text{CdSnS}_4$ is found to be between 1.37-1.5eV [8, 9]. So, these materials should be suitable for optimum conversion efficiency for solar cells.

The first report about the fabrication of $\text{Cu}_2\text{ZnGeSe}_4$ thin films for photovoltaic applications were given by Matsushita *et al.* [6], but there are no results about solar cell parameters. Ford *et al.* [10] reported an efficiency of 0,51% for $\text{Cu}_2\text{ZnGe}(\text{S}_x\text{Se}_{1-x})_4$ thin film solar cells fabricated by annealing $\text{Cu}_2\text{ZnGeS}_4$ nanocrystals in elemental selenium vapor. To our knowledge there are no published data about the performance of $\text{Cu}_2\text{CdSnS}_4$ based solar cells.

The aim of the current study is to show the additional ability for tuning bandgap of CZTSSe through substitution of Sn by Ge or Zn by Cd atoms into the crystal lattice forming above mentioned new $\text{Cu}_2\text{ZnGeSe}_4$ or $\text{Cu}_2\text{CdSnS}_4$ compounds in the form of monograin powders for photovoltaic applications. Molten salt synthesis, one of the methods of preparing semiconductor powders, involves the use of a molten salt as the medium for preparing quaternary compounds from

their constituent elements. In our previous reports [11, 12, 13], we have shown that CZTSe, CZTS and CZTSSe monograin powders with modified chemical composition could be prepared by this method. The highest certified efficiency of CZTSSe solar cell achieved by monograin layer (MGL) technology is 8.4 % [14].

2 EXPERIMENTAL

2.1 Powder preparation

The $\text{Cu}_2\text{CdSnS}_4$ and $\text{Cu}_2\text{ZnGeSe}_4$ monograin powder materials were synthesized from binary precursor compounds in the molten CdI_2 or KI as flux materials, respectively. The initial compositions of precursor mixtures were calculated for stoichiometric $\text{Cu}_2\text{CdSnS}_4$ and Zn-rich $\text{Cu}_{1.8}\text{Zn}_{1.2}\text{GeSe}_4$ monograin powder synthesis. Binary compounds were self-synthesized from high purity (99.999%) elements in evacuated quartz ampoules. After synthesis, all precursors were ground in an agate mortar before use in the powder growth process. KI was heated under dynamic vacuum (continuous vacuum pumping) at temperatures up to 270°C for dehydration. The precursors were mixed and ground in a ball mill in intended quantities and ratios. The ground initial substances were sealed into evacuated quartz ampoules and annealed at 610°C and 710°C, respectively. The growth process was finished by cooling the ampoules in air. Crystals of the synthesized powders were released from flux by washing with deionized water. More details about monograin powder growth process could be found elsewhere [15]. Narrow granulometric fractions of $\text{Cu}_2\text{CdSnS}_4$ and $\text{Cu}_2\text{ZnGeSe}_4$ monograin powder grains were separated by sieving and post-annealed in sulphur vapor in two-temperature zone arrangement and in the isothermal conditions in closed ampoules at 740°C.

2.2 Solar cell preparation

Annealed powders were used as the absorber materials in monograin layer (MGL) solar cells. The structure of solar cells based on new compounds was

remained the same as in CZTS based MGL solar cells. Monograins were covered with *n*-type CdS buffer layer by chemical bath deposition. After the CdS deposition, the grains were embedded into the epoxy layer so that the top of the grains remained uncovered. After the hardening of epoxy, first the intrinsic ZnO and then aluminium doped ZnO were sputtered on the top of CdS layer by radio frequency sputtering. After the deposition of the ZnO window layer, 1-2 μ m thick indium grid contacts were evaporated on top. For applying back contact, the epoxy was removed partly by etching with concentrated H₂SO₄ from the back side of MGL. The last procedure enabled access to each grain. Then the uncovered monograins were mechanically polished with sandpaper and graphite contacts were applied on the mechanically activated back side of absorber crystals. The active area of the MGL solar cells (on the front contact side of MGL) is around 75 % of the total area. The other 25 % of the total area, comprising epoxy between the absorber crystals, is passive.

2.3 Characterization

The bulk composition of powder crystals was determined by energy dispersive spectroscopy (EDS). The shape and surface morphology of crystals were studied with the high resolution scanning electron microscope (SEM) Zeiss ULTRA 55. X-ray diffraction (XRD) patterns were recorded by a Bruker AXS D5005 diffractometer with the monochromatic Cu K α radiation in the 2 θ interval of 10–80 deg using the step of 0.04 deg and counting time 2 s/step.

Photovoltaic properties of graphite/Cu₂ZnGeSe₄/CdS/ZnO or graphite/Cu₂CdSnS₄/CdS/ZnO structures were characterized by I–V measurements under 100 mW/cm² tungsten halogen illumination. Spectral response measurements were performed by the help of a computer-controlled SPM-2 monochromator and a 100-W tungsten halogen lamp. The room temperature micro-Raman spectra were recorded by using a Horiba LabRam HR high-resolution spectrometer equipped with a multichannel detection system in the backscattering configuration. The incident laser light with the wavelength of 532 nm was focused on samples within a spot of 2 μ m in diameter and the spectral resolution of the spectrometer was 0.5 cm⁻¹. For photoluminescence (PL) measurements, the CZGeSe and CCdTS monograin powders were mounted in the closed-cycle He cryostat and cooled down to 10 K. The 405 nm laser line was used for PL excitation and the spectra were recorded by using InGaAs detector.

3 RESULTS AND DISCUSSION

3.1 Compositional and morphological analysis

The bulk chemical composition of powder crystals analysed by energy dispersive spectroscopy showed that the composition of Cu₂CdSnS₄ powder crystals was nearly stoichiometric with compositional ratios of [Cu]/([Cd]+[Sn]) = 0.97 and [Cd]/[Sn] = 1.0. Cu₂ZnGeSe₄ monograin powder composition was Zn-rich: the compositional ratios of [Cu]/([Zn]+[Ge]) = 0.96 and [Zn]/[Ge] = 1.09.

Fig. 1 shows SEM micrographs of a) Cu₂ZnGeSe₄ and b) Cu₂CdSnS₄ monograin powder crystals. It is observed that the Cu₂ZnGeSe₄ powder grains are nonaggregated microcrystals with rounded grain edges and Cu₂CdSnS₄

powder crystals have tetragonal shape with sharp grain edges. The different shape of product crystals can be

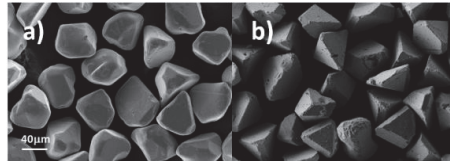


Figure 1: SEM micrographs of a) Cu₂ZnGeSe₄ and b) Cu₂CdSnS₄ monograin powders.

explained by different solubility of synthesized materials in molten salts. Round edges of the grown grains indicate that the solubility of Cu₂ZnGeSe₄ in KI must be higher than the solubility of Cu₂CdSnS₄ in CdI₂ [16].

3.2 XRD analysis

XRD study was applied to characterize the crystal structure of powder crystals. Fig. 2a shows XRD patterns of Cu₂ZnGeSe₄ monograin powder synthesized in KI, which resemble that of a tetragonal-symmetry structure with the *I*42*m* space group (ICDD PDF-4-2011, 00-055-0294).

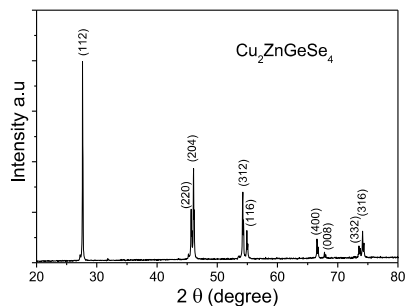


Figure 2a: XRD pattern of Cu₂ZnGeSe₄ monograin powder.

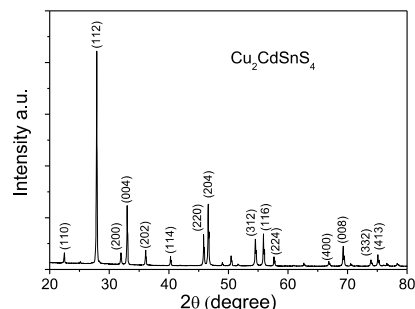


Figure 2b: XRD pattern of Cu₂CdSnS₄ monograin powder.

The values are in good agreement with Cu₂ZnGeSe₄ bulk crystals presented by Matsushita *et al.* [3] and no secondary phases were detected. The tetragonal CZGSe structure found in experimental studies has been typically

assigned to the stannite phase [3, 4]. It is interesting to note that the stannite phase has the same symmetry as a specific disordering of the kesterite phase, the $I\bar{4}2m$ symmetry is the result of a relatively low energy Cu-Zn cation exchange occurring randomly in the kesterite phase. The similarity in atomic numbers between Cu, Zn, Ge contribute to the difficulty in distinguishing between stannite and kesterite using XRD [17, 18].

Fig. 2b shows the XRD pattern of $\text{Cu}_2\text{CdSnS}_4$ monograin powder. Our diffraction pattern matches those reported for $\text{Cu}_2\text{CdSnS}_4$ in the literature [19, 20] and those standard patterns in JCPDS card database (stannite phase, PDF no. 29-0537). From the diffraction pattern the lattice parameters were determined to be $a=5.59 \text{ \AA}$ and $c=10.84 \text{ \AA}$, these values indicate also stannite structure [21].

3.3 Raman spectroscopy analysis

In the system Cu-Zn-Sn-S the diffraction peaks of the phases Cu_2SnS_3 and ZnS cannot be distinguished from the $\text{Cu}_2\text{ZnSnS}_4$ phase due to their structural similarity (the diffraction peaks of these phases can overlap) [22], the same problem can be with other quaternary compounds. Therefore, besides X-ray diffraction analysis, Raman spectroscopy study is useful to investigate the phase purity and composition of stannite and kesterite materials. The polished cross-sectional samples of $\text{Cu}_2\text{ZnGeSe}_4$ and $\text{Cu}_2\text{CdSnS}_4$ monograins were used for Raman studies of the bulk of the materials (see Fig. 3).

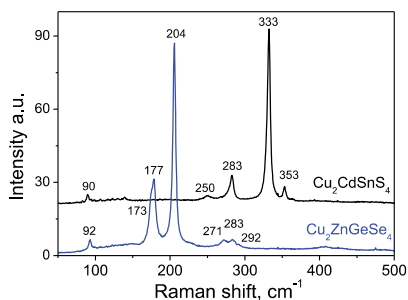


Figure 3: Raman spectra of $\text{Cu}_2\text{ZnGeSe}_4$ and $\text{Cu}_2\text{CdSnS}_4$ monograin powder crystals.

In case of the $\text{Cu}_2\text{ZnGeSe}_4$ powder, the dominating A_1 Raman peak appears at 204 cm^{-1} , other Raman peaks were detected at $92, 173, 177, 271, 283,$ and 292 cm^{-1} . Raman spectra of $\text{Cu}_2\text{CdSnS}_4$ powder crystals revealed main peaks at $90, 250, 283, 333$ and 353 cm^{-1} , the peak at 333 cm^{-1} being the dominating A_1 mode. As there were not observed other Raman peaks corresponding to the binary or ternary phases possible to co-exist in the studied materials, this is indicating to the single phase composition of the CZGeSe and CCdTS monograins.

3.4 Solar cell characterization

To evaluate the potential applicability of $\text{Cu}_2\text{ZnGeSe}_4$ and $\text{Cu}_2\text{CdSnS}_4$ monograin powders as photovoltaic materials, the I-V curves of MGL solar cells based on these materials have been measured in the dark and under illumination. The current-voltage (I - V) characteristics of the best performing $\text{Cu}_2\text{ZnGeSe}_4$ and $\text{Cu}_2\text{CdSnS}_4$ MGL

solar cells are shown in Fig. 4.

The solar cells based on the $\text{Cu}_2\text{ZnGeSe}_4$ monograin powder showed the best conversion efficiency of 1.3 %.

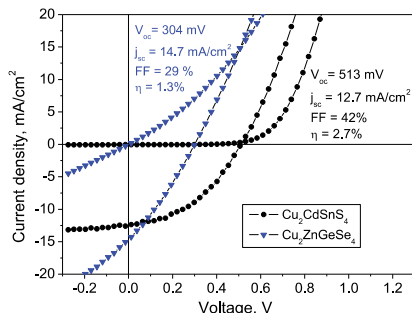


Figure 4: Current-voltage characteristics of $\text{Cu}_2\text{ZnGeSe}_4$ (triangle dots) and $\text{Cu}_2\text{CdSnS}_4$ (round dots) MGL solar cells.

The highest values of output parameters from different CZGeSe solar cells were $V_{oc}=474 \text{ mV}$, $j_{sc}=15.1 \text{ mA/cm}^2$ and $FF=29 \%$. The solar cells based on the $\text{Cu}_2\text{CdSnS}_4$ monograin powder showed the best conversion efficiency of 2.7 % with $V_{oc}=513 \text{ mV}$, $j_{sc}=12.7 \text{ mA/cm}^2$ and $FF=42 \%$.

The relative quantum efficiency (QE) spectra are shown in Fig. 5.

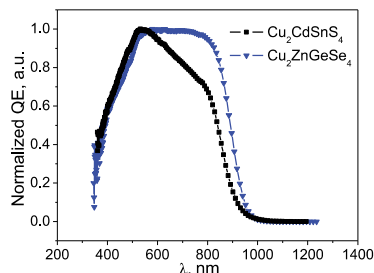


Figure 5: Normalized quantum efficiency spectra of $\text{Cu}_2\text{ZnGeSe}_4$ (triangle dots) and $\text{Cu}_2\text{CdSnS}_4$ (square dots) MGL solar cell devices.

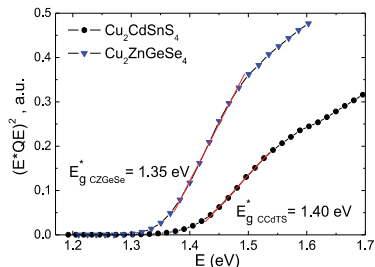


Figure 6: Bandgap energy determination using EQE data of $\text{Cu}_2\text{ZnGeSe}_4$ (triangle dots) and $\text{Cu}_2\text{CdSnS}_4$ (round dots) MGL solar cells.

The low-energy side of the quantum efficiency spectrum near the bandgap energy E_g of the absorber can be fitted by the equation [23]:

$$QE \approx KaL_{eff} \approx A(E - E_g^*)^2/E$$

where E_g^* is an effective bandgap energy and constant A includes all parameters that do not depend on E . Therefore $(E^*QE)^2$ vs. E curves (Fig. 6) should have a linear segment from which a value for E_g^* can be found. Effective bandgap energy values determined from the EQE data of the CZGeSe and CCdTS devices are 1.35 and 1.4 eV, respectively.

3.5 Photoluminescence analysis

Low-temperature PL spectra of the $\text{Cu}_2\text{ZnGeSe}_4$ and $\text{Cu}_2\text{CdSnS}_4$ monograin powders are presented in Fig. 7. Both spectra are consisted of one broad asymmetric PL band at 1.09 eV in $\text{Cu}_2\text{CdSnS}_4$ and 1.26 eV in $\text{Cu}_2\text{ZnGeSe}_4$, respectively, that shows large blueshift of about 15 meV/decade with increasing laser power indicating the presence of spatial potential fluctuations in the materials caused by random distribution of large concentration of intrinsic defects. Similar PL bands resulting from the recombination involving states in the valence and conduction band tail are also observed in $\text{Cu}_2\text{ZnSnSe}_4$ and $\text{Cu}_2\text{ZnSnS}_4$ [24, 25]. Detailed analysis of the PL spectra of the $\text{Cu}_2\text{ZnGeSe}_4$ and $\text{Cu}_2\text{CdSnS}_4$ monograin powders will be presented elsewhere.

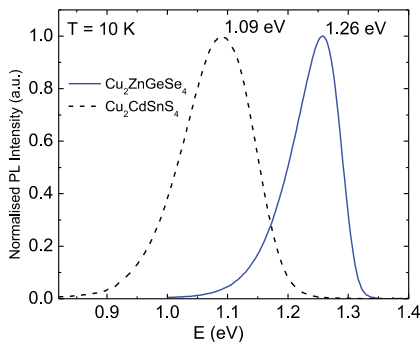


Figure 7: Low-temperature PL spectra of the $\text{Cu}_2\text{ZnGeSe}_4$ and $\text{Cu}_2\text{CdSnS}_4$ monograin powders.

4 CONCLUSION

In conclusion, $\text{Cu}_2\text{CdSnS}_4$ and $\text{Cu}_2\text{ZnGeSe}_4$ monograin powders were successfully synthesized in molten salts and used as absorber materials in MGL solar cells. The effective bandgap energy values determined from the EQE data of the $\text{Cu}_2\text{ZnGeSe}_4$ and $\text{Cu}_2\text{CdSnS}_4$ devices are 1.35 and 1.4 eV. The solar cells based on the $\text{Cu}_2\text{ZnGeSe}_4$ and $\text{Cu}_2\text{CdSnS}_4$ monograin powders showed the best conversion efficiency of 1.3 % and 2.7 %, respectively. Further work to optimize the solar cell performance and to improve the materials quality is in progress.

ACKNOWLEDGEMENTS

This work was supported by the Estonian Science Foundation grants G9346, G9425, G8964, the Estonian Ministry of Education and Science target financing

project SF0140099s08, Projects TK117T, AR10128 and AR12128.

REFERENCES

- 1) T. K. Todorov, J. Tang, S. Bag, O. Gunawan, T. Gokmen, Y. Zhu, D. B. Mitzi, *Adv. Energy Mater.* 3 (2013) 34–38.
- 2) K. Timmo, M. Altosaar, J. Raudoja, K. Muska, M. Pilvet, M. Kauk, T. Varema, M. Danilson, O. Volobujeva, E. Mellikov, *Solar Energy Materials & Solar Cells* 94 (2010) 1889–1892.
- 3) H. Matsushita, T. Maeda, A. Katsui, T. Takizawa, *J. Cryst. Growth* 208 (2000) 416–422.
- 4) O. V. Parasyuk, L. V. Piskach, Y. E. Romanyuk, I. D. Olekseyuk, V. I. Zaremba, V. I. Pekhnyo, *J. Alloys Cmpd.* 397 (2005) 85.
- 5) Y.-F. Liu, M. Y. Ge, H. H. Luo, Y. Sun, J. Wu, N. Dai, *J. Infrared Millim. Waves*, Vol. 31 (2012) No.1.
- 6) H. Matsushita, T. Ochiai, A. Katsui, *J. Cryst. Growth* 275 (2005) 995–999.
- 7) C. Lee, C. D. Kim, *J. Korean Phys. Soc.* 37 (2000) 364.
- 8) S. Chen, X. G. Gong, A. Walsh, S.-H. Wei, *Phys. Rev. B* 79 (2009) 165211.
- 9) M. Cao, L. Li, W. Z. Fan, X. Y. Liu, Y. Sun, Y. Shen, *Chemical Physics Letters* 534 (2012) 34–37.
- 10) G. M. Ford, Q. Guo, R. Agrawal, H. W. Hillhouse, *Chem. Mater.* 23 (2011) 2626.
- 11) M. Altosaar, J. Raudoja, K. Timmo, M. Danilson, M. Grossberg, M. Krunks, T. Varema, and E. Mellikov, *Proceedings of the 2006 IEEE WCPEC-4, Hawaii, May 7-12 (2006)*.
- 12) K. Muska, M. Kauk, M. Grossberg, M. Altosaar, J. Raudoja, O. Volobujeva, *Energy Procedia* 10 (2011) 203–207.
- 13) K. Muska, M. Kauk, M. Grossberg, M. Altosaar, M. Pilvet, T. Varema, K. Timmo, O. Volobujeva, A. Mere, *Thin Solid Films* 535 (2013) 35–38.
- 14) <http://www.crvstalsol.com/eng/news/news.html>.
- 15) K. Timmo, M. Altosaar, J. Raudoja, M. Grossberg, M. Danilson, O. Volobujeva, E. Mellikov, *Proceedings of the 35th IEEE Photovoltaic Specialists Conference, Hawaii, 20-25 June (2010) 1982-1985*.
- 16) K. Muska, M. Kauk, M. Grossberg, M. Altosaar, J. Raudoja, O. Volobujeva, *Energy Procedia* 10 (2011) 323–327.
- 17) S. Chen, A. Walsh, Y. Luo, J. H. Yang, X. G. Gong, S. H. Wei, *Phys. Rev. B* 82 (2010) 195203.
- 18) S. Nakamura, T. Maeda, T. Wada, *Jpn. J. Appl. Phys.* 49 (2010) 121203.
- 19) M. Cao, *Chemical Physics Letters* 534 (2012) 34–37.
- 20) K. Ito, *Jpn. J. Appl. Phys.* 27 (1988) 2094–2097.
- 21) Y. Zhang, *J. Appl. Phys.* 111 (2012) 063709.
- 22) A. Weber, R. Mainz, H.W. Schock, *J. Appl. Phys.* 107 (2010) 013516.
- 23) J. Krustok, R. Josepson, T. Raadik, M. Danilson, *Physica B* 405 (2010) 3186–3189.
- 24) M. Grossberg, J. Krustok, K. Timmo, M. Altosaar, *Thin Solid Films* 517 (2009) 2489–2492.
- 25) M. Grossberg, J. Krustok, J. Raudoja, K. Timmo, M. Altosaar, T. Raadik, *Thin Solid Films* 519 (2011) 7403–7406.

APPENDIX B

CURRICULUM VITAE

1. Personal data

Name: Maris Pilvet
Date and place of birth: 31.10.1979, Kohtla-Järve, Estonia
E-mail address: maris.pilvet@ttu.ee

2. Education

Educational institution	Graduation year	Education (field of study/degree)
Kohtla - Järve Järve Secondary School	1998	Secondary education
Tallinn University of Technology, Faculty of Chemical and Materials Technology	2003	Bachelor Degree
Tallinn University of Technology, Faculty of Chemical and Materials Technology	2007	Master Degree

3. Language competence/skills (fluent, average, basic skills)

Language	Level
Estonian	Fluent, native language
English	Average
Russian	Average

4. Special courses

Period	Educational or other organisation
11– 18 September 2011	International Summer School “Photovoltaics and New Concepts of Quantum Solar Energy Conversion”, Hirschegg, Austria
21– 24 April 2013	Graduate school “Functional materials and nanotechnologies FM&NT”, Tartu, Estonia
8-13 September 2013	FEMS Euromat 2013, European Congress and Exhibition on Advanced Materials and Processes, Sevilla, Spain
20 November 2013	PhD student pre-workshop, 4 th European Kesterite workshop, Berlin, Germany

21-22 November 2013	4 th European Kesterite workshop, Berlin, Germany
26-30 May 2014	EMRS-2014 Spring Meeting, Lille, France
13-14 November 2014	5 th European Kesterite workshop, Tallinn, Estonia
26-27 February 2015	Center of excellence “High-technology Materials for Sustainable Development” conference-meeting
11-15 May 2015	EMRS-2015 Spring Meeting, Lille, France

5. Professional employment

Period	Organization	Position
2003–2005	Tallinn University of Technology, Faculty of Chemical and Materials Technology	Other staff
2005–2007	Tallinn University of Technology, Faculty of Chemical and Materials Technology	Engineer
2007–2008	Tallinn University of Technology, Faculty of Chemical and Materials Technology	Extraordinary Researcher
2008–2013	Tallinn University of Technology, Faculty of Chemical and Materials Technology	Extraordinary Researcher
2013–2016	Tallinn University of Technology, Faculty of Chemical and Materials Technology	Researcher
2016–...	Tallinn University of Technology, Department of Materials and Environmental Technology	Researcher

6. Research activity and thesis supervised

Projects

- 1.01.2016–1.03.2023 Advanced materials and high-technology devices for sustainable energetics, sensorics and nanoelectronics (TK141);
- 1.01.2004–31.12.2005 Contacts for semiconductor solar cells (G5914);

- 1.01.2007–31.12.2008 CuInSe₂ thin film preparation through a new selenisation process using chemical bath deposited selenium (ETF7268);
- 1.01.2008–31.12.2011 Extrinsic doping of CuInSe₂ and alternative buffer layers for monograin layer solar cells application (ETF7678);
- 1.01.2010–31.12.2013 Quaternary thin films by chalcogenization: mechanism and kinetics (ETF8147);
- 1.07.2010–31.08.2015 New materials for solar energetics (AR10128);
- 1.01.2012–31.12.2015 Development of CZTS monograin powders towards abundant and non-toxic materials for solar cells (ETF9346);
- 1.04.2012–30.06.2017 Increasing the efficiency of CZTS semiconductor material (Lep12065);
- 1.01.2014–31.12.2019 New materials and technologies for solar energetics (IUT19-28).

Supervision

- 01.09.2014 - 31.05.2016 L. Sha, Master's thesis "Optimization of CdS chemical deposition process for monograin membrane solar cells", Tallinn University of Technology

Defended dissertations

- 2007 Master's thesis "Contact formation for monograin layer solar cells", Tallinn University of Technology, supervisor Dr. T. Varema.
- 2003 Bachelor's thesis "ZnO layer deposition by RF- magnetron sputtering", Tallinn University of Technology, supervisor Dr. T. Varema.

LIST OF PUBLICATIONS

1. **M. Pilvet**, M. Kauk-Kuusik, M. Grossberg, T. Raadik, V. Mikli, R. Traksmaa, J. Raudoja, K. Timmo, J. Krustok, Modification of the optoelectronic properties of $\text{Cu}_2\text{CdSnS}_4$ through low-temperature annealing treatments, *Journal of Alloys and Compounds* (2017) *submitted*.
2. K. Timmo, M. Kauk-Kuusik, **M. Pilvet**, T. Raadik, M. Altosaar, M. Danilson, M. Grossberg, J. Raudoja, K. Ernits, Influence of order-disorder in $\text{Cu}_2\text{ZnSnS}_4$ powders on the performance of monograin layer solar cells, *Thin Solid Films* (2017) *in press*; <http://dx.doi.org/10.1016/j.tsf.2016.10.017>.
3. K. Timmo, M. Kauk-Kuusik, **M. Pilvet**, V. Mikli, E. Kärber, T. Raadik, I. Leinemann, M. Altosaar, J. Raudoja, Comparative study of SnS recrystallization in molten CdI_2 , SnCl_2 and KI, *Physica status solidi (c)* (2016) 13 (1), 8–12; DOI:10.1002/pssc.201510082.
4. **M. Pilvet**, M. Kauk-Kuusik, M. Altosaar, M. Grossberg, M. Danilson, K. Timmo, A. Mere, V. Mikli, Compositionally tunable structure and optical properties of $\text{Cu}_{1.85}(\text{Cd}_x\text{Zn}_{1-x})_{1.1}\text{SnS}_{4.1}$ ($0 \leq x \leq 1$) monograin powders, *Thin Solid Films* (2015) 582, 180–183; DOI:10.1016/j.tsf.2014.10.091.
5. O. Volobujeva, S. Bereznev, J. Raudoja, K. Otto, **M. Pilvet**, E. Mellikov, Synthesis and Characterisation of $\text{Cu}_2\text{ZnSnSe}_4$ Thin Films Prepared via a Vacuum Evaporation-Based Route, *Thin Solid Films* (2013) 535, 48–51; DOI:10.1016/j.tsf.2012.12.080.
6. M. Kauk-Kuusik, M. Altosaar, K. Muska, **M. Pilvet**, J. Raudoja, K. Timmo, T. Varema, M. Grossberg, E. Mellikov, O. Volobujeva, Post-growth annealing effect on the performance of $\text{Cu}_2\text{ZnSnSe}_4$ monograin layer solar cells, *Thin Solid Film* (2013) 535, 18–21; DOI:10.1016/j.tsf.2012.11.075.
7. K. Muska, M. Kauk-Kuusik, M. Grossberg, M. Altosaar, **M. Pilvet**, T. Varema, K. Timmo, O. Volobujeva, A. Mere, Impact of $\text{Cu}_2\text{ZnSn}(\text{Se}_x\text{S}_{1-x})_4$ ($x=0.3$) compositional ratios on the monograin powder properties and solar cells, *Thin Solid Films* (2013) 535, 35–38; DOI:10.1016/j.tsf.2012.10.031.
8. K. Timmo, M. Kauk-Kuusik, M. Altosaar, J. Raudoja, T. Raadik, M. Grossberg, T. Varema, **M. Pilvet**, I. Leinemann, O. Volobujeva, E. Mellikov, NOVEL $\text{Cu}_2\text{CdSnS}_4$ AND $\text{Cu}_2\text{ZnGeSe}_4$ ABSORBER MATERIALS FOR MONOGRAIN LAYER SOLAR CELL APPLICATION, *EU PVSEC 2013, Paris, France 30.Sept.-04.Okt. (2013)* Wiley-Blackwell, 2385–2388.

9. O. Volobujeva, E. Mellikov, S. Bereznev, J. Raudoja, K. Otto, **M. Pilvet**, T. Raadik, $\text{Cu}_2\text{ZnSnSe}_4$ thin films by selenization of stacked binaries, *E-MRS Spring Meeting 2012 - Symposium B: Strasbourg, France, May 14-18, (2012): program and abstract book*.
10. K. Muska, M. Kauk, M. Altosaar, **M. Pilvet**, M. Grossberg, O. Volobujeva, Synthesis of $\text{Cu}_2\text{ZnSnS}_4$ Monograin Powders with Different Compositions. In: *Energy Procedia* (2011) 203–207, Elsevier.
11. M. Kauk, K. Muska, M. Altosaar, J. Raudoja, **M. Pilvet**, T. Varema, K. Timmo, O. Volobujeva, Effects of sulphur and tin disulphide vapour treatments of $\text{Cu}_2\text{ZnSnS}(\text{Se})_4$ absorber materials for monograin solar cells, *Energy Procedia* (2011) 197–202.
12. K. Timmo, M. Altosaar, J. Raudoja, K. Muska, M. Kauk, **M. Pilvet**, T. Varema, M. Danilson, O. Volobujeva, E. Mellikov, Sulfur-containing $\text{Cu}_2\text{ZnSnSe}_4$ monograin powders for solar cells, *Solar Energy Materials and Solar Cells* (2010) 94 (11), 1889–1892; DOI: 10.1016/j.solmat.2010.06.046.
13. O. Volobujeva, E. Mellikov, J. Raudoja, S. Bereznev, **M. Pilvet**, Cu-In and Cu-Zn-Sn Films as Precursors for Production of CuInSe_2 and $\text{Cu}_2\text{ZnSnSe}_4$ Thin Films, *Thin-Film Compound Semiconductor Photovoltaics* (2009) 1165-M05-40.
14. L. Kaupmees, **M. Pilvet**, M. Altosaar, Effect of cleaning procedure of Mo surface to the properties of MoSe_2 , *Teaduskonverentsi teesid: XXIX Eesti Keemiapäevad, Tallinn (2005)* 36–37.

ELULOOKIRJELDUS

1. Isikuandmed

Ees- ja perekonnanimi: Maris Pilvet

Sünniaeg ja -koht: 31.10.1979, Kohtla-Järve, Eesti

Kodakondsus: Eesti

E-posti aadress: maris.pilvet@ttu.ee

2. Hariduskäik

Õppeasutus (nimetus lõpetamise ajal)	Lõpetamise aeg	Haridus (eriala/kraad)
Kohtla - Järve Järve Gümnaasium	1998	Keskharidus
Tallinna Tehnikaülikool, Keemia - ja materjalitehnoloogia instituut	2003	Bakalaureusekraad
Tallinna Tehnikaülikool, Keemia- ja materjalitehnoloogia instituut	2007	Magistrikraad

3. Keelteoskus

Keel	Tase
Eesti	Emakeel
Inglise	Kesktaase
Vene	Kesktaase

4. Täiendusõpe

Õppimise aeg	Täiendusõppe korraldaja nimetus
11.- 18. september 2011	International Summer School "Photovoltaics and New Concepts of Quantum Solar Energy Conversion", Hirschegg, Austria
21.- 24. aprill 2013	Doktorikool "Funktionaalsed materjalid ja nanotehnoloogiad" (FM&NT), Tartu, Eesti
8.- 13. september 2013	FEMS Euromat 2013, European Congress and Exhibition on Advanced Materials and Processes, Sevilla, Hispaania
20. november 2013	PhD student pre-workshop, 4 th European Kesterite workshop, Berlin, Saksamaa
21.-22. november 2013	4 th European Kesterite workshop, Berlin, Saksamaa

26.-30. mai 2014	EMRS-2014 Spring Meeting, Lille, Prantsusmaa
13.-14. november 2014	5 th European Kesterite workshop, Tallinn, Eesti
26.-27. veebruar 2015	Tippkeskuse „Kõrgtehnoloogilised materjalid jätkusuutlikuks arenguks" konverents-seminar
11.-15. mai 2015	EMRS-2015 Spring Meeting, Lille, Prantsusmaa

5. Teenistuskäik

Töötamise aeg	Tööandja nimetus	Ametikoht
2003–2005	Tallinna Tehnikaülikool, Materjaliteaduse instituut	Tehniline töötaja
2005–2007	Tallinna Tehnikaülikool, Materjaliteaduse instituut	Insener
2007–2008	Tallinna Tehnikaülikool, Materjaliteaduse ja materjalide tehnoloogia doktorikool	Erakorraline teadur
2008–2013	Tallinna Tehnikaülikool, Materjaliteaduse instituut	Erakorraline teadur
2013–2016	Tallinna Tehnikaülikool, Materjaliteaduse instituut	Teadur
2016–...	Tallinna Tehnikaülikool, Materjali- ja keskkonnatehnoloogia instituut	Teadur

6. Teadustegevus, sh juhendatud lõputööd

Projektid

- 1.01.2016–1.03.2023 Uudsed materjalid ja kõrgtehnoloogilised seadmed energia salvestamise ja muundamise süsteemidele (TK141);
- 1.01.2004–31.12.2005 Kontaktid pooljuhtpäikesepatareidele (G5914);
- 1.01.2007–31.12.2008 CuInSe₂ saamisvõimaluste uurimine CuIn sulamite seleniseerimisel vesilahustest (ETF7268);
- 1.01.2008–31.12.2011 CuInSe₂ legerimine võõrlisanditega ja alternatiivsed puhverkihid rakendamiseks monoterakihi päikesepatareides (ETF7678);

- 1.01.2010–31.12.2013 Nelikmaterjalide kiled kalkogeniseerimise protsessis; mehhanism ja kineetika (ETF8147);
- 1.07.2010–31.08.2015 Uued materjalid päikesseenergeetikale (AR10128);
- 1.01.2012–31.12.2015 Development of CZTS monograin powders towards abundant and non-toxic materials for solar cells (ETF9346);
- 1.04.2012–30.06.2017 CZTS monoterakiht päikesepatareide efektiivsuse parandamine (Lep12065);
- 1.01.2014–31.12.2019 Uued materjalid ja tehnoloogiad päikesenergeetikale (IUT19-28).

Kaasjuhendamine

- 01.09.2014 - 31.05.2016 L. Sha, magistritöö „Vask-tsink-tina-sulfiidtüüpi päikesepatarei puhverkihi optimeerimine“, Tallinna Tehnikaülikool

Kaitstud lõputööd

- 2007 Magistritöö „Kontaktide formeerimine monoterakihi päikesepatareile“, Tallinna Tehnikaülikool, juhendaja T. Varema.
- 2003 Bakalaureusetöö „ZnO õhukese kile sadestamine raadiosageduslikul magnetronpihustusmeetodil“, Tallinna Tehnikaülikool, juhendaja T. Varema.

**DISSERTATIONS DEFENDED AT
TALLINN UNIVERSITY OF TECHNOLOGY ON
NATURAL AND EXACT SCIENCES**

1. **Olav Kongas**. Nonlinear Dynamics in Modeling Cardiac Arrhythmias. 1998.
2. **Kalju Vanatalu**. Optimization of Processes of Microbial Biosynthesis of Isotopically Labeled Biomolecules and Their Complexes. 1999.
3. **Ahto Buldas**. An Algebraic Approach to the Structure of Graphs. 1999.
4. **Monika Drews**. A Metabolic Study of Insect Cells in Batch and Continuous Culture: Application of Chemostat and Turbidostat to the Production of Recombinant Proteins. 1999.
5. **Eola Valdre**. Endothelial-Specific Regulation of Vessel Formation: Role of Receptor Tyrosine Kinases. 2000.
6. **Kalju Lott**. Doping and Defect Thermodynamic Equilibrium in ZnS. 2000.
7. **Reet Koljak**. Novel Fatty Acid Dioxygenases from the Corals *Plexaura homomalla* and *Gersemia fruticosa*. 2001.
8. **Anne Paju**. Asymmetric oxidation of Prochiral and Racemic Ketones by Using Sharpless Catalyst. 2001.
9. **Marko Vendelin**. Cardiac Mechanoenergetics *in silico*. 2001.
10. **Pearu Peterson**. Multi-Soliton Interactions and the Inverse Problem of Wave Crest. 2001.
11. **Anne Menert**. Microcalorimetry of Anaerobic Digestion. 2001.
12. **Toomas Tiivel**. The Role of the Mitochondrial Outer Membrane in *in vivo* Regulation of Respiration in Normal Heart and Skeletal Muscle Cell. 2002.
13. **Olle Hints**. Ordovician Scolecodonts of Estonia and Neighbouring Areas: Taxonomy, Distribution, Palaeoecology, and Application. 2002.
14. **Jaak Nõlvak**. Chitinozoan Biostratigraphy in the Ordovician of Baltoscandia. 2002.
15. **Liivi Kluge**. On Algebraic Structure of Pre-Operad. 2002.
16. **Jaanus Lass**. Biosignal Interpretation: Study of Cardiac Arrhythmias and Electromagnetic Field Effects on Human Nervous System. 2002.
17. **Janek Peterson**. Synthesis, Structural Characterization and Modification of PAMAM Dendrimers. 2002.
18. **Merike Vaher**. Room Temperature Ionic Liquids as Background Electrolyte Additives in Capillary Electrophoresis. 2002.
19. **Valdek Mikli**. Electron Microscopy and Image Analysis Study of Powdered Hardmetal Materials and Optoelectronic Thin Films. 2003.
20. **Mart Viljus**. The Microstructure and Properties of Fine-Grained Cermets. 2003.
21. **Signe Kask**. Identification and Characterization of Dairy-Related *Lactobacillus*. 2003.
22. **Tiiu-Mai Laht**. Influence of Microstructure of the Curd on Enzymatic and Microbiological Processes in Swiss-Type Cheese. 2003.
23. **Anne Kuuskalu**. 2–5A Synthetase in the Marine Sponge *Geodia cydonium*. 2003.

24. **Sergei Bereznev**. Solar Cells Based on Polycrystalline Copper-Indium Chalcogenides and Conductive Polymers. 2003.
25. **Kadri Kriis**. Asymmetric Synthesis of C₂-Symmetric Bimorpholines and Their Application as Chiral Ligands in the Transfer Hydrogenation of Aromatic Ketones. 2004.
26. **Jekaterina Reut**. Polypyrrole Coatings on Conducting and Insulating Substrates. 2004.
27. **Sven Nõmm**. Realization and Identification of Discrete-Time Nonlinear Systems. 2004.
28. **Olga Kijatkina**. Deposition of Copper Indium Disulphide Films by Chemical Spray Pyrolysis. 2004.
29. **Gert Tamberg**. On Sampling Operators Defined by Rogosinski, Hann and Blackman Windows. 2004.
30. **Monika Übner**. Interaction of Humic Substances with Metal Cations. 2004.
31. **Kaarel Adamberg**. Growth Characteristics of Non-Starter Lactic Acid Bacteria from Cheese. 2004.
32. **Imre Vallikivi**. Lipase-Catalysed Reactions of Prostaglandins. 2004.
33. **Merike Peld**. Substituted Apatites as Sorbents for Heavy Metals. 2005.
34. **Vitali Syritski**. Study of Synthesis and Redox Switching of Polypyrrole and Poly(3,4-ethylenedioxythiophene) by Using *in-situ* Techniques. 2004.
35. **Lee Põllumaa**. Evaluation of Ecotoxicological Effects Related to Oil Shale Industry. 2004.
36. **Riina Aav**. Synthesis of 9,11-Secosterols Intermediates. 2005.
37. **Andres Braunbrück**. Wave Interaction in Weakly Inhomogeneous Materials. 2005.
38. **Robert Kitt**. Generalised Scale-Invariance in Financial Time Series. 2005.
39. **Juss Pavelson**. Mesoscale Physical Processes and the Related Impact on the Summer Nutrient Fields and Phytoplankton Blooms in the Western Gulf of Finland. 2005.
40. **Olari Ilison**. Solitons and Solitary Waves in Media with Higher Order Dispersive and Nonlinear Effects. 2005.
41. **Maksim Säkki**. Intermittency and Long-Range Structurization of Heart Rate. 2005.
42. **Enli Kiipli**. Modelling Seawater Chemistry of the East Baltic Basin in the Late Ordovician–Early Silurian. 2005.
43. **Igor Golovtsov**. Modification of Conductive Properties and Processability of Polyparaphenylene, Polypyrrole and polyaniline. 2005.
44. **Katrin Laos**. Interaction Between Furcellaran and the Globular Proteins (Bovine Serum Albumin β -Lactoglobulin). 2005.
45. **Arvo Mere**. Structural and Electrical Properties of Spray Deposited Copper Indium Disulphide Films for Solar Cells. 2006.
46. **Sille Ehala**. Development and Application of Various On- and Off-Line Analytical Methods for the Analysis of Bioactive Compounds. 2006.
47. **Maria Kulp**. Capillary Electrophoretic Monitoring of Biochemical Reaction Kinetics. 2006.

48. **Anu Aaspõllu.** Proteinases from *Vipera lebetina* Snake Venom Affecting Hemostasis. 2006.
49. **Lyudmila Chekulayeva.** Photosensitized Inactivation of Tumor Cells by Porphyrins and Chlorins. 2006.
50. **Merle Uudsemaa.** Quantum-Chemical Modeling of Solvated First Row Transition Metal Ions. 2006.
51. **Tagli Pitsi.** Nutrition Situation of Pre-School Children in Estonia from 1995 to 2004. 2006.
52. **Angela Ivask.** Luminescent Recombinant Sensor Bacteria for the Analysis of Bioavailable Heavy Metals. 2006.
53. **Tiina Lõugas.** Study on Physico-Chemical Properties and Some Bioactive Compounds of Sea Buckthorn (*Hippophae rhamnoides* L.). 2006.
54. **Kaja Kasemets.** Effect of Changing Environmental Conditions on the Fermentative Growth of *Saccharomyces cerevisiae* S288C: Auxo-accelerostat Study. 2006.
55. **Ildar Nisamedtinov.** Application of ^{13}C and Fluorescence Labeling in Metabolic Studies of *Saccharomyces* spp. 2006.
56. **Alar Leibak.** On Additive Generalisation of Voronoï's Theory of Perfect Forms over Algebraic Number Fields. 2006.
57. **Andri Jagomägi.** Photoluminescence of Chalcopyrite Tellurides. 2006.
58. **Tõnu Martma.** Application of Carbon Isotopes to the Study of the Ordovician and Silurian of the Baltic. 2006.
59. **Marit Kauk.** Chemical Composition of CuInSe₂ Monograin Powders for Solar Cell Application. 2006.
60. **Julia Kois.** Electrochemical Deposition of CuInSe₂ Thin Films for Photovoltaic Applications. 2006.
61. **Ilona Oja Ačik.** Sol-Gel Deposition of Titanium Dioxide Films. 2007.
62. **Tiia Anmann.** Integrated and Organized Cellular Bioenergetic Systems in Heart and Brain. 2007.
63. **Katrin Trummal.** Purification, Characterization and Specificity Studies of Metalloproteinases from *Vipera lebetina* Snake Venom. 2007.
64. **Gennadi Lessin.** Biochemical Definition of Coastal Zone Using Numerical Modeling and Measurement Data. 2007.
65. **Enno Pais.** Inverse problems to determine non-homogeneous degenerate memory kernels in heat flow. 2007.
66. **Maria Borissova.** Capillary Electrophoresis on Alkylimidazolium Salts. 2007.
67. **Karin Valmsen.** Prostaglandin Synthesis in the Coral *Plexaura homomalla*: Control of Prostaglandin Stereochemistry at Carbon 15 by Cyclooxygenases. 2007.
68. **Kristjan Piirimäe.** Long-Term Changes of Nutrient Fluxes in the Drainage Basin of the Gulf of Finland – Application of the PolFlow Model. 2007.
69. **Tatjana Dedova.** Chemical Spray Pyrolysis Deposition of Zinc Sulfide Thin Films and Zinc Oxide Nanostructured Layers. 2007.

70. **Katrin Tomson.** Production of Labelled Recombinant Proteins in Fed-Batch Systems in *Escherichia coli*. 2007.
71. **Cecilia Sarmiento.** Suppressors of RNA Silencing in Plants. 2008.
72. **Vilja Mardla.** Inhibition of Platelet Aggregation with Combination of Antiplatelet Agents. 2008.
73. **Maie Bachmann.** Effect of Modulated Microwave Radiation on Human Resting Electroencephalographic Signal. 2008.
74. **Dan H÷ivonen.** Terahertz Spectroscopy of Low-Dimensional Spin Systems. 2008.
75. **Ly Villo.** Stereoselective Chemoenzymatic Synthesis of Deoxy Sugar Esters Involving *Candida antarctica* Lipase B. 2008.
76. **Johan Anton.** Technology of Integrated Photoelasticity for Residual Stress Measurement in Glass Articles of Axisymmetric Shape. 2008.
77. **Olga Volobujeva.** SEM Study of Selenization of Different Thin Metallic Films. 2008.
78. **Artur Jõgi.** Synthesis of 4'-Substituted 2,3'-dideoxynucleoside Analogues. 2008.
79. **Mario Kadastik.** Doubly Charged Higgs Boson Decays and Implications on Neutrino Physics. 2008.
80. **Fernando Pérez-Caballero.** Carbon Aerogels from 5-Methylresorcinol-Formaldehyde Gels. 2008.
81. **Sirje Vaask.** The Comparability, Reproducibility and Validity of Estonian Food Consumption Surveys. 2008.
82. **Anna Menaker.** Electrosynthesized Conducting Polymers, Polypyrrole and Poly(3,4-ethylenedioxythiophene), for Molecular Imprinting. 2009.
83. **Lauri Ilison.** Solitons and Solitary Waves in Hierarchical Korteweg-de Vries Type Systems. 2009.
84. **Kaia Ernits.** Study of In₂S₃ and ZnS Thin Films Deposited by Ultrasonic Spray Pyrolysis and Chemical Deposition. 2009.
85. **Veljo Sinivee.** Portable Spectrometer for Ionizing Radiation "Gammamapper". 2009.
86. **Jüri Virkepu.** On Lagrange Formalism for Lie Theory and Operadic Harmonic Oscillator in Low Dimensions. 2009.
87. **Marko Piirsoo.** Deciphering Molecular Basis of Schwann Cell Development. 2009.
88. **Kati Helmja.** Determination of Phenolic Compounds and Their Antioxidative Capability in Plant Extracts. 2010.
89. **Merike Sõmera.** Sobemoviruses: Genomic Organization, Potential for Recombination and Necessity of P1 in Systemic Infection. 2010.
90. **Kristjan Laes.** Preparation and Impedance Spectroscopy of Hybrid Structures Based on CuIn₃Se₅ Photoabsorber. 2010.
91. **Kristin Lippur.** Asymmetric Synthesis of 2,2'-Bimorpholine and its 5,5'-Substituted Derivatives. 2010.
92. **Merike Luman.** Dialysis Dose and Nutrition Assessment by an Optical Method. 2010.

93. **Mihhail Berezovski.** Numerical Simulation of Wave Propagation in Heterogeneous and Microstructured Materials. 2010.
94. **Tamara Aid-Pavlidis.** Structure and Regulation of BDNF Gene. 2010.
95. **Olga Bragina.** The Role of Sonic Hedgehog Pathway in Neuro- and Tumorigenesis. 2010.
96. **Merle Randrüüt.** Wave Propagation in Microstructured Solids: Solitary and Periodic Waves. 2010.
97. **Marju Laars.** Asymmetric Organocatalytic Michael and Aldol Reactions Mediated by Cyclic Amines. 2010.
98. **Maarja Grossberg.** Optical Properties of Multinary Semiconductor Compounds for Photovoltaic Applications. 2010.
99. **Alla Maloverjan.** Vertebrate Homologues of Drosophila Fused Kinase and Their Role in Sonic Hedgehog Signalling Pathway. 2010.
100. **Priit Pruunsild.** Neuronal Activity-Dependent Transcription Factors and Regulation of Human *BDNF* Gene. 2010.
101. **Tatjana Knjazeva.** New Approaches in Capillary Electrophoresis for Separation and Study of Proteins. 2011.
102. **Atanas Katerski.** Chemical Composition of Sprayed Copper Indium Disulfide Films for Nanostructured Solar Cells. 2011.
103. **Kristi Timmo.** Formation of Properties of CuInSe_2 and $\text{Cu}_2\text{ZnSn}(\text{S},\text{Se})_4$ Monograin Powders Synthesized in Molten KI. 2011.
104. **Kert Tamm.** Wave Propagation and Interaction in Mindlin-Type Microstructured Solids: Numerical Simulation. 2011.
105. **Adrian Popp.** Ordovician Proetid Trilobites in Baltoscandia and Germany. 2011.
106. **Ove Pärn.** Sea Ice Deformation Events in the Gulf of Finland and This Impact on Shipping. 2011.
107. **Germo Väli.** Numerical Experiments on Matter Transport in the Baltic Sea. 2011.
108. **Andrus Seiman.** Point-of-Care Analyser Based on Capillary Electrophoresis. 2011.
109. **Olga Katargina.** Tick-Borne Pathogens Circulating in Estonia (Tick-Borne Encephalitis Virus, *Anaplasma phagocytophilum*, *Babesia* Species): Their Prevalence and Genetic Characterization. 2011.
110. **Ingrid Sumeri.** The Study of Probiotic Bacteria in Human Gastrointestinal Tract Simulator. 2011.
111. **Kairit Zovo.** Functional Characterization of Cellular Copper Proteome. 2011.
112. **Natalja Makarytsheva.** Analysis of Organic Species in Sediments and Soil by High Performance Separation Methods. 2011.
113. **Monika Mortimer.** Evaluation of the Biological Effects of Engineered Nanoparticles on Unicellular Pro- and Eukaryotic Organisms. 2011.
114. **Kersti Tepp.** Molecular System Bioenergetics of Cardiac Cells: Quantitative Analysis of Structure-Function Relationship. 2011.

115. **Anna-Liisa Peikolainen.** Organic Aerogels Based on 5-Methylresorcinol. 2011.
116. **Leeli Amon.** Palaeoecological Reconstruction of Late-Glacial Vegetation Dynamics in Eastern Baltic Area: A View Based on Plant Macrofossil Analysis. 2011.
117. **Tanel Peets.** Dispersion Analysis of Wave Motion in Microstructured Solids. 2011.
118. **Liina Kaupmees.** Selenization of Molybdenum as Contact Material in Solar Cells. 2011.
119. **Allan Olspert.** Properties of VPg and Coat Protein of Sobemoviruses. 2011.
120. **Kadri Koppel.** Food Category Appraisal Using Sensory Methods. 2011.
121. **Jelena Gorbatšova.** Development of Methods for CE Analysis of Plant Phenolics and Vitamins. 2011.
122. **Karin Viipsi.** Impact of EDTA and Humic Substances on the Removal of Cd and Zn from Aqueous Solutions by Apatite. 2012.
123. **David Schryer.** Metabolic Flux Analysis of Compartmentalized Systems Using Dynamic Isotopologue Modeling. 2012.
124. **Ardo Illaste.** Analysis of Molecular Movements in Cardiac Myocytes. 2012.
125. **Indrek Reile.** 3-Alkylcyclopentane-1,2-Diones in Asymmetric Oxidation and Alkylation Reactions. 2012.
126. **Tatjana Tamberg.** Some Classes of Finite 2-Groups and Their Endomorphism Semigroups. 2012.
127. **Taavi Liblik.** Variability of Thermohaline Structure in the Gulf of Finland in Summer. 2012.
128. **Priidik Lagemaa.** Operational Forecasting in Estonian Marine Waters. 2012.
129. **Andrei Errapart.** Photoelastic Tomography in Linear and Non-linear Approximation. 2012.
130. **Külliki Krabbi.** Biochemical Diagnosis of Classical Galactosemia and Mucopolysaccharidoses in Estonia. 2012.
131. **Kristel Kaseleht.** Identification of Aroma Compounds in Food using SPME-GC/MS and GC-Olfactometry. 2012.
132. **Kristel Kodar.** Immunoglobulin G Glycosylation Profiling in Patients with Gastric Cancer. 2012.
133. **Kai Rosin.** Solar Radiation and Wind as Agents of the Formation of the Radiation Regime in Water Bodies. 2012.
134. **Ann Tiiman.** Interactions of Alzheimer's Amyloid-Beta Peptides with Zn(II) and Cu(II) Ions. 2012.
135. **Olga Gavrilova.** Application and Elaboration of Accounting Approaches for Sustainable Development. 2012.
136. **Olesja Bondarenko.** Development of Bacterial Biosensors and Human Stem Cell-Based *In Vitro* Assays for the Toxicological Profiling of Synthetic Nanoparticles. 2012.

137. **Katri Muska.** Study of Composition and Thermal Treatments of Quaternary Compounds for Monograin Layer Solar Cells. 2012.
138. **Ranno Nahku.** Validation of Critical Factors for the Quantitative Characterization of Bacterial Physiology in Accelerostat Cultures. 2012.
139. **Petri-Jaan Lahtvee.** Quantitative Omics-level Analysis of Growth Rate Dependent Energy Metabolism in *Lactococcus lactis*. 2012.
140. **Kerti Orumets.** Molecular Mechanisms Controlling Intracellular Glutathione Levels in Baker's Yeast *Saccharomyces cerevisiae* and its Random Mutagenized Glutathione Over-Accumulating Isolate. 2012.
141. **Loreida Timberg.** Spice-Cured Sprats Ripening, Sensory Parameters Development, and Quality Indicators. 2012.
142. **Anna Mihhalevski.** Rye Sourdough Fermentation and Bread Stability. 2012.
143. **Liisa Arike.** Quantitative Proteomics of *Escherichia coli*: From Relative to Absolute Scale. 2012.
144. **Kairi Otto.** Deposition of In₂S₃ Thin Films by Chemical Spray Pyrolysis. 2012.
145. **Mari Sepp.** Functions of the Basic Helix-Loop-Helix Transcription Factor TCF4 in Health and Disease. 2012.
146. **Anna Suhhova.** Detection of the Effect of Weak Stressors on Human Resting Electroencephalographic Signal. 2012.
147. **Aram Kazarjan.** Development and Production of Extruded Food and Feed Products Containing Probiotic Microorganisms. 2012.
148. **Rivo Uiboupin.** Application of Remote Sensing Methods for the Investigation of Spatio-Temporal Variability of Sea Surface Temperature and Chlorophyll Fields in the Gulf of Finland. 2013.
149. **Tiina Kriščiunaite.** A Study of Milk Coagulability. 2013.
150. **Tuuli Levandi.** Comparative Study of Cereal Varieties by Analytical Separation Methods and Chemometrics. 2013.
151. **Natalja Kabanova.** Development of a Microcalorimetric Method for the Study of Fermentation Processes. 2013.
152. **Himani Khanduri.** Magnetic Properties of Functional Oxides. 2013.
153. **Julia Smirnova.** Investigation of Properties and Reaction Mechanisms of Redox-Active Proteins by ESI MS. 2013.
154. **Mervi Sepp.** Estimation of Diffusion Restrictions in Cardiomyocytes Using Kinetic Measurements. 2013.
155. **Kersti Jääger.** Differentiation and Heterogeneity of Mesenchymal Stem Cells. 2013.
156. **Victor Alari.** Multi-Scale Wind Wave Modeling in the Baltic Sea. 2013.
157. **Taavi Päll.** Studies of CD44 Hyaluronan Binding Domain as Novel Angiogenesis Inhibitor. 2013.
158. **Allan Niidu.** Synthesis of Cyclopentane and Tetrahydrofuran Derivatives. 2013.
159. **Julia Geller.** Detection and Genetic Characterization of *Borrelia* Species Circulating in Tick Population in Estonia. 2013.

160. **Irina Stulova**. The Effects of Milk Composition and Treatment on the Growth of Lactic Acid Bacteria. 2013.
161. **Jana Holmar**. Optical Method for Uric Acid Removal Assessment During Dialysis. 2013.
162. **Kerti Ausmees**. Synthesis of Heterobicyclo[3.2.0]heptane Derivatives *via* Multicomponent Cascade Reaction. 2013.
163. **Minna Varikmaa**. Structural and Functional Studies of Mitochondrial Respiration Regulation in Muscle Cells. 2013.
164. **Indrek Koppel**. Transcriptional Mechanisms of BDNF Gene Regulation. 2014.
165. **Kristjan Pilt**. Optical Pulse Wave Signal Analysis for Determination of Early Arterial Ageing in Diabetic Patients. 2014.
166. **Andres Anier**. Estimation of the Complexity of the Electroencephalogram for Brain Monitoring in Intensive Care. 2014.
167. **Toivo Kallaste**. Pyroclastic Sanidine in the Lower Palaeozoic Bentonites – A Tool for Regional Geological Correlations. 2014.
168. **Erki Kärber**. Properties of ZnO-nanorod/In₂S₃/CuInS₂ Solar Cell and the Constituent Layers Deposited by Chemical Spray Method. 2014.
169. **Julia Lehner**. Formation of Cu₂ZnSnS₄ and Cu₂ZnSnSe₄ by Chalcogenisation of Electrochemically Deposited Precursor Layers. 2014.
170. **Peep Pitk**. Protein- and Lipid-rich Solid Slaughterhouse Waste Anaerobic Co-digestion: Resource Analysis and Process Optimization. 2014.
171. **Kaspar Valgepea**. Absolute Quantitative Multi-omics Characterization of Specific Growth Rate-dependent Metabolism of *Escherichia coli*. 2014.
172. **Artur Noole**. Asymmetric Organocatalytic Synthesis of 3,3'-Disubstituted Oxindoles. 2014.
173. **Robert Tsanev**. Identification and Structure-Functional Characterisation of the Gene Transcriptional Repressor Domain of Human Gli Proteins. 2014.
174. **Dmitri Kartofelev**. Nonlinear Sound Generation Mechanisms in Musical Acoustic. 2014.
175. **Sigrid Hade**. GIS Applications in the Studies of the Palaeozoic Graptolite Argillite and Landscape Change. 2014.
176. **Agne Velthut-Meikas**. Ovarian Follicle as the Environment of Oocyte Maturation: The Role of Granulosa Cells and Follicular Fluid at Pre-Ovulatory Development. 2014.
177. **Kristel Hälvin**. Determination of B-group Vitamins in Food Using an LC-MS Stable Isotope Dilution Assay. 2014.
178. **Mailis Päre**. Characterization of the Oligoadenylate Synthetase Subgroup from Phylum Porifera. 2014.
179. **Jekaterina Kazantseva**. Alternative Splicing of *TAF4*: A Dynamic Switch between Distinct Cell Functions. 2014.
180. **Jaanus Suurväli**. Regulator of G Protein Signalling 16 (RGS16): Functions in Immunity and Genomic Location in an Ancient MHC-Related Evolutionarily Conserved Synteny Group. 2014.

181. **Ene Viiard.** Diversity and Stability of Lactic Acid Bacteria During Rye Sourdough Propagation. 2014.
182. **Kristella Hansen.** Prostaglandin Synthesis in Marine Arthropods and Red Algae. 2014.
183. **Helike Lõhelaid.** Allene Oxide Synthase-lipoxygenase Pathway in Coral Stress Response. 2015.
184. **Normunds Stivriņš.** Postglacial Environmental Conditions, Vegetation Succession and Human Impact in Latvia. 2015.
185. **Mary-Liis Kütt.** Identification and Characterization of Bioactive Peptides with Antimicrobial and Immunoregulating Properties Derived from Bovine Colostrum and Milk. 2015.
186. **Kazbulat Šogenov.** Petrophysical Models of the CO₂ Plume at Prospective Storage Sites in the Baltic Basin. 2015.
187. **Taavi Raadik.** Application of Modulation Spectroscopy Methods in Photovoltaic Materials Research. 2015.
188. **Reio Pöder.** Study of Oxygen Vacancy Dynamics in Sc-doped Ceria with NMR Techniques. 2015.
189. **Sven Siir.** Internal Geochemical Stratification of Bentonites (Altered Volcanic Ash Beds) and its Interpretation. 2015.
190. **Kaur Jaanson.** Novel Transgenic Models Based on Bacterial Artificial Chromosomes for Studying BDNF Gene Regulation. 2015.
191. **Niina Karro.** Analysis of ADP Compartmentation in Cardiomyocytes and Its Role in Protection Against Mitochondrial Permeability Transition Pore Opening. 2015.
192. **Piret Laht.** B-plexins Regulate the Maturation of Neurons Through Microtubule Dynamics. 2015.
193. **Sergei Žari.** Organocatalytic Asymmetric Addition to Unsaturated 1,4-Dicarbonyl Compounds. 2015.
194. **Natalja Buhhalko.** Processes Influencing the Spatio-temporal Dynamics of Nutrients and Phytoplankton in Summer in the Gulf of Finland, Baltic Sea. 2015.
195. **Natalia Maticiu.** Mechanism of Changes in the Properties of Chemically Deposited CdS Thin Films Induced by Thermal Annealing. 2015.
196. **Mario Öeren.** Computational Study of Cyclohexylhemicurbiturils. 2015.
197. **Mari Kalda.** Mechanoenergetics of a Single Cardiomyocyte. 2015.
198. **Ieva Grudzinska.** Diatom Stratigraphy and Relative Sea Level Changes of the Eastern Baltic Sea over the Holocene. 2015.
199. **Anna Kazantseva.** Alternative Splicing in Health and Disease. 2015.
200. **Jana Kazarjan.** Investigation of Endogenous Antioxidants and Their Synthetic Analogues by Capillary Electrophoresis. 2016.
201. **Maria Safonova.** SnS Thin Films Deposition by Chemical Solution Method and Characterization. 2016.

202. **Jekaterina Mazina.** Detection of Psycho- and Bioactive Drugs in Different Sample Matrices by Fluorescence Spectroscopy and Capillary Electrophoresis. 2016.
203. **Karin Rosenstein.** Genes Regulated by Estrogen and Progesterone in Human Endometrium. 2016.
204. **Aleksei Tretjakov.** A Macromolecular Imprinting Approach to Design Synthetic Receptors for Label-Free Biosensing Applications. 2016.
205. **Mati Danilson.** Temperature Dependent Electrical Properties of Kesterite Monograin Layer Solar Cells. 2016.
206. **Kaspar Kevvai.** Applications of ^{15}N -labeled Yeast Hydrolysates in Metabolic Studies of *Lactococcus lactis* and *Saccharomyces Cerevisiae*. 2016.
207. **Kadri Aller.** Development and Applications of Chemically Defined Media for Lactic Acid Bacteria. 2016.
208. **Gert Preegel.** Cyclopentane-1,2-dione and Cyclopent-2-en-1-one in Asymmetric Organocatalytic Reactions. 2016.
209. **Jekaterina Služenikina.** Applications of Marine Scatterometer Winds and Quality Aspects of their Assimilation into Numerical Weather Prediction Model HIRLAM. 2016.
210. **Erkki Kask.** Study of Kesterite Solar Cell Absorbers by Capacitance Spectroscopy Methods. 2016.
211. **Jürgen Arund.** Major Chromophores and Fluorophores in the Spent Dialysate as Cornerstones for Optical Monitoring of Kidney Replacement Therapy. 2016.
212. **Andrei Šamarin.** Hybrid PET/MR Imaging of Bone Metabolism and Morphology. 2016.
213. **Kairi Kasemets.** Inverse Problems for Parabolic Integro-Differential Equations with Instant and Integral Conditions. 2016.
214. **Edith Soosaar.** An Evolution of Freshwater Bulge in Laboratory Scale Experiments and Natural Conditions. 2016.
215. **Peeter Laas.** Spatiotemporal Niche-Partitioning of Bacterioplankton Community across Environmental Gradients in the Baltic Sea. 2016.
216. **Margus Voolma.** Geochemistry of Organic-Rich Metalliferous Oil Shale/Black Shale of Jordan and Estonia. 2016.
217. **Karin Ojamäe.** The Ecology and Photobiology of Mixotrophic Alveolates in the Baltic Sea. 2016.
218. **Anne Pink.** The Role of CD44 in the Control of Endothelial Cell Proliferation and Angiogenesis. 2016.
219. **Kristiina Kreek.** Metal-Doped Aerogels Based on Resorcinol Derivatives. 2016.
220. **Kaia Kukk.** Expression of Human Prostaglandin H Synthases in the Yeast *Pichia pastoris*. 2016.
221. **Martin Laasmaa.** Revealing Aspects of Cardiac Function from Fluorescence and Electrophysiological Recordings. 2016.
222. **Eeva-Gerda Kobrin.** Development of Point of Care Applications for Capillary Electrophoresis. 2016.

223. **Villu Kikas**. Physical Processes Controlling the Surface Layer Dynamics in the Stratified Gulf of Finland: An Application of Ferrybox Technology. 2016.
224. **Maris Skudra**. Features of Thermohaline Structure and Circulation in the Gulf of Riga. 2017.
225. **Sirje Sildever**. Influence of Physical-Chemical Factors on Community and Populations of the Baltic Sea Spring Bloom Microalgae. 2017.
226. **Nicolae Spalatu**. Development of CdTe Absorber Layer for Thin-Film Solar Cells. 2017.
227. **Kristi Luberg**. Human Tropomyosin-Related Kinase A and B: from Transcript Diversity to Novel Inhibitors. 2017.
228. **Andrus Kaldma**. Metabolic Remodeling of Human Colorectal Cancer: Alterations in Energy Fluxes. 2017.
229. **Irina Osadchuk**. Structures and Catalytic Properties of Titanium and Iridium Based Complexes. 2017.
230. **Roman Borožnjak**. A Computational Approach for Rational Monomer Selection in Molecularly Imprinted Polymer Synthesis. 2017.
231. **Sten Erm**. Use of Mother-Daughter Multi-Bioreactor Systems for Studies of Steady State Microbial Growth Space. 2017.
232. **Merike Kriisa**. Study of ZnO:In, Zn(O,S) and Sb₂S₃ Thin Films Deposited by Aerosol Methods. 2017.
233. **Marianna Surženko**. Selection of Functional Starter Bacteria for Type I Sourdough Process. 2017.
234. **Nkwusi God'swill Chimezie**. Formation and Growth of Cu₂ZnSnS₄ Monograin Powder in Molten CdI₂. 2017.